University of Cincinnati

Date: 5/4/2021

I, Chamindu C Gunatilaka, hereby submit this original work as part of the requirements for the degree of Doctor of Philosophy in Physics.

It is entitled:

Neonatal Airway Analysis Using Magnetic Resonance Imaging and Computational Fluid Dynamics

Student's name: **Chamindu C Gunatilaka**

This work and its defense approved by:

Committee chair: David Mast, Ph.D.

Committee member: Zackary Cleveland, Ph.D.

Committee member: L. C. R. Wijewardhana, Ph.D.

Committee member: Jason Woods, Ph.D.

38264

Neonatal Airway Analysis Using Magnetic Resonance Imaging and Computational Fluid Dynamics

A dissertation submitted to the

Graduate School

of the University of Cincinnati

in partial fulfillment of the

requirements for the degree of

Doctor of Philosophy

in the Department of Physics

of the College of Arts and Sciences

by

Chamindu Chinthaka Gunatilaka

B.S. University of Colombo

May 2021

Committee Chair: Jason C. Woods, Ph.D.

Abstract

Newborns admitted to the neonatal intensive care unit can suffer from various respiratory diseases due to prematurity or abnormality. Tracheomalacia (TM) is an airway condition characterized by airway collapse during breathing. Newborns diagnosed with TM may require respiratory support for breathing and there is no reliable method to quantify the breathing effort. The standard diagnosis for TM is bronchoscopy. However, bronchoscopy cannot precisely evaluate the severity of the disease and measure the effect of airway motion on airflow. This study aims to quantify airflow measurements such as work of breathing, airway resistance, and pressure in the central airway (trachea and main bronchi). Magnetic resonance imaging (MRI) was used to obtain the airway anatomy and motion during the breathing cycle. The acquired MR images were reconstructed based on respiration to obtain four MR images that show four main breathing phases (end expiration, peak inspiration, end inspiration, and peak expiration). Airway surfaces were segmented from MR images to create virtual airway models. Surface registration between the airway surfaces at each phase of breathing was used to obtain the physiologic motion during the breathing cycle. However, MRI cannot quantify airflow measurements alone. Computational fluid dynamics (CFD) is a well-known technique to model the airflow in airway models derived from MRI. Virtual airway models, airflow rates and airway motion were obtained for each subject and used as inputs for the CFD simulation. The main bronchi's airflow rates were obtained using the lung tidal volumes and the free induction decay waveform. Using these techniques, three studies were performed to investigate the effect of TM on neonatal respiration. The first study investigates the effect of airway motion on breathing by comparing airflow measurements in dynamic airways with static airways in four subjects with TM and without TM. Results indicated that CFD

simulations should be performed using dynamic airway models and when dynamic imaging is not available, static imaging should be acquired at the correct phase of breathing. The second study calculates the increase in tracheal resistive work of breathing per day due to airway motion using 14 neonatal subjects (8 TM, 6 non-TM). For each subject, 2 CFD simulations were performed. The first simulation used an airway model with dynamic airway motion and the second simulation used a static airway which represented the biggest airway of each subject. The study showed that neonates with TM have a nearly five times increase in breathing effort due to airway motion compared to the static airway. The third study investigates the effect of the glottis on airflow in 21 neonatal subjects (11 TM, 10 non-TM). The glottis motion during the breathing cycle was measured and the total pressure loss along the airway was calculated using individual CFD simulations. The study showed that neonates with TM self-generate positive end expiratory pressure (auto-PEEP) by narrowing their glottises during breathing. The studies presented in this dissertation provide clinically relevant information that can enhance patient care and health based on MRI and CFD, both of which rely on basic Physics principles.

Acknowledgements

First of all, I wish to express my deepest gratitude to my research advisor, Professor Jason Woods for all his guidance, assistance, motivation, and financial support during all these years. I wanted to learn a new field of study when I enrolled in the Physics PhD program, and I am grateful for the opportunity you have given me. I am extremely grateful to Dr. Alister Bates for his guidance and support throughout this work. I was inspired to study computational fluid dynamics after seeing cool videos on airflow in the airway, and I am grateful for his mentorship and friendship. I would like to extend my gratitude to Professors Zackary Cleveland, David Mast, and Rohana Wijewardhana for serving on my defense committee and for providing me with helpful advice.

I would like to acknowledge all members of the Center for Pulmonary Imaging Research (CPIR) for their friendship and support. I learned many skills working with you all and I had a great time at the CPIR. I would also like to thank all the collaborators from the University of Wisconsin-Madison and Imperial College London for their contributions to this work. I am thankful to Dr. Robert Fleck and Dr. Erik Hysinger for their advice and support. I convey my deepest gratitude to all neonatal intensive care unit staff, patients, and their parents for their participation in this research. Finally, I would like to express my appreciation to my lovely wife, Dewmi, my parents, brother, and sister for believing in me and supporting me achieve this milestone.

Table of Contents

List of Figures

List of Tables

List of Abbreviations

BEF	Bronchoesophageal fistula
BPD	Bronchopulmonary dysplasia
CFD	Computational fluid dynamics
COPD	Chronic obstructive lung disease
CPAP	Continuous positive airway pressure
CT	Computed tomography
DNS	Direct numerical simulation
EA	Esophageal atresia
FEV_1	Forced expiratory volume in 1 second
FID	Free induction decay
HFNC	High flow nasal cannula
LES	Large eddy simulation
MRI	Magnetic resonance imaging
NICU	Neonatal intensive care unit
NMR	Nuclear magnetic resonance
PEEP	Positive end expiratory pressure
PMA	post-menstrual age

RF	Radio-frequency
TEF	Tracheoesophageal fistula
TM	Tracheomalacia
TR-WOB	Tracheal resistive work of breathing
UTE	Ultrashort echo time
WALE	Wall-adapting local eddy-viscosity
WOB	Work of breathing

1 Human Respiratory System

This chapter covers the anatomy of the human respiratory system and illnesses affecting the airway and lungs. The respiratory system includes the airways, lungs, and pulmonary blood vessels. The main purpose of the respiratory system is gas exchange. This study focuses on newborns with tracheomalacia (TM) who are admitted to the neonatal intensive care unit (NICU).

1.1 Airway

The primary function of the airways is to transfer air in and out of the lungs to perform gas exchange: inhaled O_2 into hemoglobin and the exhalation of CO_2. The respiratory tract is divided into two regions, upper airway and lower airway/lung. The upper airway includes the nasal cavity to larynx and the lower airway includes trachea to alveoli in the lungs. One of the functions of the upper airway is to warm inhaled air to body temperature [1]. The upper airway is not the focus of this thesis, but it is required as the inflow to the larynx.

This thesis investigates the airflow in the larynx and the central airway, which includes the trachea and the main bronchi. The trachea is commonly known as the windpipe and it is composed of incomplete cartilage rings, forming a “C”-shape. In the opening of the “C”, a membrane called the trachealis allows the trachea to change size and shape during breathing. In preterm newborns, the internal diameter of the trachea varies between 2 - 4 mm [2]. The main bronchi that are connected to the left and right lungs are attached to trachea at the carina. The larynx is commonly referred to as the voice box. The main functions of the larynx are protecting the lower airways from food aspiration and producing sound. The opening between the vocal folds in the larynx is called the glottis and is capable of controlling airflow to the lungs [3]. Furthermore, the glottis is

usually the narrowest location of the airway and therefore is responsible for a large proportion of airway resistance [4,5].

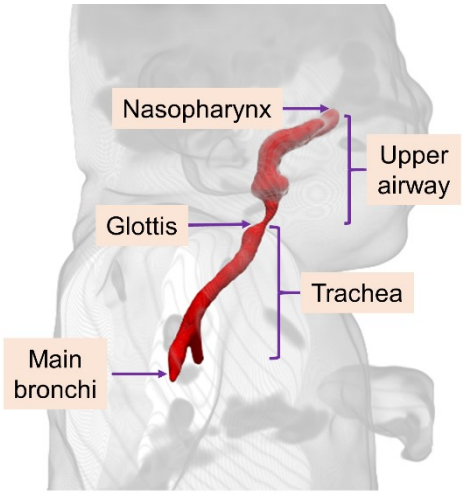

Figure 1.1: Neonatal airway from nasopharynx to main bronchi

When the thorax enlarges, the pressure inside the pleural cavity (intrapleural pressure) falls below atmospheric pressure during inspiration. As a result, air flows in. When the thorax compresses, air flows out during expiration due to the elevated pressure in the pleural cavity. Figure 1.2 indicates the pressure inside the pleural cavity and airways relative to atmospheric pressure.

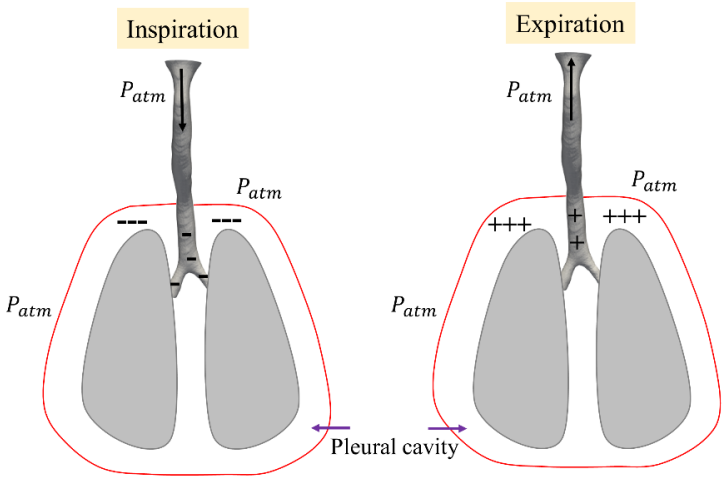

Figure 1.2: Airway pressure during breathing. Black arrows denote the airflow direction and P_{atm} stands for atmospheric pressure.

1.2 Airway Diseases

In this research study, neonates with airway diseases such as TM and tracheoesophageal fistula/ esophageal atresia (TEF/EA) are investigated.

1.2.1 Tracheomalacia

In pediatrics, TM is an airway condition due to dynamic collapse in the trachea during breathing. One of the causes of the dynamic collapse is the softness in the tracheal cartilage [6,7]. The trachea also narrows during expiration due to increased intrapleural pressure in the pleural cavity [8]. According to previous studies, there is at least one pediatric subject diagnosed with TM for every 2100 children [9–11]. The gold standard for diagnosing TM is bronchoscopy [12]. Although, current studies have proposed various methods to diagnose TM via imaging, such as magnetic resonance imaging (MRI) and computed tomography (CT) [13–15]. These studies have measured the cross-sectional area change during inspiration and expiration to quantify the differences in health and disease subjects. Figure 1.3 demonstrates the difference between the cross-sectional area in a subject with and without TM.

Neonates with TM have breathing difficulties due to dynamic collapse. Newborns may require positive pressure support using high flow nasal cannula (HFNC) or RAM continuous positive airway pressure (CPAP) to keep the airway lumen open during breathing [6,16,17]. More severe cases are intubated using an endotracheal tube or use mechanical ventilation to support breathing [18]. Several surgical procedures such as aortopexy, tracheopexy, and stent placement are necessary to manage severe TM cases [6,7]. Newborns with TM are often comorbid with other diseases, such as bronchopulmonary dysplasia (BPD) and TEF/EA [9,10,19]. Currently, there is no technique to quantify the effect of dynamic collapse and how it affects airflow during breathing.

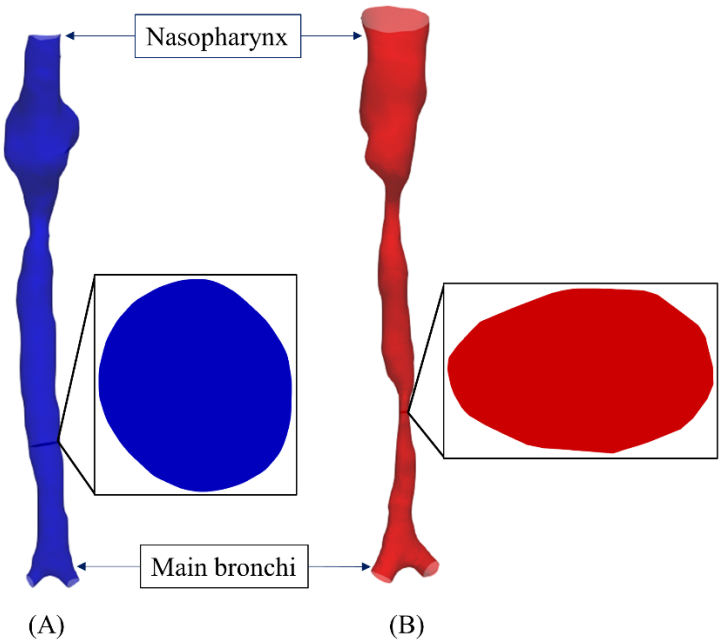

Figure 1.3: Mid-tracheal cross-section in a subject without TM (A) and with TM (B) at peak expiration. The subject without TM has a more circular cross-sectional plane than the subject with TM.

1.2.2 Tracheoesophageal Fistula/ Esophageal Atresia

Tracheoesophageal fistula (TEF), a congenital abnormality where trachea and esophagus are connected. Esophageal atresia (EA) is a condition in which the esophagus is split into two tubes that are not connected. TEF/EA may occur in a newborn in five different forms and the most common of which is Type C, where the lower esophagus is attached to the trachea [20][21]. Figure 1.4 illustrates the differences between each type of TEF/EA.

The prevalence of TEF/EA is 1:2500 to 1:4000 in newborns [22]. Newborns with TEF/EA have breathing difficulties and may exhibit respiratory distress [23]. In addition, vomiting, coughing, and choking are some of the symptoms due to aspiration [24]. Ultrasound scans can be

used to detect TEF/EA before birth and chest x-ray is used to diagnose after birth [21,25]. Surgery is needed to connect the two ends of the esophagus or/and to remove the fistula [26].

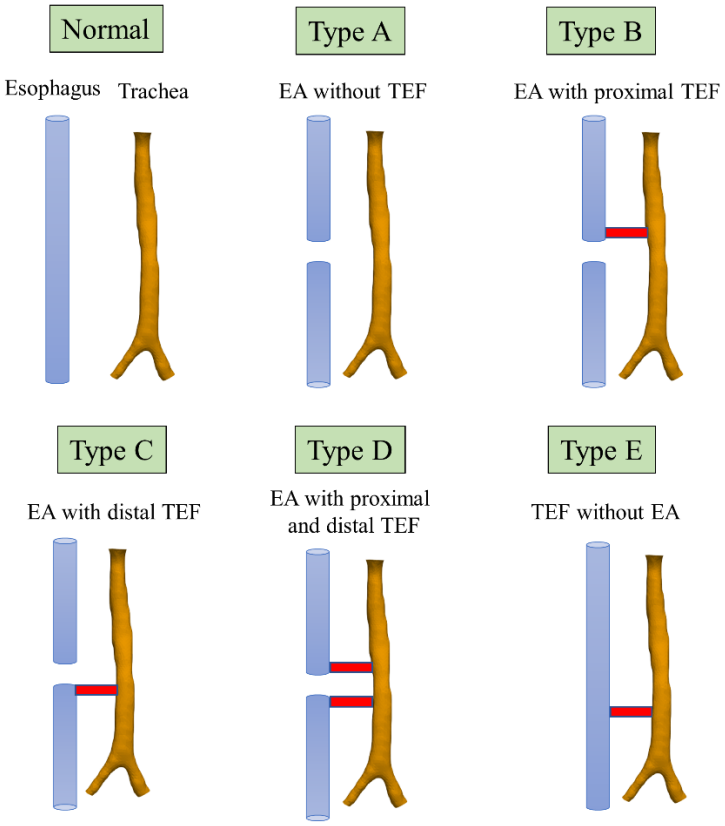

Figure 1.4: Types of tracheoesophageal fistula/ esophageal atresia.

1.3 Lungs

The core function of the lungs is to provide oxygen into the bloodstream while also removing carbon dioxide. There are approximately 23 branching tubes starting from the trachea to alveolar sacs [27]. The first 17 generations are in the conducting zone (largely governed by pressure-driven flow) and the rest of the generations are in the respiratory zone (largely governed by thermal diffusion). The airway volume in the conducting zone is called the dead space (~ 130-180 ml) and the respiratory zone performs the gas exchange [27].

During inspiration, the diaphragm (muscle underneath the lungs) contracts to create negative intrapleural pressure allowing air to flow in. During expiration, the lungs deflate on their own due to the elastic nature. In most cases, the right lung is bigger than the left lung. Small airways in the respiratory zone begin to grow during the later weeks of gestation. Prematurely born neonates have underdeveloped lungs that are unable to function. The increased intrapleural pressure in the thorax affects the airflow in the trachea, particularly during expiration. BPD is one of the lung diseases associated with premature newborns.

1.4 Bronchopulmonary Dysplasia

BPD is a serious pulmonary disease caused by preterm birth, which requires respiratory support to survive during the early stage of life. The definition of BPD is newborns receiving oxygen therapy for at least 28 days and based on the respiratory support at 36 weeks post-menstrual age (PMA) [28]. Based on the severity, it is further divided into three categories, mild, moderate, and severe. There are more than 10,000 cases in the United States every year [28–30].

BPD is mainly evaluated using Chest x-ray and CT. However, these imaging techniques expose neonatal subjects to ionizing radiation. Recent studies show that MRI can be used to evaluate subjects with BPD and correlates well with MRI findings [31–33]. Higano et al. [31] showed that lung disease severity based on Ochiai scoring [33] has a significant correlation with respiratory support at the NICU discharge ($p < 0.0001$). Subjects with BPD also have airway issues such as tracheobronchomalacia, which require treatment. In addition to respiratory support, subjects with BPD receive diuretics to clear excess water in the lungs, bronchodilators to relax airway muscles, and anti-inflammatory medications to reduce swelling in the airways [34–36].

2 Nuclear Magnetic Resonance and Magnetic Resonance Imaging

2.1 Nuclear Magnetic Resonance

2.1.1 Nuclear Spin and Larmor Frequency

Nuclear spin, I is the total angular momentum of a nucleus. In 1922, Stern and Gerlach discovered that spin is quantized and is a fundamental magnetic property [37–39]. Nuclear spin varies from I = 0 to I = 8 in 1/2–unit increments. Nuclear spin is zero for nuclei with an even number of protons and neutrons such as ^{4}He and ^{16}O. Nuclear spin is a positive integer if the number of protons and neutrons are both odd numbers. The nuclear spin of ^{6}Li and ^{10}B is 1 and 3, respectively. Nuclear spin is a half-integral if the nuclei are a combination of odd/even or even/odd protons and neutrons. For example, ^{1}H, ^{129}Xe, ^{19}F, ^{31}P elements nuclear spin is ½.

In the presence of an external magnetic field, nuclei with non-zero nuclear spin align parallel or anti-parallel to the direction of the magnetic field and can be perturbed by an alternating field normal to the external field. This phenomenon is called nuclear magnetic resonance (NMR). Nuclear spin of ½ nuclei splits into two energy levels and the energy difference, ΔE can be written as,

$$\Delta E = hf \tag{2.1}$$

where h is the Planck constant (6.626 x 10^{-34} Js) and f is the frequency of the absorbed or emitted electromagnetic energy.

The precession rate of the nuclear spin is defined as the Larmor frequency, ω_0.

$$\omega_0 = \gamma B_0 \tag{2.2}$$

where γ is the gyromagnetic ratio which depends on the nuclei and B_0 is the external magnetic field.

2.1.2 Magnetization Vector Components

Let's consider a spin ensemble in an external magnetic field, $\vec{B}_{ext}$ applied in z direction. The total magnetization, $\vec{M}$ can be expressed using the volume, V and the summation of each spin magnetic moment, $\vec{\mu}_i$ as,

$$\vec{M} = \frac{1}{V}\sum_i \vec{\mu}_i \tag{2.3}$$

Neglecting the each spin ½ interaction with the surrounding, individual spins interaction can be written using the equation of motion as,

$$\frac{1}{V}\sum_i \frac{d\vec{\mu}_i}{dt} = \frac{\gamma}{V}\sum_i \vec{\mu}_i \times \vec{B}_{ext} \tag{2.4}$$

Equation *(2.4)* reduces to,

$$\frac{d\vec{M}}{dt} = \gamma\vec{M} \times \vec{B}_{ext} \tag{2.5}$$

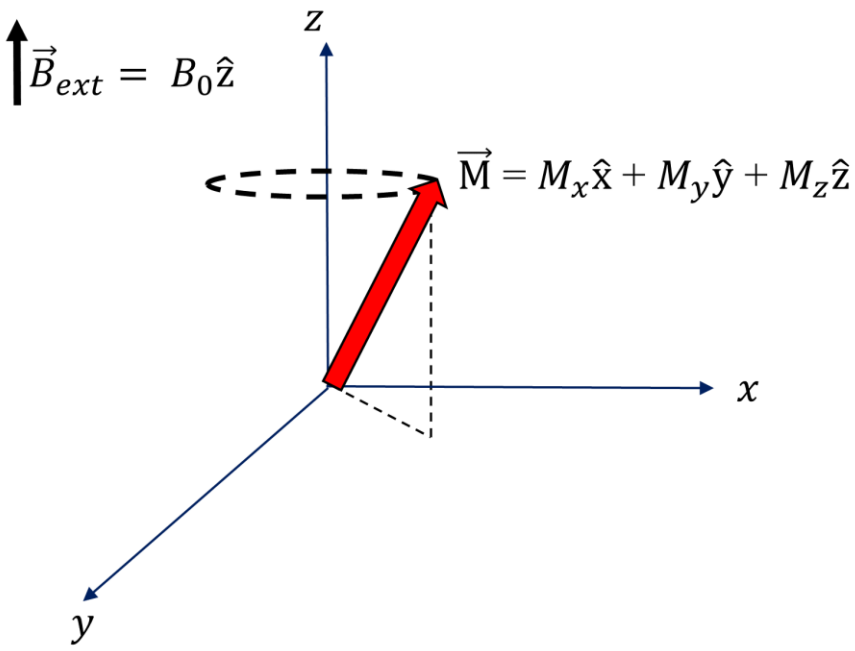

Figure 2.1: Magnetization vector in a spin ensemble

The longitudinal component of the magnetization vector, $\vec{M}_{||}$ can be written as,

$$\vec{M}_{||} = M_z\hat{z} \tag{2.6}$$

The transverse component of the magnetization vector, $\vec{M}_{||}$ can be written as,

$$\vec{M}_{\perp} = M_x\hat{x} + M_y\hat{y} \tag{2.7}$$

Using equations *(2.5), (2.6),* and *(2.7),*

$$\frac{dM_z}{dt} = 0 \tag{2.8}$$

$$\frac{d\vec{M}_{\perp}}{dt} = \gamma\vec{M}_{\perp} \times \vec{B}_{ext} \tag{2.9}$$

2.1.3 Free Induction Decay

The net magnetization vector at thermal equilibrium points in the same z direction as the external magnetic field.

The total magnetization, M_0 at thermal equilibrium can be expressed for a spin ½ case as follows.

$$M_z = M_0 = \frac{\rho\gamma^2\hbar^2}{4kT}B_0 \qquad (\hbar\omega_0 \ll kT) \tag{2.10}$$

where ρ is the spin density and $\hbar = \frac{h}{2\pi}$.

When a pulsed magnetic field ($\overrightarrow{B_1}$) applied in the transverse plane orthogonal to $\vec{B}_{ext} = B_0\hat{z}$ by using a radio-frequency (RF) coil, the ensemble magnetization starts rotating in the direction of the applied magnetic field, $\overrightarrow{B_1}$. After the pulsed magnetic field, the net magnetization vector pointed in the transverse direction precesses about the z-axis at the Larmor frequency. The induced signal due to change of magnetization can be detected using a LC circuit (often the same coil as used for transmission) and the receiver signal is called the free induction decay (FID). The angle of rotation, which is known as flip angle (β) measured from the z-axis depends on the applied RF pulse duration, τ and the strength, B_1.

$$\beta = \gamma B_1 \tau \tag{2.11}$$

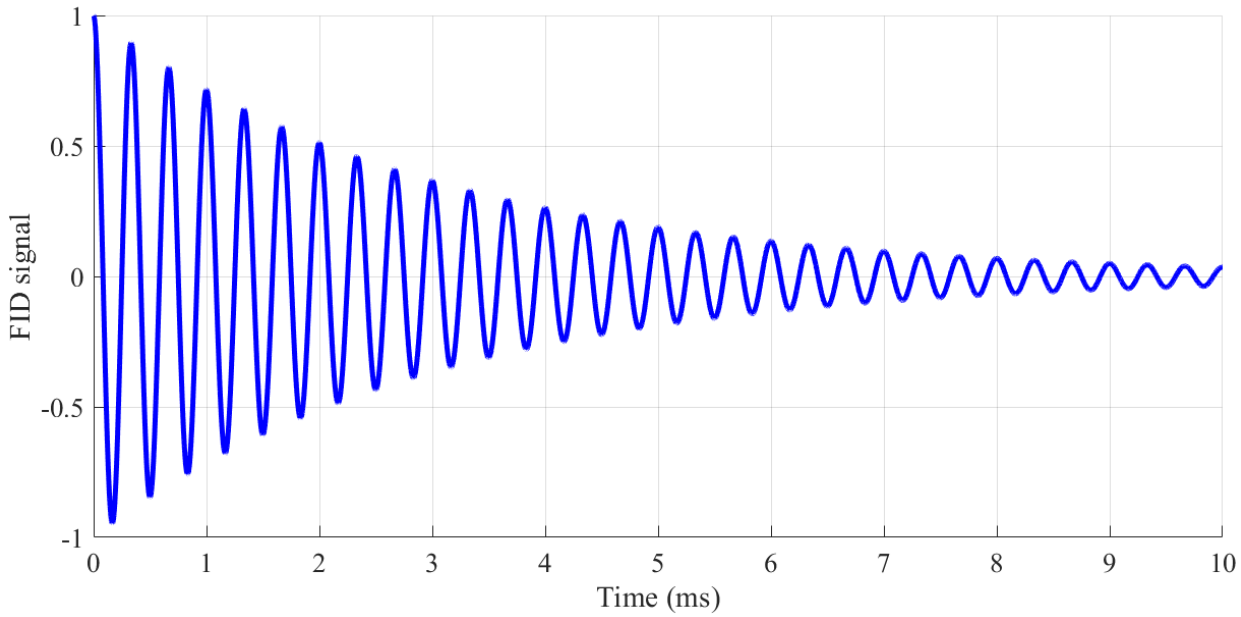

Figure 2.2: Free induction decay signal at off-resonance frequency of 3 kHz.

2.1.4 Relaxation Times

After applying a RF pulse, FID signal decays over time exponentially as shown in the above Figure 2.2. There are two types of relaxation time constants.

The first type of relaxation, T_1 is known as spin-lattice relaxation. Spins transmit energy to the environment (lattice) and the longitudinal magnetization vector recovers in the direction of the magnetic field B_0. The rate of change in longitudinal magnetization can be expressed as follows.

$$\frac{dM_z}{dt} = \frac{1}{T_1}(M_0 - M_z) \tag{2.12}$$

Assuming no induced longitudinal magnetization at t = 0, the solution of the above equation can be written as,

$$M_z(t) = M_0\left(1 - e^{-t/T_1}\right) \tag{2.13}$$

The second type of relaxation, T_2 is known as spin-spin relaxation. Spins within the ensemble dephase over time due to changes in the magnetic fields. The net magnetization vector rotates in the x-y plane and the transverse magnetization can be written as follows.

$$\frac{d\vec{M}_{\perp}}{dt} = \gamma \vec{M}_{\perp} \times \vec{B}_{ext} - \frac{1}{T_2} \vec{M}_{\perp} \tag{2.14}$$

A simplified solution of the above equation can be written as,

$$\vec{M}_{\perp}(t) = M_0 e^{-t/T_2} \tag{2.15}$$

The transverse magnetization decays faster due to inhomogeneity of the static magnetic field, $\vec{B}_{ext}$. The observed T_2 is called T_2^* and it is always shorter than or equal to true T_2 initiated by atomic and molecular interactions.

$$\frac{1}{T_2^*} = \frac{1}{T_2} + \frac{1}{T_{2,inhomg}} \tag{2.16}$$

The rate of change of the magnetization vector can be written by combining equations *(2.12)* and *(2.14)* as,

$$\frac{d\vec{M}}{dt} = \gamma \vec{M} \times \vec{B}_{ext} + \frac{1}{T_1}(M_0 - M_z)\hat{z} - \frac{1}{T_2} \vec{M}_{\perp} \tag{2.17}$$

This vector equation is known as Bloch equation.

2.2 Magnetic Resonance Imaging

The concepts described under NMR are used in magnetic resonance imaging (MRI). The human body is up to 60% water, which consists largely of hydrogen atoms [40]. The water percentage in a healthy newborn and a premature newborn is approximately 70% and 80%, respectively [41]. In the presence of an external static magnetic field, a spatially changing magnetic field (that is, a field gradient) allows spatial localization of signal via spatially changing frequency. The detected frequencies and phases can spatially map to an image using the Fourier Transform.

2.2.1 Fourier Transform

The Fourier transform is a mathematical technique that can be used to decompose the output signal of the MR into a frequency domain.

The continuous Fourier transform and inverse Fourier transform as follows.

$$\mathcal{F}\{f(x)\} = g(k) = \int_{-\infty}^{+\infty} f(x)e^{-i2\pi kx}dx \tag{2.18}$$

$$\mathcal{F}^{-1}\{g(k)\} = f(x) = \int_{-\infty}^{+\infty} g(k)e^{i2\pi kx}dk \tag{2.19}$$

where $f(x)$ represents the spatial domain function and $g(k)$ represents the frequency domain function.

2.2.2 k-Space

In MR physics, k-space represents the spatial frequencies of the MR image. The Fourier transform is used to decompose k-space ($\mathrm{g}(\mathrm{k_x}, \mathrm{k_y}, \mathrm{k_z})$) data to image-space ($\mathrm{f}(\mathrm{x}, \mathrm{y}, \mathrm{z})$) either in two-dimensions or three-dimensions.

$$\mathcal{F}\{f(x,y,z)\} = g(k_x,k_y,k_z) = \iiint_{-\infty}^{+\infty} f(x,y,z)e^{-i2\pi(k_x x+k_y y+k_z z)}dxdydz \quad (2.20)$$

$$\mathcal{F}^{-1}\{g(k_x,k_y,k_z)\} = f(x,y,z) = \iiint_{-\infty}^{+\infty} g(k_x,k_y,k_z)e^{i2\pi(k_x x+k_y y+k_z z)}dk_x dk_y dk_z \quad (2.21)$$

2.2.3 Spatial Encoding Gradients

In MRI, there are three different magnetic field gradients applied consecutively to localize spins spatially. They are slice selection, phase encoding, and frequency encoding gradients.

Consider a volume element with spin density $\rho(x,y,z)$ at $z_0\hat{z}$. If the thickness of the slice is Δz, the frequency of the spins in that volume element can be written as,

$$\Delta\omega = \gamma G_{ss}\Delta z \quad (2.22)$$

where $\Delta\omega$ represents the applied RF pulse bandwidth and G_{ss} is the slice selection gradient.

After the slice selection, phase encoding gradient, $B_z(y) = G_{PE}y$ is applied perpendicular to the slice axis for a time period of τ.

Frequency encoding gradient, $B_z(x) = G_{FE}x$ is also known as readout gradient, is applied perpendicular to both slice selection and phase encoding gradients for a time period of t.

The acquired signal can be written as follows.

$$s(G_{PE},t) = \iint \rho(x,y,z_0)e^{-i(\gamma y G_{PE}\tau+\gamma x G_{FE}t)}dxdy \quad (2.23)$$

$$s(k_x, k_y) = \iint \rho(x, y, z_0) e^{-i2\pi(k_x x + k_y y)} dx dy \quad (2.24)$$

where $k_x = \frac{\gamma}{2\pi} G_{FE} t$ and $k_y = \frac{\gamma}{2\pi} G_{PE} \tau$.

2.3 Ultrashort Echo Time MRI

Imaging of the lungs is challenging due to low proton density in the lung parenchyma and shorter T_2^* (~2 ms) due to inhomogeneous magnetic susceptibility of the lungs [42–44]. X-ray CT has been used as the traditional method of imaging the lungs. However, CT exposes patients to high doses of ionizing radiation, which increases the risks of cancer [45,46]. Previous studies have shown that pediatrics have a higher risk of cancer than adults as a result of CT [47,48].

For neonates, MRI is the most suitable imaging method as this technique does not expose to ionizing radiation and does not require sedation. Ultrashort echo time (UTE) technique acquires raw data starting at the center of k-space and uses radial pseudo-randomized sampling scheme. This technique has improved the signal-to-noise ratio in the lung tissue by reducing echo time to 0.2 ms (echo time is defined as the duration between the mid-point of the RF pulse and the beginning of the data acquisition) [49–52]. This short echo time allows rapid data sampling after spin excitation. In this work, 3D radial UTE MRI was performed for each neonate at 1.5 T scanner sited within the NICU. The following imaging parameters were applied [53–55].

Table 2.1: UTE MRI parameters

Imaging parameter	Value
Image resolution	0.7 mm (3D isotropic)
Flip angle	5°
Echo time	200 μs
Repetition time	5.2 ms
Number of projections	~200,000
Field of view	18 cm
Scan time	~16 minutes

2.4 Respiratory Gated UTE MR Images

Previous studies have reported that the magnitude or phase of the initial point of each FID signal can be used to trace physiologic motion at the time of MRI [55–60]. This is only possible with center-out trajectories and the following Figure 2.3 shows the modulation of the initial magnitude of FID signal due to the neonate's quiescent breathing and bulk motion. The time intervals caused by the bulk motion of neonates can be easily determined. The removal of bulk motion increases image quality and decreases motion blurring in non-sedated neonates.

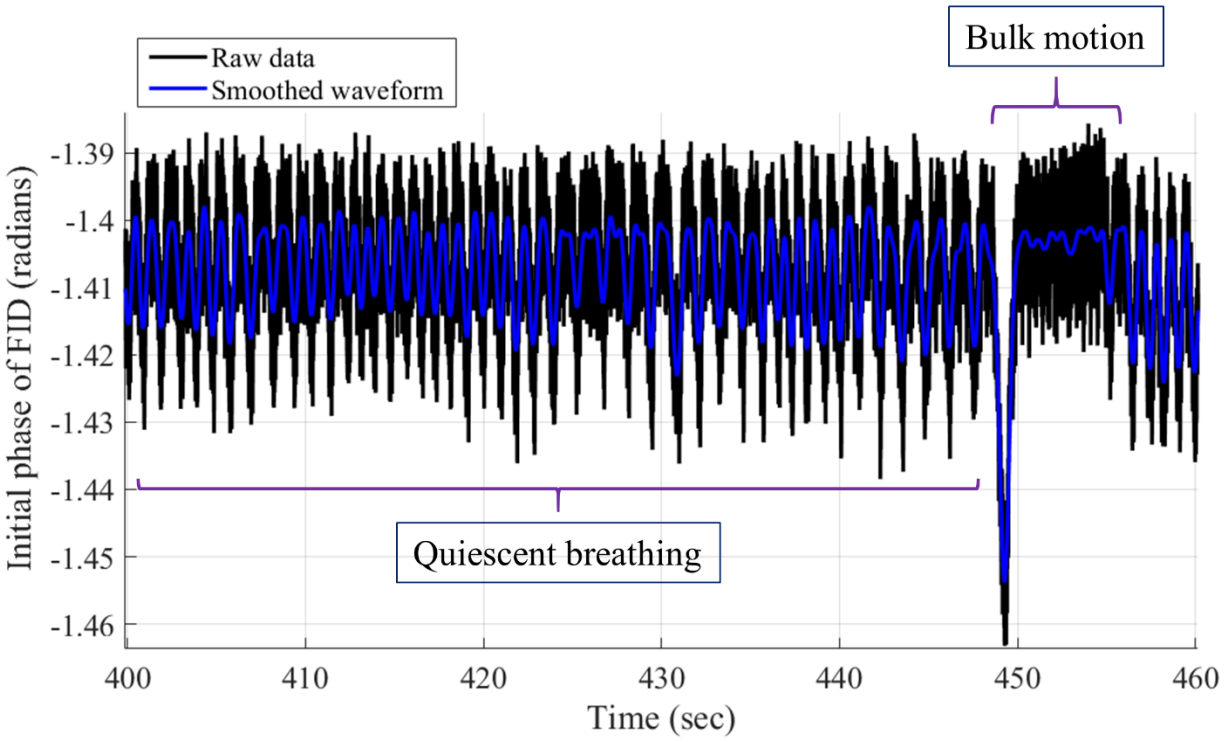

Figure 2.3: Initial phase of FID signal due to quiescent breathing and bulk motion. Raw data and smoothed waveform are shown in black and blue, respectively.

Higano et al. [55] have shown that UTE MR images can be reconstructed after removing bulk motion. Since this method acquires k-space projections in a pseudo-random order, the entire k-space is still covered uniformly. These images show less blurring and the signal-to-noise ratio of the lung parenchymal and airway are accurate, compared to images with bulk motion. Furthermore, these MR images can be gated based on breathing and reconstructed to achieve images showing various stages of breathing such as end inspiration and end expiration [55,61,62].

In this work, MR images of each neonate were gated based on breathing to obtain four images that demonstrate four phases during breathing (i.e. end expiration, peak inspiration, end inspiration, and peak expiration) [54,55,60]. Matlab R2019b (The MathWorks, Inc.) software was used to process the FID data. The magnitude or phase of the FID signal was selected based on the

signal-to-noise ratio of the respiratory signal (peak-to-peak). After removing the bulk motion, a low-pass filter was applied to obtain the smoothed waveform shown in Figure 2.4A. The frequency that corresponds to the highest peak in the amplitude spectrum of the FID was used as the low-pass frequency.

Each breath, inspiration and expiration phase amplitudes were used to assign projections for each respiratory phase bin (end expiration, peak inspiration, end inspiration, and peak expiration). Data points from the center of the end expiration time point to the center of the end inspiration time point were assigned into four bins based on the inspiration phase-amplitude as a percentage (end expiration- 12.5%, peak inspiration- 25%, end inspiration- 12.5%, discarded data- 50%). Similarly, expiration phase-amplitude was used to assign data points into four bins (end inspiration- 12.5%, peak expiration- 25%, end expiration- 12.5%, discarded data- 50%). Note that data between these bins were discarded to reduce motion blurring (discarded data is shown in brown, Figure 2.4A). The sampling density compensation method was used to reconstruct each respiratory phase image [49,63,64].

Figure 2.4B compares the tracheal cross-section in a subject with TM at each phase of breathing. The tracheal cross-sectional was smaller in the end expiration time point than at the end inspiration time point. The peak inspiration and peak expiration images demonstrate intermediate changes of the tracheal cross-section.

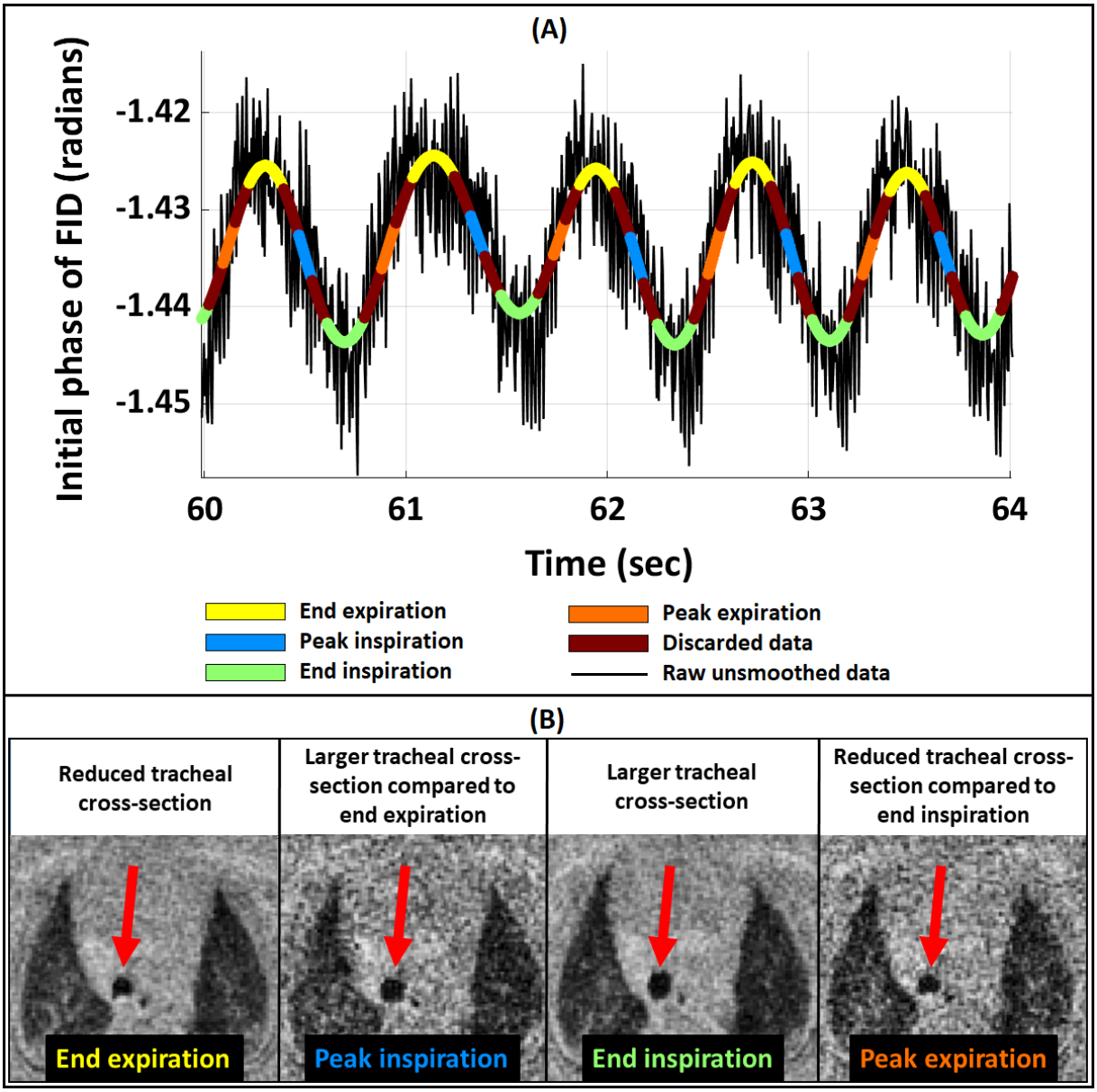

Figure 2.4: (A) Initial phase of the FID waveform over a 4s window during the MRI scan. Raw data colored in black and smoothed waveform was divided into four bins based on respiration (end expiration-yellow, peak inspiration-blue, end inspiration-green, and peak expiration-orange). (B) Axial plane of the thorax in a subject with TM at each phase of breathing. Reprinted with permission of the American Thoracic Society. Copyright © 2021 American Thoracic Society. All rights reserved [54].

The entire FID waveform was used after removing bulk motion to obtain the ungated image, representing an average image taken over many breathing cycles during the scan. Figure 2.5 compares an ungated image and a gated image at end expiration of a neonatal subject with TM. The image on the left was blurred due to motion compared to the gated image on the right.

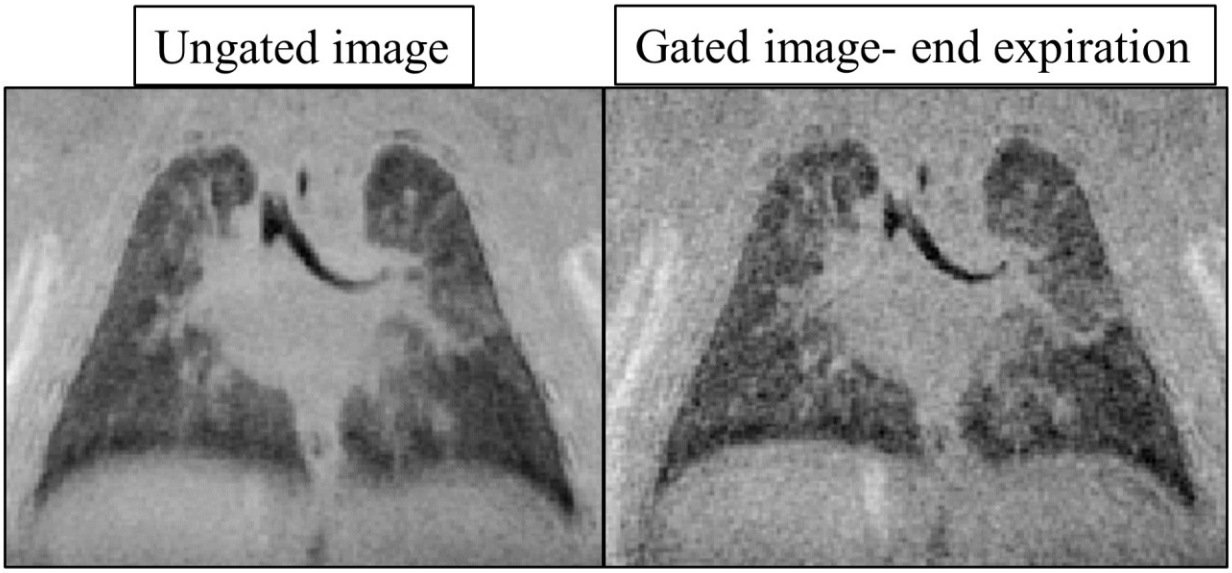

Figure 2.5: Comparison of the ungated image and the gated image (coronal plane). The gated image represents the end expiration time point.

3 Computational Fluid Dynamics

3.1 CFD Basics

Computational fluid dynamics (CFD) simulations are based on mathematical modeling and numerical methods. Basic Physics principles are applied in CFD to study a fluid problem. In CFD, all liquids and gases are considered fluids. The conservation of mass, conservation of momentum, and conservation of energy are the main principles used in CFD. The Navier-Stokes equations, which describe the fluid flow, are based on these principles.

3.1.1 Conservation of Mass

Fluid mass cannot be created or destroyed. For example, let's consider a stationary cylindrical pipe where water flows from A to B as shown in Figure 3.1. The water flow rate at A is equal to the water flow rate at B.

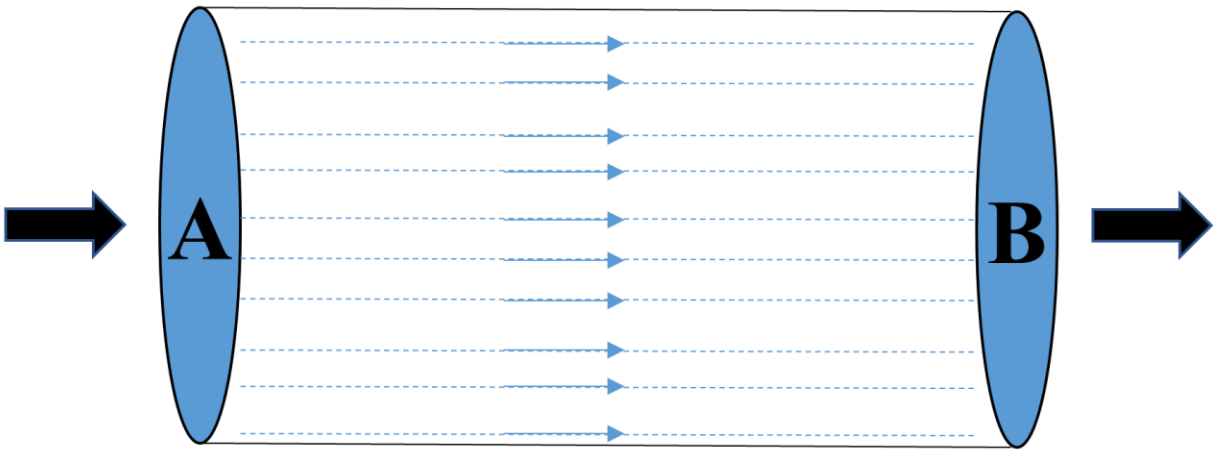

Figure 3.1: A cylindrical pipe with water flowing from A to B. The water flow rate at A and B cross-sections are equal.

The change of mass, m can be written as,

$$\frac{dm}{dt} = \dot{m}_A - \dot{m}_B \tag{3.1}$$

Since, $\dot{m}_A = \dot{m}_B$,

$$\frac{dm}{dt} = 0$$

$$m = \text{constant} \tag{3.2}$$

Continuity equation

Let's consider a control volume with dimensions dx, dy, and dz.

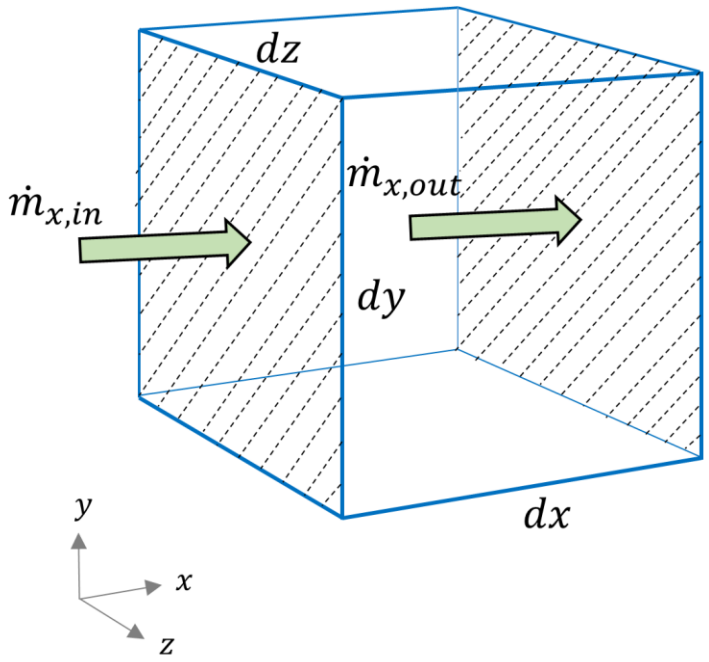

Figure 3.2: A stationary control volume where mass is flowing in x direction

The mass flow through $dydz$ surface can be written as,

$$\dot{m}_{x,in} = \rho u dydz \tag{3.3}$$

where ρ, u represents the density and velocity of the fluid in x direction, respectively.

Inside the control volume, fluid has traveled a distance dx and has a different velocity than u at the beginning.

The change in mass along dx can be written as,

$$d\dot{m}_{x,in} = \frac{\partial(\rho u)}{\partial x} dx \tag{3.4}$$

Therefore, $\dot{m}_{x,out}$ is the addition of change in mass and the mass flowing into the control volume.

$$\dot{m}_{x,out} = \left(\rho u + \frac{\partial(\rho u)}{\partial x} dx\right) dydz \tag{3.5}$$

The mass flow difference in the x direction is,

$$\dot{m}_{x,in} - \dot{m}_{x,out} = -\frac{\partial(\rho u)}{\partial x} dxdydz \tag{3.6}$$

Similarly, the mass flow difference can be written in y and z directions. If the mass flowing velocities in y and z directions are v and w, the total mass flow difference is,

$$\sum \dot{m}_{in} - \sum \dot{m}_{out} = -\frac{\partial(\rho u)}{\partial x} dxdydz - \frac{\partial(\rho v)}{\partial y} dxdydz - \frac{\partial(\rho w)}{\partial z} dxdydz \tag{3.7}$$

Since our control volume ($\rho dxdydz$) is fixed, the mass flow difference can be expressed as,

$$\frac{\partial m}{\partial t} = \frac{\partial \rho}{\partial t} dxdydz \tag{3.8}$$

Using equations *(3.7)* and *(3.8)*,

$$\frac{\partial \rho}{\partial t} dxdydz = -\frac{\partial(\rho u)}{\partial x} dxdydz - \frac{\partial(\rho v)}{\partial y} dxdydz - \frac{\partial(\rho w)}{\partial z} dxdydz$$

$$\frac{\partial \rho}{\partial t} = -\frac{\partial(\rho u)}{\partial x} - \frac{\partial(\rho v)}{\partial y} - \frac{\partial(\rho w)}{\partial z} \qquad (3.9)$$

Equation *(3.31)* can be written in vector form using the velocity vector $\mathbf{u} = (u, v, w)$

$$\frac{\partial \rho}{\partial t} + \nabla \cdot \rho \mathbf{u} = 0 \qquad (3.10)$$

Equation *(3.10)* is called the continuity equation and it represents the conservation of mass.

For incompressible fluids, ρ is constant and continuity equation simplifies to

$$\nabla \cdot \mathbf{u} = 0 \qquad (3.11)$$

The above equation represents that to keep the density of the fluid constant, the divergence of the fluid velocity is zero. In this work, air density was assumed to be constant.

3.1.2 Conservation of Momentum

Newton's second law of motion is applied to demonstrate the conservation of momentum. Let's assume our control volume shown in Figure 3.2 now moves in x direction with a velocity u. The mass of the control volume is $\rho dxdydz$ and this volume may have an acceleration (a_x) in the x direction.

Since velocity u depends on x, y, z, and t, using the chain rule,

$$a_x = \frac{du}{dt} = \frac{\partial u}{\partial t}\frac{dt}{dt} + \frac{\partial u}{\partial x}\frac{dx}{dt} + \frac{\partial u}{\partial y}\frac{dy}{dt} + \frac{\partial u}{\partial z}\frac{dz}{dt} \qquad (3.12)$$

Equation *(3.12)* can be expressed using velocity components u, v, and w in x, y, and z directions, respectively.

$$a_x = \frac{du}{dt} = \underbrace{\frac{\partial u}{\partial t}}_{\text{Local acceleration}} + \underbrace{u\frac{\partial u}{\partial x} + v\frac{\partial u}{\partial y} + w\frac{\partial u}{\partial z}}_{\text{Convective acceleration}} = \underbrace{\frac{Du}{Dt}}_{\text{Material derivative}} \tag{3.13}$$

Similarly, acceleration components in y and z directions can be derived as well. Using velocity vector $\mathbf{u} = (u, v, w)$, the material derivative is,

$$\frac{D\mathbf{u}}{Dt} = \frac{\partial \mathbf{u}}{\partial t} + (\mathbf{u} \cdot \nabla)\mathbf{u} \tag{3.14}$$

There are mainly 3 different forces acting on the control volume. They are called body forces, pressure forces, and viscous forces. The body force is due to the gravity acting on the control volume. The pressure forces act normal to the surface of the control volume and viscous forces are due to the friction. These viscous forces are also called surface forces that can act both normal and tangentially.

Let's define body force per unit mass as f_{Bx} and pressure forces acting normal to the surface as p and $p + \frac{\partial p}{\partial x}dx$ in x direction. The term $\frac{\partial p}{\partial x}dx$ is called the pressure gradient in x direction. As shown in Figure 3.3, there are six surface forces that act in x direction. These forces are called shear stress (τ) that acts parallel to the surface. For example, the shear stress acting on a plane normal to the y-axis in x direction is called τ_{yx}.

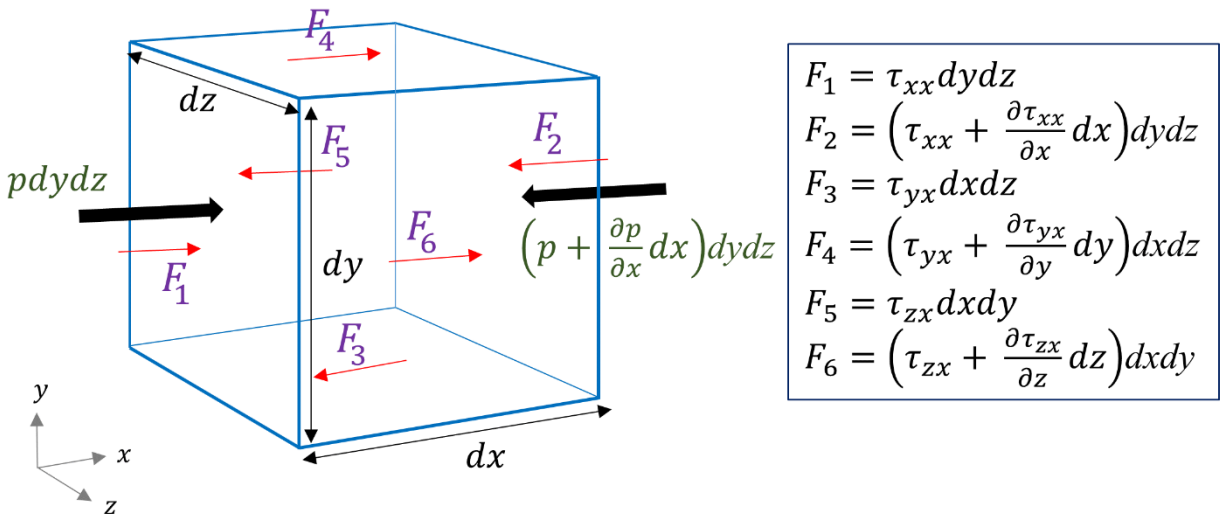

Figure 3.3: Forces act on control volume in x direction

All forces (F_x) act on the control volume in x direction can be written as,

$$F_x = f_{Bx}\rho dxdydz + \left[p - \left(p + \frac{\partial p}{\partial x}dx\right)\right]dydz + \left[\left(\tau_{xx} + \frac{\partial \tau_{xx}}{\partial x}dx\right) - \tau_{xx}\right]dydz$$
$$+ \left[\left(\tau_{yx} + \frac{\partial \tau_{yx}}{\partial y}dy\right) - \tau_{yx}\right]dxdz + \left[\left(\tau_{zx} + \frac{\partial \tau_{zx}}{\partial z}dz\right) - \tau_{zx}\right]dxdy \qquad (3.15)$$

After simplifying,

$$F_x = \left(f_{Bx}\rho - \frac{\partial p}{\partial x} + \frac{\partial \tau_{xx}}{\partial x} + \frac{\partial \tau_{yx}}{\partial y} + \frac{\partial \tau_{zx}}{\partial z}\right)dxdydz \qquad (3.16)$$

Since we know all forces, mass and acceleration of the control volume, we can write Newton's second law in x direction.

$$F_x = \rho dxdydz.a_x$$

$$\left(f_{Bx}\rho - \frac{\partial p}{\partial x} + \frac{\partial \tau_{xx}}{\partial x} + \frac{\partial \tau_{yx}}{\partial y} + \frac{\partial \tau_{zx}}{\partial z}\right) dxdydz = \rho dxdydz \frac{Du}{Dt}$$

$$f_{Bx}\rho - \frac{\partial p}{\partial x} + \frac{\partial \tau_{xx}}{\partial x} + \frac{\partial \tau_{yx}}{\partial y} + \frac{\partial \tau_{zx}}{\partial z} = \rho \frac{Du}{Dt} \qquad (3.17)$$

Similarly, we can apply Newton's second law in y and z directions as well. We can write equation *(3.17)* in vector form as,

$$\rho \mathbf{F_B} - \nabla p + \nabla \cdot \tau = \rho \frac{D\mathbf{u}}{Dt} \qquad (3.18)$$

where, $\mathbf{F_B}$ is the body force vector per unit mass, stress tensor (τ) = $\begin{bmatrix} \tau_{xx} & \tau_{xy} & \tau_{xz} \\ \tau_{yx} & \tau_{yy} & \tau_{yz} \\ \tau_{zx} & \tau_{zy} & \tau_{zz} \end{bmatrix}$.

Equations (3.18) and (3.10) are called the Navier-Stokes equations.

For incompressible fluids, τ can be written as,

$$\tau = \mu(\nabla \mathbf{u} + (\nabla \mathbf{u})^{\mathrm{T}}) \qquad (3.19)$$

where μ is the dynamic viscosity of the fluid.

Using equations (3.11), (3.14), (3.18), and (3.19)

$$\underbrace{\rho \mathbf{F_B}}_{\text{Body force}} - \underbrace{\nabla p}_{\text{Pressure force}} + \underbrace{\mu \nabla^2 \mathbf{u}}_{\text{Frictional force}} = \rho \underbrace{\left(\frac{\partial \mathbf{u}}{\partial t} + (\mathbf{u} \cdot \nabla)\mathbf{u}\right)}_{\text{Material derivative}} \qquad (3.20)$$

3.1.3 Conservation of Energy

The conservation of energy states that the total energy inside a closed system (control volume) is constant (energy cannot be created or destroyed). In this work, the air temperature inside the airway is assumed to be at 37 °C and no heat transfer to the surrounding area (i.e. isothermal and adiabatic process). More details on the first law of thermodynamics and how conservation of energy applied in fluid dynamics can be found in this book chapter [65].

3.2 Implementation for Solving Navier-Stokes Equations

The commercial CFD package, STAR-CCM+ (Siemens PLM Software) versions 11.06.011-R8 and 14.04.011-R8 were used in this work to solve Navier-Stokes equations for incompressible flow. These flow governing equations were discretized and solved using a segregated method [66–69].

Previous sections explained how mass, momentum and energy transport through the fluids. We can write the more general equation for momentum neglecting body force term,

$$\rho\left(\frac{\partial \mathbf{u}}{\partial t} + (\mathbf{u}\cdot\nabla)\mathbf{u}\right) = -\nabla p + \mu\nabla^2\mathbf{u} \qquad (3.21)$$

Using divergence theorem, the continuity equation for incompressible fluid derived in equation *(3.11)* can be written as,

$$\oint_A \mathbf{u}.da = 0 \qquad (3.22)$$

where da is the vector representing the surface of the fluid element.

The equation, *(3.21)* can be expressed in integral form as,

$$\underbrace{\frac{\partial}{\partial t}\int_V \rho \mathbf{u} dV}_{\text{Transient term}} + \underbrace{\oint_A \rho \mathbf{u} \otimes \mathbf{u} \cdot da}_{\text{Convective flux}} = \underbrace{-\oint_A p\mathbf{I} \cdot da}_{\text{Pressure gradient}} + \underbrace{\oint_A \tau \cdot da}_{\text{Viscous flux}} \qquad (3.23)$$

where V represents the cell volume, $\otimes$ represents the outer product, $\mathbf{I}$ is the identity matrix, and τ is the viscous stress tensor.

Equation *(3.21)* can be written for a scalar, $\emptyset$ with diffusion coefficient, D as,

$$\frac{\partial \rho \emptyset}{\partial t} + \nabla \cdot (\rho \mathbf{u} \emptyset) = \nabla \cdot (D \nabla \emptyset) \qquad (3.24)$$

Above equation can be written in integral form,

$$\frac{\partial}{\partial t}\int_V \rho \emptyset dV + \oint_A \rho \emptyset \mathbf{u} \cdot da = \oint_A D \nabla \emptyset \cdot da \qquad (3.25)$$

The transient term, the first term of the left-hand side denotes the time dependent of the fluid property $\emptyset$. The second term of the left-hand side indicates the changes due to convection of the fluid property. The right-hand side denotes the changes due to diffusion of the fluid property within the volume domain.

After applying integration approximations, equation *(3.25)* can be written in discrete form,

$$\frac{d}{dt}(\rho \emptyset V) + \sum_f [\rho \emptyset (\mathbf{u} \cdot \mathbf{a})]_f = \sum_f (D \nabla \emptyset \cdot \mathbf{a})_f \qquad (3.26)$$

where f denotes the face of each cell in the mesh.

In STAR-CCM+, second order implicit unsteady approach was implemented to discretize the transient term. The unsteady solver uses the solution at the current time point and the previous two time points. The convective flux term can be discretized as shown in equation (*3.27)*.

$$\left(\rho\emptyset(\mathbf{u}\cdot\mathbf{a})\right)_f = \left(\dot{m}\emptyset\right)_f = \dot{m}_f\emptyset_f \qquad (3.27)$$

where $\dot{m}_f$ represents the mass flow rate of the volume domain.

The diffusion term can be expressed in discrete form as,

$$(D\nabla\emptyset\cdot\mathbf{a})_f = D_f\nabla\emptyset_f\cdot\mathbf{a} \qquad (3.28)$$

where D_f denotes the harmonic average of the volume domains.

The diffusion flux of the interior face can be written using fluid properties $\emptyset_0$, $\emptyset_1$,

$$D_f\nabla\emptyset_f\cdot\mathbf{a} = D_f\left[(\emptyset_1 - \emptyset_0)\bar{\alpha}\cdot\mathbf{a} + \overline{\nabla\emptyset}\cdot\mathbf{a} - \left(\overline{\nabla\emptyset}\cdot\mathbf{ds}\right)\bar{\alpha}\cdot\mathbf{a}\right] \qquad (3.29)$$

where,

$\mathbf{ds}$ = distance between the neighboring cells

$$\alpha = \frac{\mathbf{a}}{\mathbf{a}\cdot\mathbf{ds}}$$

$$\overline{\nabla\emptyset} = \frac{(\nabla\emptyset_0 + \nabla\emptyset_1)}{2}$$

3.2.1 Large Eddy Simulation

Navier-Stokes equations are numerically solved without any turbulence model. However, it is computationally expensive and time consuming. To overcome these challenges, a turbulence model can be used. In this work, large eddy simulation (LES) mathematical model was applied to solve Navier-Stokes equations. In LES, large-scale turbulence is resolved and small-scale turbulence is modeled. LES acts as a low pass filter to Navier-Stokes equations.

In this technique, fluid property, u can be divided into a filtered value, $\bar{u}$ and a sub-grid value, u'.

$$u = \bar{u} + u' \qquad (3.30)$$

The wall-adapting local eddy-viscosity (WALE) subgrid-scale model was implemented that is based on velocity gradient. This subgrid-scale model is capable of modeling flow near the walls and much faster than the dynamic Smagorinsky model [70,71]. Previous studies have demonstrated that LES is an efficient method to model turbulent and transitional flow within the airway [72–74].

3.3 Meshing

A CFD mesh separates the virtual airway segmented from an MR image into small cells. Each airway included prism layers on the wall and the rest was constructed using polyhedral cells. Bass et al. [75] showed that an airway with polyhedral cells required fewer number of cells and converged faster than airway with tetrahedral cells. The prism layers provide more accurate results near walls by capturing high velocity gradient in the direction normal to the wall and reduce misalignment of the flow with the mesh [76]. Airway surfaces have approximately 2 million cells and a temporal resolution of 0.8 ms which was based on the convergence study explained in section 3.4.1 Each inlet and outlet of the airway included extruded sections that extended the CFD mesh

beyond initial lengths. These extensions are 30 mm long and can avoid backflow due to unsteadiness of the flow.

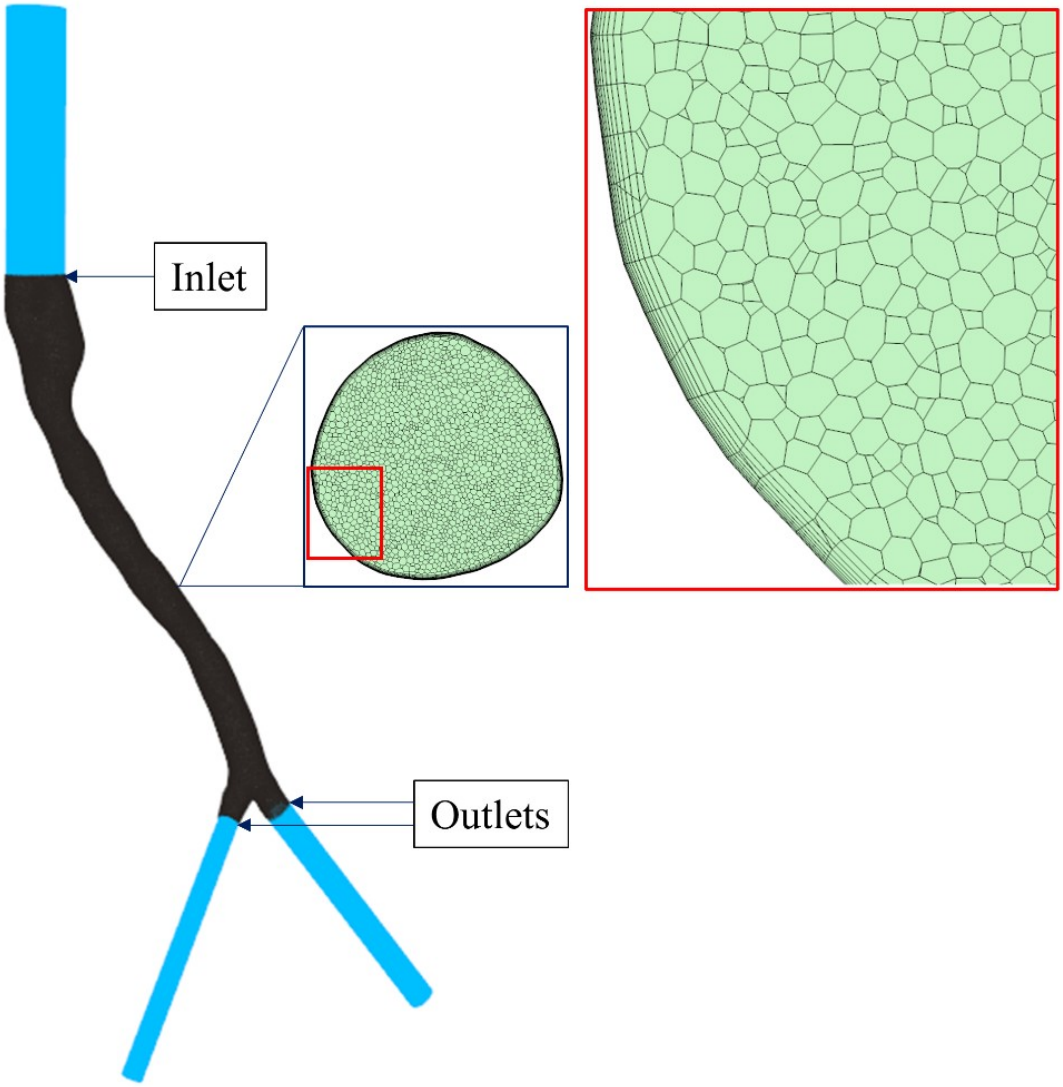

Figure 3.4: Discretized airway surface using prism layers and polyhedral cells. Extensions attached to the inlet and outlets are shown in blue.

3.4 Convergence

3.4.1 Mesh and Time Step Study

Mesh and time step convergence studies were performed before running patient-specific CFD simulations. The aim of the convergence study is to find spatial and temporal discretization parameters that produce mesh and time step independent results, that is the results depend only on the boundary conditions and not on the discretizations. The following Figure 3.5 shows the total pressure loss through the trachea (glottis to carina) at peak inspiration in a subject without TM at different mesh sizes and time steps. Each time step (0.08 ms, 0.8 ms, and 2 ms), five simulations were performed with five different mesh sizes (0.5 Million (M), 1 M, 2 M, 5 M, and 10 M). However, the time step of 0.01 ms only has three mesh sizes (0.5 M, 2 M, and 10 M) due to the run time of the CFD simulation is longer than other time steps. Based on the convergence study results, all patient-specific CFD simulations were performed with a mesh size of 2 M cells and a temporal resolution of 0.8 ms.

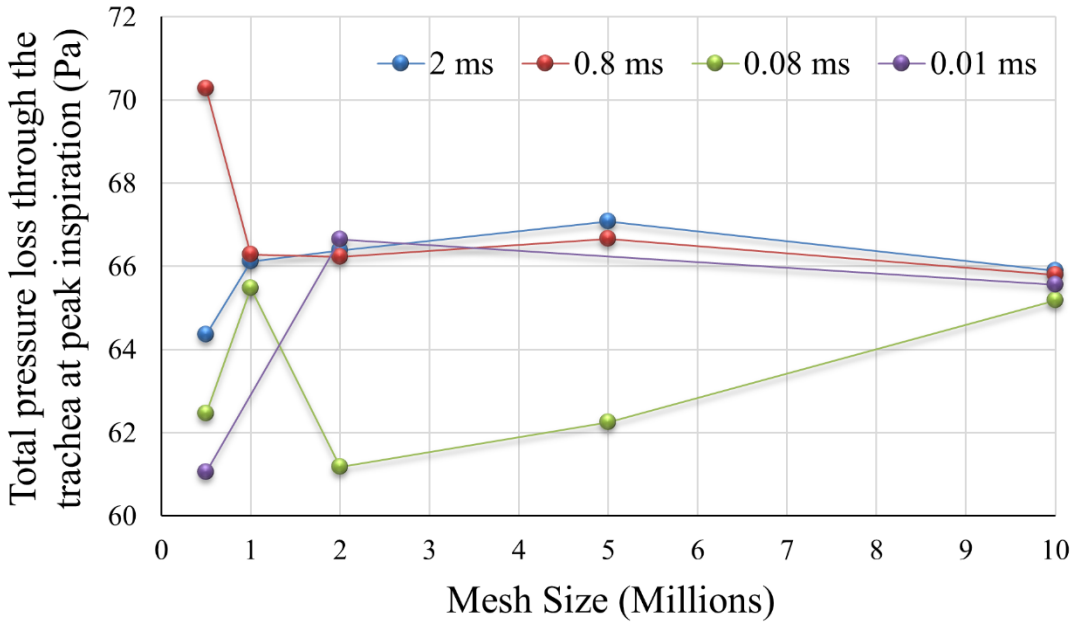

Figure 3.5: Total pressure loss through the trachea at peak inspiration at different mesh sizes (0.5 million (M), 1 M, 2 M, 5 M, and 10 M) and time steps (0.01 ms, 0.08 ms, 0.8 ms, and 2 ms).

Table 3.1 shows the errors between different mesh sizes at a temporal resolution of 0.8 ms. The relative error of the 10 M mesh compared to the 2 M mesh was 0.65%. In terms of the CFD run time, 2M mesh size with 0.8 ms time step took approximately 250 core-hours to complete up to peak inspiration. In contrast, 10 M mesh size with 0.8 ms took about 1100 core-hours.

Table 3.1: Mesh convergence study results at the temporal resolution of 0.8 ms

Mesh size (millions)	0.5	1	2	5	10
Total pressure loss of the trachea at peak inspiration (Pa)	70.27	66.28	66.22	66.65	65.79
Relative error (%)	6.12	0.09	0	0.65	-0.65

The following table summarizes the relative errors in total pressure loss through the trachea at peak inspiration using 2 million cells with different time steps (Table 3.2). The relative error in the total pressure loss through the trachea at peak inspiration with the temporal resolution of 0.01 ms was 0.63% compared to 0.8 ms time step.

Table 3.2: Time step convergence study results with mesh size of 2 million cells

Time step (ms)	0.01	0.08	0.8	2
Total pressure loss of the trachea at peak inspiration (Pa)	66.64	61.18	66.22	66.39
Relative error (%)	0.63	-7.61	0	0.26

3.4.2 Kolmogorov Scales

The Kolmogorov length and time scales determine the smallest scales in a turbulent flow. The kinetic energy of the turbulence disperses into smaller and smaller eddies until it is converted into heat due to viscous forces. The Kolmogorov scales are dominated by the viscosity (ν) and the turbulent dissipation rate (ε).

The fluctuations in velocity occur due to turbulent eddies and average quantities are considered in fluid dynamics. To understand Kolmogorov scales, first look at temporal means and variances.

For a specific velocity u,

$$u(x, y, z, t) = \bar{u} + u'(x, y, z, t) \qquad (3.31)$$

where $\bar{u}$ and u' represent time average and fluctuating velocities, respectively.

Time average velocity can be defined as,

$$\bar{u} = \lim_{T\to\infty} \frac{1}{T} \int_{t}^{t+T} u(x,y,z,t)dt \qquad (3.32)$$

Where T represents the average time period of the sample.

The time-average velocity can be rewritten in discrete form, assuming equally spaced points with a number of samples (N),

$$\bar{u} = \frac{1}{N} \sum_{i=0}^{N} u_i(x,y,z,t) \qquad (3.33)$$

The fluctuating velocity can be defined as,

$$u'(x,y,z,t) = u(x,y,z,t) - \overline{u(x,y,z,t)} \qquad (3.34)$$

Variance of the fluctuating velocity can be expressed by,

$$Var(u') = \overline{u'(x,y,z,t)^2} \qquad (3.35)$$

Using *(3.33)*, *(3.34)* and *(3.35)*,

$$Var(u') = \overline{u(x,y,z,t)^2} - \left(\overline{u(x,y,z,t)}\right)^2$$

$$Var(u') = \frac{1}{N-1}\left[\sum_{i=1}^{N} u_i^2 - \frac{1}{N}\left(\sum_{i=1}^{N} u_i\right)^2\right] \qquad (3.36)$$

Using equation *(3.36)*, fluctuating velocity components in the turbulent dissipation rate can be calculated.

$$\varepsilon = \nu\left\{ 2\left(\overline{\left(\frac{\partial u}{\partial x}\right)^2} + \overline{\left(\frac{\partial v}{\partial y}\right)^2} + \overline{\left(\frac{\partial w}{\partial z}\right)^2}\right) + \overline{\left(\frac{\partial u}{\partial y}\right)^2} + \overline{\left(\frac{\partial v}{\partial x}\right)^2} + \overline{\left(\frac{\partial u}{\partial z}\right)^2} + \overline{\left(\frac{\partial w}{\partial x}\right)^2} + \overline{\left(\frac{\partial v}{\partial z}\right)^2} + \overline{\left(\frac{\partial w}{\partial y}\right)^2} + 2\left(\frac{\overline{\partial u \partial v}}{\partial y \partial x} + \frac{\overline{\partial u \partial w}}{\partial z \partial x} + \frac{\overline{\partial v \partial w}}{\partial z \partial y}\right)\right\} \qquad (3.37)$$

Where $u, v,$ and w denote the fluctuating components of velocity.

The Kolmogorov length scale, η is given by,

$$\eta = \left(\frac{\nu^3}{\varepsilon}\right)^{\frac{1}{4}} \tag{3.38}$$

The Kolmogorov time scale, τ_η is given by,

$$\tau_\eta = \left(\frac{\nu}{\varepsilon}\right)^{\frac{1}{2}} \tag{3.39}$$

Direct Numerical Simulation (DNS) resolves all flow features in the flow, including large and small eddies created due to disturbances. In order to compare our CFD simulation to DNS, the Kolmogorov scales were compared with the finest simulation (i.e. 10 M cells with 0.01 ms time step) and calculated the length ratio and time ratio at peak inspiration.

$$Length\ ratio = \frac{Mean\ of\ cubic\ root\ volume}{\eta} \tag{3.40}$$

$$Time\ ratio = \frac{Time\ step\ of\ the\ simulation}{\tau_\eta} \tag{3.41}$$

Since our simulation has a dynamic airway surface, mean value of cubic root volume was used.

Figure 3.6 shows the Kolmogorov length ratio in the airway (pharynx to main bronchi) at peak inspiration for the 10 M mesh and 0.01 ms time step simulation. The volume-averaged length ratio was 0.55 [53]. The length ratio was less than one in the majority of the airway, indicating that our

finest simulation captured the smallest eddies in the flow. However, in the lower part of the airway, the length ratio was above one and the maximum length ratio was 6.2.

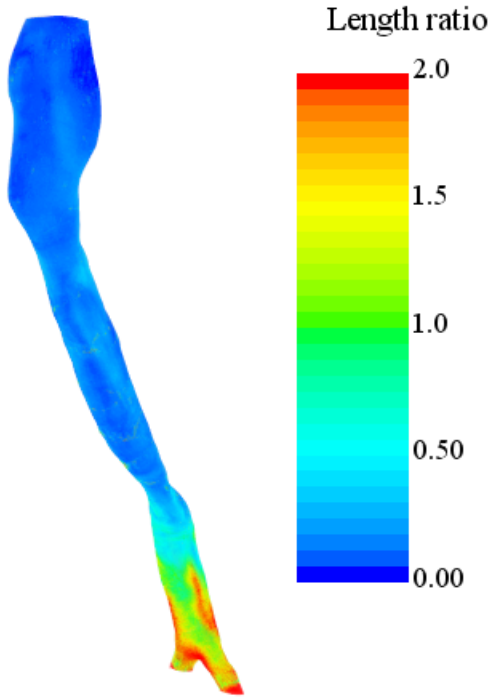

Figure 3.6: Length ratio distribution at peak inspiration in the cross-sectional area of the airway (pharynx to main bronchi)

Figure 3.7 shows the Kolmogorov time ratio for the finest simulation at peak inspiration. The volume-averaged time ratio was 0.025 and the time ratio was less than one throughout the airway [53]. These time ratio values indicate that 0.01 ms time step simulation captured all flow features in the flow.

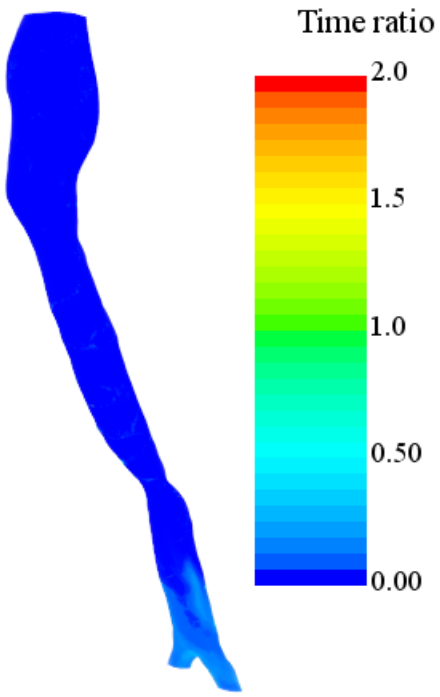

Figure 3.7: Time ratio distribution at peak inspiration in the cross-sectional area of the airway (pharynx to main bronchi)

3.5 Outputs of CFD

3.5.1 Energy Flux

CFD simulations provide airflow parameters such as work of breathing (WOB), pressure loss, and resistance through the airway that cannot be derived clinically. The instantaneous energy flux through a plane was calculated to obtain the WOB.

The instantaneous energy flux, $\emptyset_E$ can be calculated for a cross-sectional plane (A) using the following equation.

$$\emptyset_E = \oint_A P_T(\mathbf{U} \cdot \hat{\mathbf{n}}_\mathbf{A})\, dA \qquad (3.42)$$

where P_T is the total pressure on the plane, $\mathbf{U}$ is the velocity vector, and $\hat{\mathbf{n}}_\mathbf{A}$ is the unit vector perpendicular to the plane.

The energy loss (ΔE) between two cross-sectional planes of the airway over a breathing cycle (T) can be calculated,

$$\Delta E = \int_0^T \left(\emptyset_{E,1} - \emptyset_{E,2}\right) dt \qquad (3.43)$$

where $\emptyset_{E,1}$ and $\emptyset_{E,2}$ represent the instantaneous energy flux through plane 1 and 2, respectively. The difference between $\emptyset_{E,1}$ and $\emptyset_{E,2}$ is called the power loss between planes 1 and 2.

The energy loss (ΔE) represents the breathing effort (i.e. resistive WOB) required to overcome frictional losses due to airflow between 2 points in the airway during a single breath. The daily WOB can be computed by multiplying ΔE by the number of breaths per day. Figure 3.8 shows the instantaneous power loss of the trachea (glottis to carina) changes during the breathing cycle. The daily WOB of this subject was 108 J.

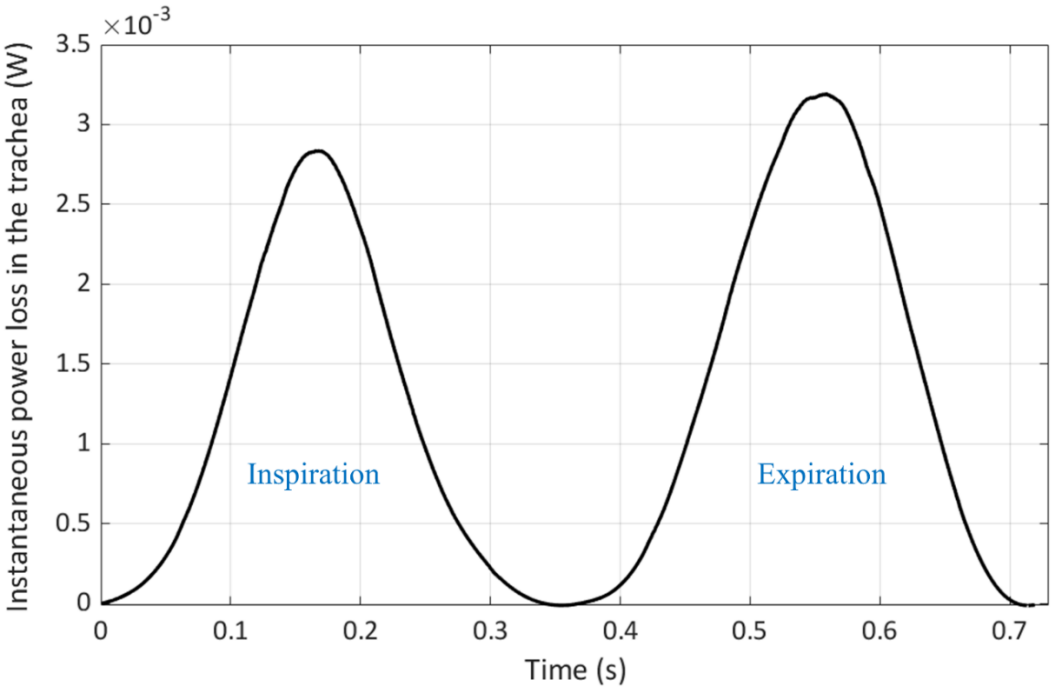

Figure 3.8: The instantaneous power loss of the trachea (glottis to carina) during the breathing cycle

3.5.2 Resistance

The instantaneous airway resistance, R is given by,

$$R = \frac{\Delta P}{Q} \tag{3.44}$$

where ΔP is the total pressure loss between 2 points in the airway and Q is the volumetric flow rate.

Cumulative airway resistance per breath, R_T can be calculated,

$$R_T = \int_0^T R dt \tag{3.45}$$

3.5.3 Reynolds Number

In fluid dynamics, the behavior of the fluid flow is determined based on the Reynolds number (Re) which is a dimensionless quantity.

$$Re = \frac{\rho \mathbf{U_{avg}} D}{\mu} \tag{3.46}$$

where ρ is the density of the fluid, $\mathbf{U_{avg}}$ is the average velocity through a cross-sectional plane of the airway, D is the hydraulic diameter, and μ denotes the fluid viscosity.

D can be calculated for an arbitrary shape cross-sectional plane such as a cross-section through the airway using the following equation.

$$D = 4 \frac{area\ of\ the\ plane}{perimeter\ of\ the\ plane} \tag{3.47}$$

Flow is considered laminar if Re is less than 2400. Flow is considered transitional if Re is between 2400 and 4000. Flow is considered turbulent if Re is over 4000 [65].

The cross-sectional area of the airway and the airflow rate have a direct impact on Re. Figure 3.9 shows the Re along the airway at peak expiration. This graph indicates that Re is fluctuating in a bigger range and it is over 2300 in some locations indicating the flow is transitional.

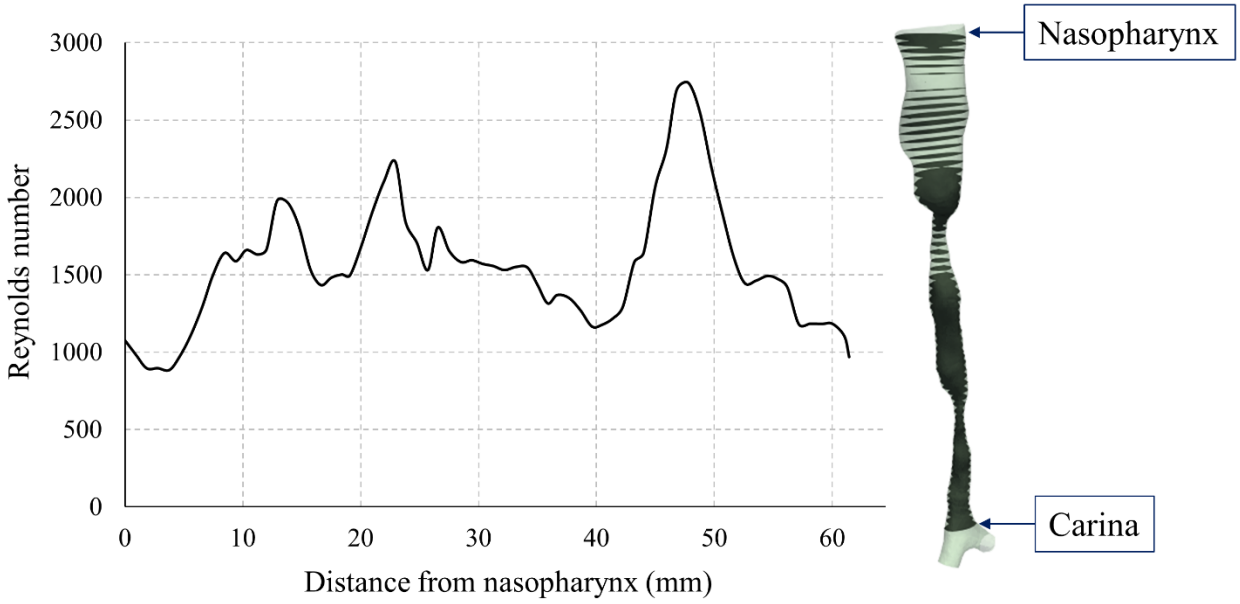

Figure 3.9: Reynolds number along the airway at peak expiration

4 Generating Boundary Conditions to Run CFD

There are mainly two boundary conditions applied to perform CFD simulations. The first boundary condition is the airway motion and the second boundary condition is the airflow rates in the airway. This chapter explains the step-by-step process of deriving these boundary conditions.

4.1 Airway Motion

4.1.1 Airway Segmentation

For each subject, there are four MR images that represent different phases of breathing (i.e. end expiration, peak inspiration, end inspiration, and peak expiration). Image reconstruction is explained in Section 2.4. ITK-SNAP (version 3.8.0) software developed by Penn Image Computing and Science Laboratory, USA was used to derive airway surfaces from MR images [77]. This software uses a 3-dimensional active contour segmentation technique. The initial intensity threshold of each MR image was obtained by calculating the average intensity between the air-filled airway and the tissue surrounding the airway [14,53,54]. Manual corrections may be needed after running the auto segmentation. Previous studies have demonstrated that to calculate accurate flow in the trachea, upstream anatomy extending to at least the glottis should be included [78,79]. Therefore, all our segmented airway surfaces extended from the main bronchi into the pharynx or nasopharynx.

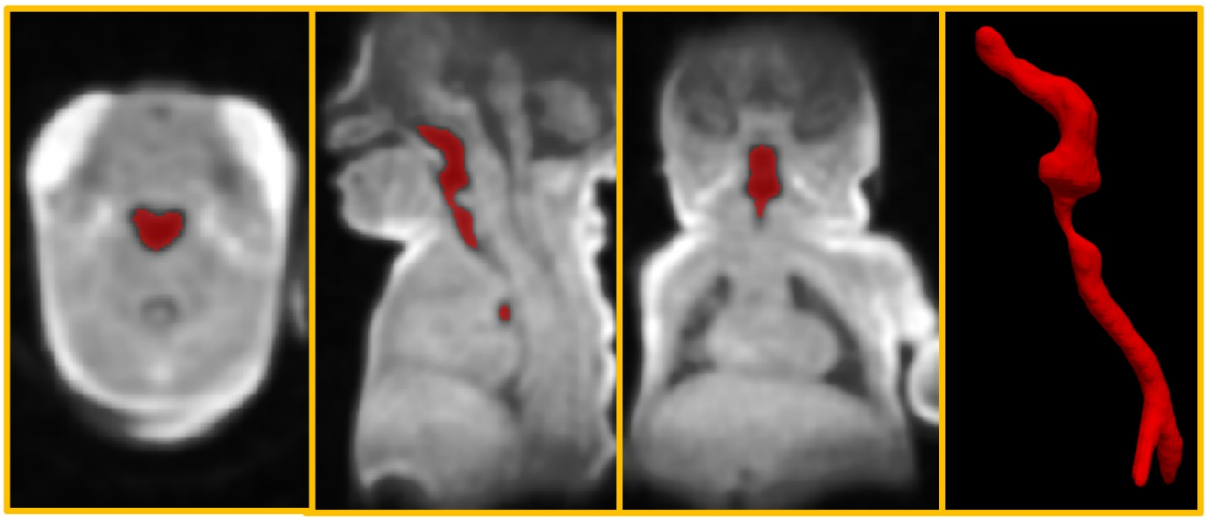

Figure 4.1: Segmentation of the airway from nasopharynx to main bronchi. Planes from left; axial, sagittal, coronal, and 3D rendered surface

4.1.2 Airway Surfaces Registration

A triangulated three-dimensional airway surface was created for each segmentation using as described in Section 4.1.1. All airway surfaces were smoothed to avoid volume shrinkage before starting the registration process. Taubin smoothing filter (smoothing parameters; $\lambda = 0.6$, $\mu = -0.6$) in the MeshLab 2016 (Visual Computing Lab, Italy) software was used to smooth airways [80,81].

Medical Image Registration ToolKit (MIRTK, developed by the Department of Computing, Imperial College London, UK, https://mirtk.github.io/) version 1.1 was used to register smoothed airway surfaces by using joined deformable motion tracking method. This technique allows obtaining the position of the airway at any time point between the main airway surfaces. Four-dimensional free-form deformation modeling technique was implemented to model the airway motion [82–85]. This technique is explained below.

All segmented airway surfaces were mapped to the initial airway surface by using the following parametric spline function [84,86–88].

$$\emptyset(\boldsymbol{x}, t: \boldsymbol{c}) = \boldsymbol{x} + \sum_{l=1}^{m} \beta\left(\frac{x - x_l}{\Delta x}\right) \beta\left(\frac{y - y_l}{\Delta y}\right) \beta\left(\frac{z - z_l}{\Delta z}\right) \beta\left(\frac{t - t_l}{\Delta t}\right) \boldsymbol{c_l} \tag{4.1}$$

where $\emptyset(\boldsymbol{x}, t)$ is the position of the airway at time t, $\boldsymbol{x} = (x, y, z)$ represents the spatial position of the first airway surface, $\beta(\cdot)$ represents the cubic B-spline function, m denotes the number of nodes in the airway surface, and $\boldsymbol{c_l}$ denotes the spline coefficient. Since all MR images were isotropic and 0.7 mm in resolution, control point spaces, Δx, Δy, and Δz were chosen as 1.4 mm (a multiple of voxel size). Several registrations were performed to obtain the smooth motion of the airway surface by changing the control point spacing. The time difference between the consecutive images of the breathing cycle is denoted by Δt.

In order to prevent excessive dynamic motion and to avoid folding, an objective function, $E(\boldsymbol{c})$ was introduced. Conjugate gradient descent minimization technique was applied to determine the parameters $\boldsymbol{c}$ in the airway motion model [86].

$$E(\boldsymbol{c}) = w_b b(\boldsymbol{c}) + w_s d_s(S_0, S_k; \boldsymbol{c}) \tag{4.2}$$

where $w_b = 0.001$ is a positive weight, $b(\mathbf{c})$ is the bending energy, $w_s = 1$ is a positive weight, d_s represents a distance measure related to airway surface, S_0 is a node in the initial mesh, S_k is the number of nodes in the S_k mesh.

$\mathrm{b}(\mathbf{c})$ is defined as,

$$b(\boldsymbol{c}) = \int_{\alpha} \sum_{i=1}^{4} \sum_{j=1}^{4} \left(\frac{\partial^2 \emptyset(\boldsymbol{p}, \boldsymbol{c})}{\partial p_i \partial p_j} \right)^2 \tag{4.3}$$

where α represents the four-dimensional domain of the airway surface and $\boldsymbol{p} = (\boldsymbol{x}, t)$ represents a point in the domain.

$\mathrm{d_s}(\mathrm{S_0}, \mathrm{S_k}; \mathbf{c})$ is defined as,

$$d_s(S_0, S_k; \boldsymbol{c}) = \frac{1}{|S_0|} \sum_{i=1}^{|S_0|} \sum_{j=1}^{|S_k|} A_k(\boldsymbol{c})[i, j] \left\| x_i - x_j \right\|_2 \tag{4.4}$$

where $\mathrm{A_k}(\mathbf{c})[\mathrm{i}, \mathrm{j}]$ is a weight that varies from 0-1 depending on the arrangement of the nodes in the mesh. The nearest neighbor approach was used to determine S_0 and S_k values. $\left\| \mathrm{x_i} - \mathrm{x_j} \right\|_2$ is the Euclidean distance between $\mathrm{i^{th}}$ and $\mathrm{j^{th}}$ node in the surface mesh [89–91].

Figure 4.2 compares the cross-sectional area between the segmented airway and the registered airway at end expiration time point. Cross-sectional areas in both airways were equal along the airway. The volume difference between the registered and segmented airways was 0.00001% compared to the segmented airway.

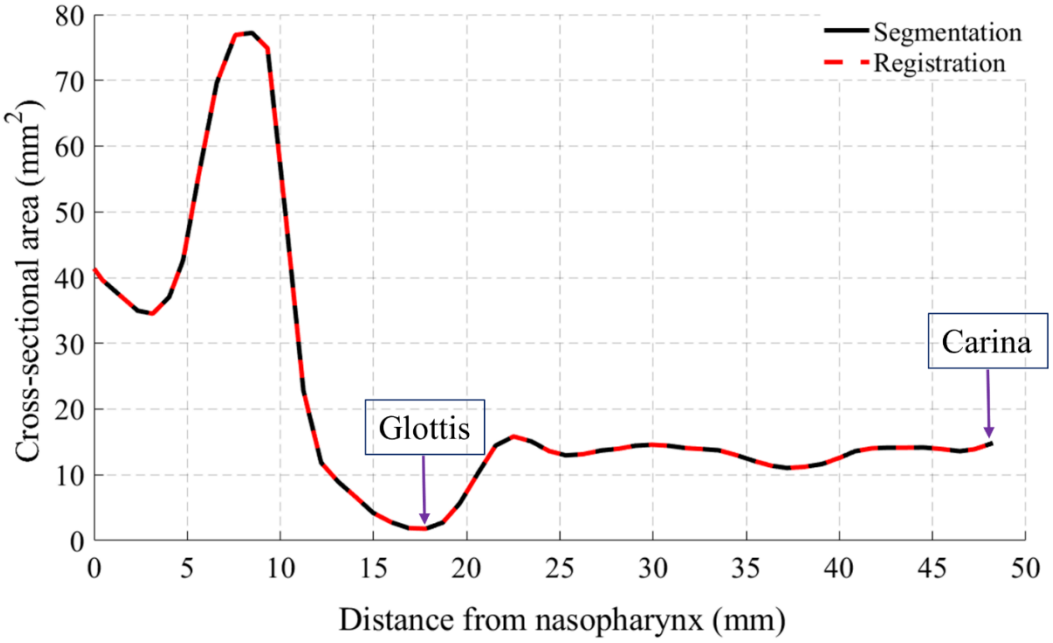

Figure 4.2: Cross-sectional area from the nasopharynx to carina in the segmented airway (solid line: black) and registered airway (dashed line: red) at end expiration time point.

4.1.3 Implementation of Airway Motion in STAR-CCM +

After airway surfaces registration, the position of each surface node in the airway can be determined at any instant during the breathing cycle. The temporal resolution of the airway motion was 0.8 ms, which was found from the time-step independence study (section 3.4.1). A table containing the position (x, y, z) of each surface node at each time interval throughout the breathing cycle was imported to CFD software, STAR-CCM+ (Siemens PLM Software, Plano, TX). The inbuilt morphing motion was used to move the nodes of the initial surface based on the control points table. BSpline morphing method was applied to interpolate the displacement of the surface vertices. The following figure shows the moving vertices on the initial CFD mesh.

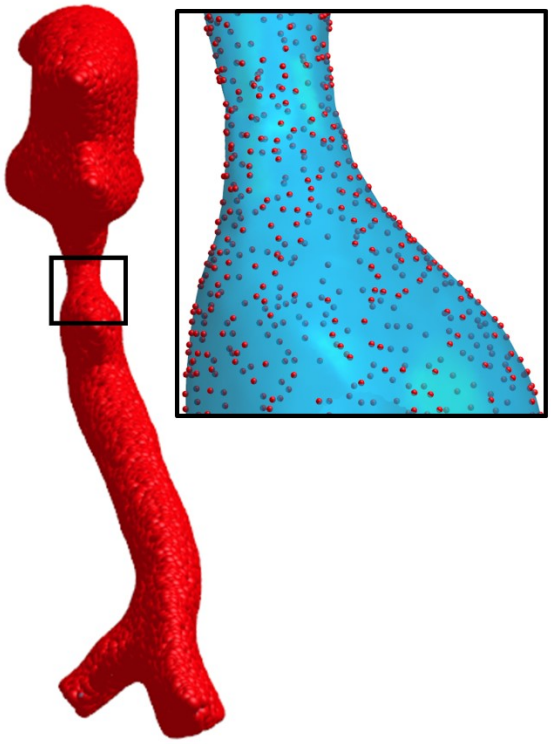

Figure 4.3: Moving nodes of the initial airway surface are shown in red (zoomed window). The position of each node changes every 0.8 ms during the breathing cycle.

4.2 Airflow Rates

4.2.1 Lung Segmentation

The lung tidal volume of each subject is needed to derive the airflow rates. The lungs in the end inspiration and end expiration MR images were segmented using the ITK-SNAP software with the auto-segmentation technique described for airway segmentation in Section 4.1.1. Manual corrections were made as needed. The lung volume difference between the two MR images was taken as the lung tidal volume.

4.2.2 Median Respiratory Waveform

Neonates may take about 1000 breaths during the 16-minute MRI scan. In order to find a typical respiratory waveform, a median waveform was obtained from the FID signal data for each subject. Figure 4.4 represents 10 breaths taken during the time of MRI.

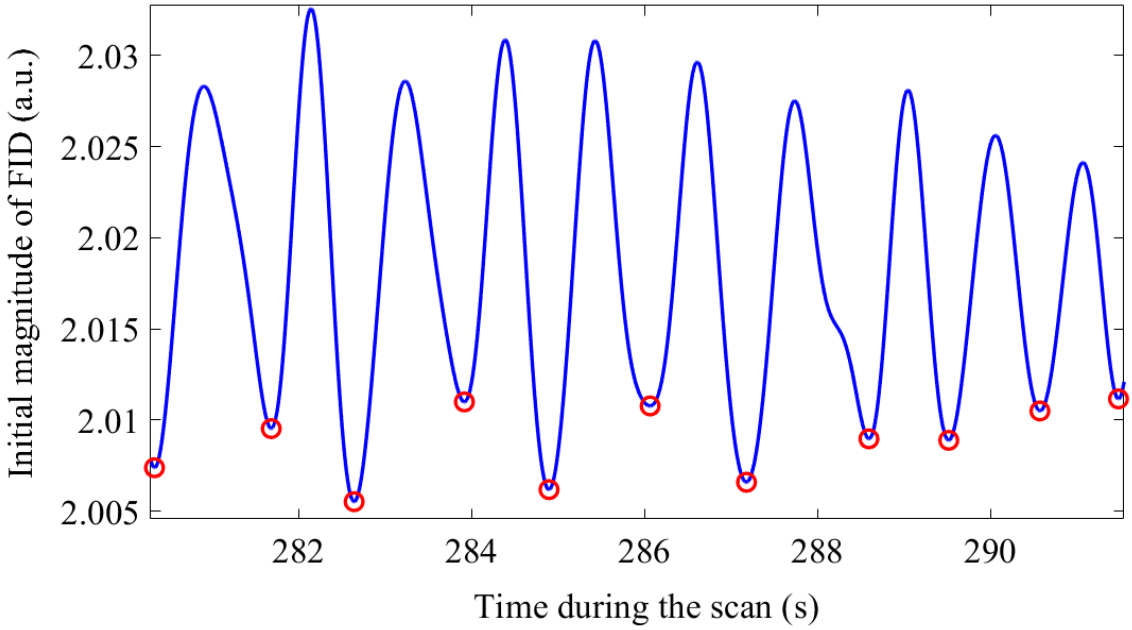

Figure 4.4: Initial magnitude of FID waveform, which represents 10 breaths. Red circles denote the end expiration time point. (a.u. = arbitrary units)

To obtain the median waveform, the total waveform was divided into respiratory waveforms representing a single breath. From these approximately 1000 breaths, groups of three waveforms were compared to each other. All three waveforms were stretched to the same length in time. Each waveform was assigned a score based on how many data points occurred with values in between the other two waveforms. This step was repeated until all breathing waveforms were compared with each other. Since the waveform with the highest score may not reflect a normal

breathing cycle, it cannot be considered the median waveform. The following criteria were followed to find the best representative waveform.

1) The difference between the inspiration and expiration volume has to be approximately zero (volume difference error was less than 1% compared to total tidal volume).

2) Expiration volume cannot exceed the inspiration volume.

3) The median wave should be selected within the 20% of the highest scored waves (score variations between the highest scored wave and 20% of the highest scored waves were small).

After obtaining the median waveform, the amplitude was rescaled based on the total lung tidal volume. The median breath duration of all breaths was used as the breathing time of the median waveform. Since the tidal volume of each lung is known, the same median waveform was rescaled according to each lung tidal volume.

Figure 4.5 shows the right and left lung volume change over a breath derived using the median waveform.

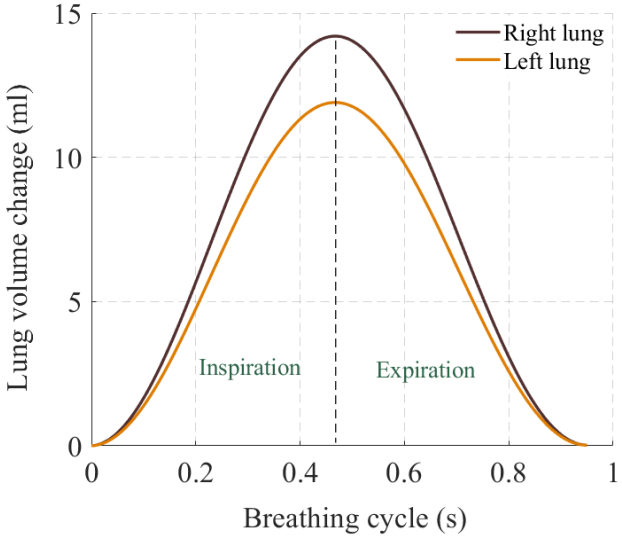

Figure 4.5: Lung volume change of the right and left lungs during the breathing cycle. The dashed line represents the end inspiration time point.

4.2.3 Derivation of Main Bronchi Airflow Rates

Right and left bronchus were used as inlets in the CFD simulation. The right and left lung volume curves were differentiated with respect to time to obtain the airflow rates (Figure 4.6).

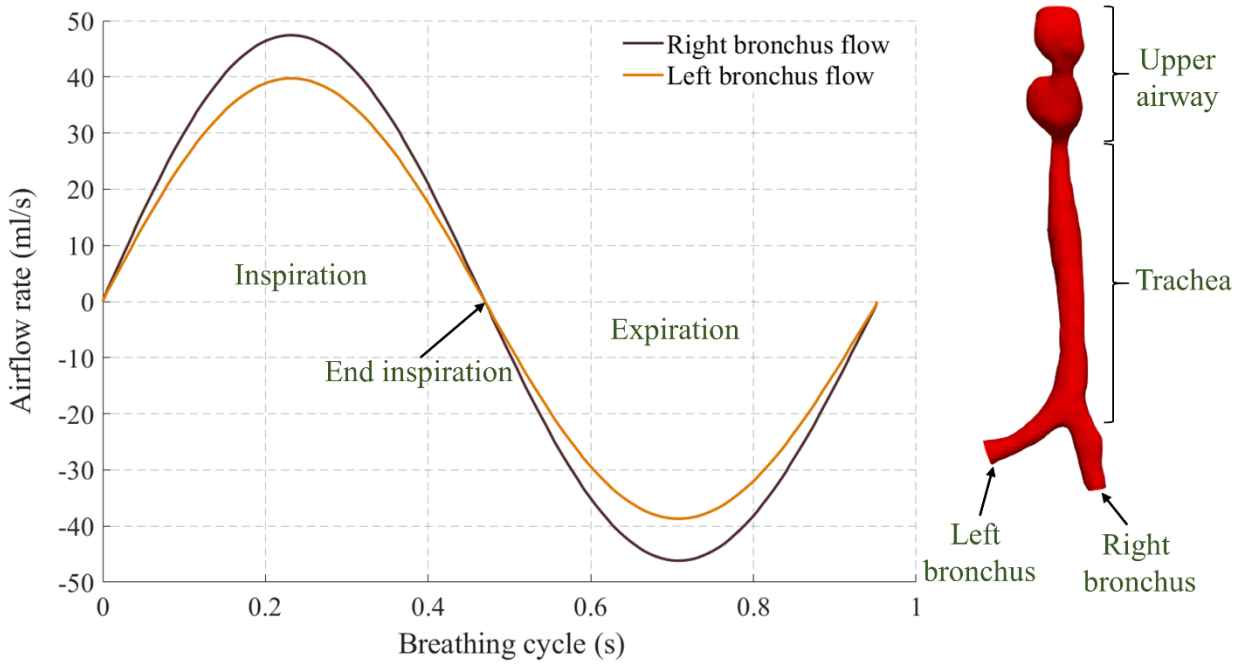

Figure 4.6: Airflow rates of the left and right bronchus

The airflow rates were converted to mass flow rates for use in the CFD simulation. The following air density values were applied for the conversion depending on the respiratory support used at the time of MRI by each subject (Table 4.1). All air density values were calculated assuming the air density was at 37 °C and incompressible during the breathing cycle [92–94].

Table 4.1: Air density values based on respiratory support

Respiratory support	Humidity (%)	Air density (kgm^{-3})
Room air	50	1.1248
HFNC/ CPAP, dry gas	0	1.1381
HFNC/ CPAP, heated gas	100	1.1114

In addition to airflow rates of the main bronchi, the initial pressure at the top of the airway was assumed to be atmospheric pressure. The airflow velocity at the airway wall was assumed to be zero relative to the airway wall (no-slip condition).

4.3 Summary

The airway motion and the airflow rates were derived for each subject to perform dynamic CFD simulations. A commercial CFD package, STAR-CCM+ versions 11.06.011-R8 and 14.04.011-R8 were used to perform CFD simulations in this study. These patient-specific simulations with unsteady boundary conditions took approximately 720 core-hours to complete. Chapters 5, 6, and 7 explain how these CFD simulations can be used to obtain clinically relevant information to improve patient care and well-being.

5 Differences in Respiratory Airflow Parameters due to Breathing Phase in Imaging

Researchers have limited access to dynamic MRI and only a few research groups use gating methods to reconstruct images. In Chapter 2.4 we learned that UTE MR images can be gated based on breathing to reconstruct an image that corresponds to each breathing phase. This chapter will detail the differences in respiratory airflow parameters in the trachea derived via CFD simulations using various airway images. All results were published in the journal of Computers in Biology and Medicine [53].

5.1 Introduction

Respiratory airflow measurements such as WOB, airway resistance, and pressure loss of the airway cannot be derived clinically but can be obtained by performing CFD simulations. Previous studies have demonstrated that these respiratory airflow measurements can be used to improve the understanding between the airway anatomy and airflow of healthy and patients with airway disease [95–100]. Usually, the airway geometry used for CFD simulation is derived from medical imaging, MRI or CT [86,96–98,101–103]. These images are usually static and represent only a one-time point of the breathing cycle or an average image of the entire breathing cycle. Therefore, the airway geometry in the CFD simulation is also static too. However, airway anatomy changes size and shape during breathing [104].

CFD simulations without airway motion are often performed with a steady flow rate that corresponds to a specific time point of the breathing cycle [105]. However, the airway anatomy derived using MRI or CT may not represent the same phase of breathing compared to airflow rate

time point. For instance, some studies use a breath-hold at total lung capacity or end expiration to capture images [98,106,107]. However, several studies have not reported the image acquisition time point during the breathing cycle [102,108].

A few studies have demonstrated the differences in respiratory airflow measurements between static and dynamic airway models [109,110]. The pressure loss difference from mask inlet at the nose to carina between dynamic and static model was 14.6% during inspiration and 19.2% during expiration in a single study [110].

In this work, one CFD simulation was performed with prescribed realistic airway wall motion derived via UTE MRI and compared with five static CFD simulations for each subject. The airway geometries of the static simulations were derived using end expiration, peak inspiration, end inspiration, peak expiration, and ungated (an average image captured over several breaths) airway images. In order to compare the differences in respiratory airflow measurements between healthy and subjects with airway disease, CFD simulations were conducted in a total of 4 subjects.

5.2 Methods

In this study, UTE MR images were obtained in four non-intubated NICU subjects (two healthy, two with airway disease-TM) after receiving parental consent and the Institutional Review Board approval. UTE MRI parameters are explained in detail in Section 2.3 Three subjects were breathing room air and one subject was using a high flow nasal cannula at the time of the MRI. The healthy subjects used in this study did not have any respiratory issues and the diagnosis of TM of the other two subjects was confirmed using clinical bronchoscopy. The mean postmenstrual age of four subjects was 41.6 ± 1.8 weeks at the time of the scan.

MR data of each subject were gated according to breathing and reconstructed into four images representing different breathing phases (end expiration, peak inspiration, end inspiration, and peak expiration). More details on image reconstruction can be found in Chapter 2.4. An ungated image was also reconstructed using all MR data. For each subject, five airway surfaces were segmented using the ungated and four gated images. All segmented airway surfaces represent the nasopharynx through the main bronchi. After smoothing airway surfaces, the airway motion of each subject was obtained by registering end expiration, peak inspiration, end inspiration, and peak expiration surfaces (Chapter 4.1). Airflow rates were obtained for each subject using the FID waveform and lung tidal volumes as described in Chapter 4.2.

For each subject, five static (no airway motion) and one dynamic (with airway motion) CFD simulations were performed (STAR-CCM+ 14.04.011-R8). Static simulations included an ungated airway geometry and four airways representing the main time points during the breath. Each CFD mesh had 2 million cells and a temporal resolution of 0.8 ms. More details about the CFD simulations can be found in Chapter 3. The daily resistive WOB of the trachea (glottis to carina), cumulative airway resistance per breath, and pressure loss through the trachea at peak expiration were calculated for each subject to compare cases. Reynolds number along the airway also evaluated at peak inspiration and peak expiration airflow rates.

5.3 Results

5.3.1 Analysis of the Airway Cross-sectional Areas and Airflow Rates

The airway motion during the breathing cycle changes the size and shape of the airway at each time point. The following figure demonstrates the cross-sectional area along the airway of the four subjects in five static airways and in the dynamic airway.

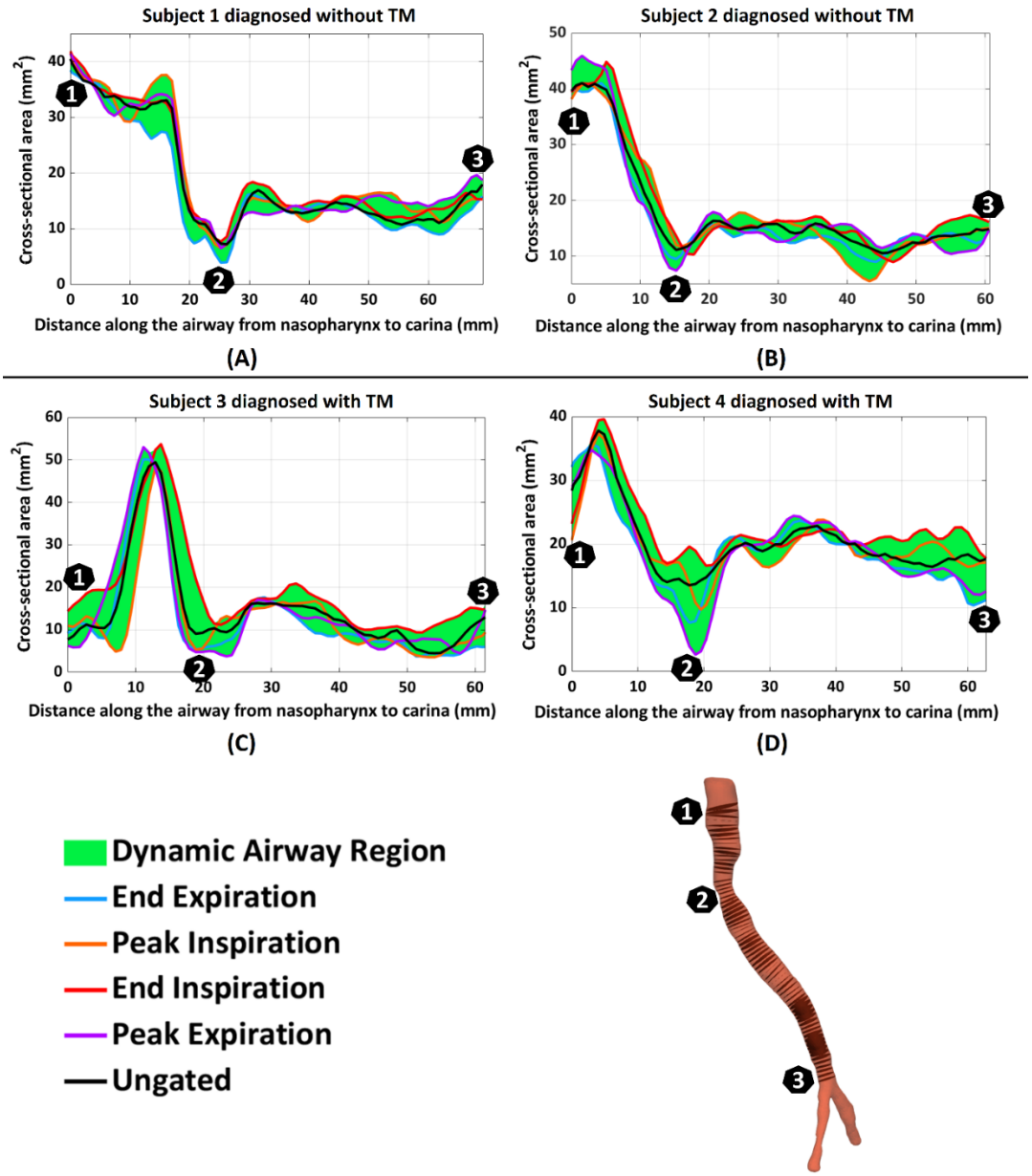

Figure 5.1: The cross-sectional area along the airway from the nasopharynx to carina of the subject 1 (A), subject 2 (B) without airway disease, subject 3 (C), and subject 4 (D) with airway disease (TM). The ungated, end expiration, peak inspiration, end inspiration, and peak expiration airways are shown in black, blue, orange, red, and purple. The green-colored area demonstrates the airway motion of the airway. Reprinted with permission [53].

The mean variation in tracheal cross-sectional area from the end expiration time point to the time point of most differences in the subject 1, 2, 3, and 4 were 30%, 24%, 91%, and 27%, respectively. The maximum change in tracheal cross-sectional area in the healthy subjects (Subjects 1 and 2) was 68% and 223% in the subjects with TM (Subjects 3 and 4). In all subjects, the end inspiration airway was the largest in cross-sectional area in the majority of the airway than other time point airways and had the highest airway volume. Figure 5.1C shows that the cross-sectional area of the end inspiration airway after 50 mm from the nasopharynx was changed by more than 100% compared to the end expiration. The glottis cross-sectional area changed from 2.6 mm^2 to 16.6 mm^2 in subject 4 diagnosed with TM (Figure 5.1D). The cross-sectional area of the ungated airway was approximately in the middle of the dynamic region in all subjects.

Table 5.1 shows the lung tidal volumes, the ratio of the right to left lung tidal volumes, and the respiratory rates of all subjects. The lung tidal volume of each subject was derived by segmenting the end inspiration and end expiration MR images. The right lung tidal volume is approximately twice compared to the left lung tidal volume in subject 3 with TM [53].

Table 5.1: Respiratory data of the four subjects

Subject (Condition)	Lung tidal volume (ml)	The ratio of right: left lung tidal volumes	Respiratory rate (breaths/min)
Subject 1 (without TM)	7.95	57 : 43	79
Subject 2 (without TM)	14.8	48 : 52	83
Subject 3 (with TM)	23.1	65 : 35	54
Subject 4 (with TM)	13.0	55 : 45	68

5.3.2 Reynolds Number along the Airway

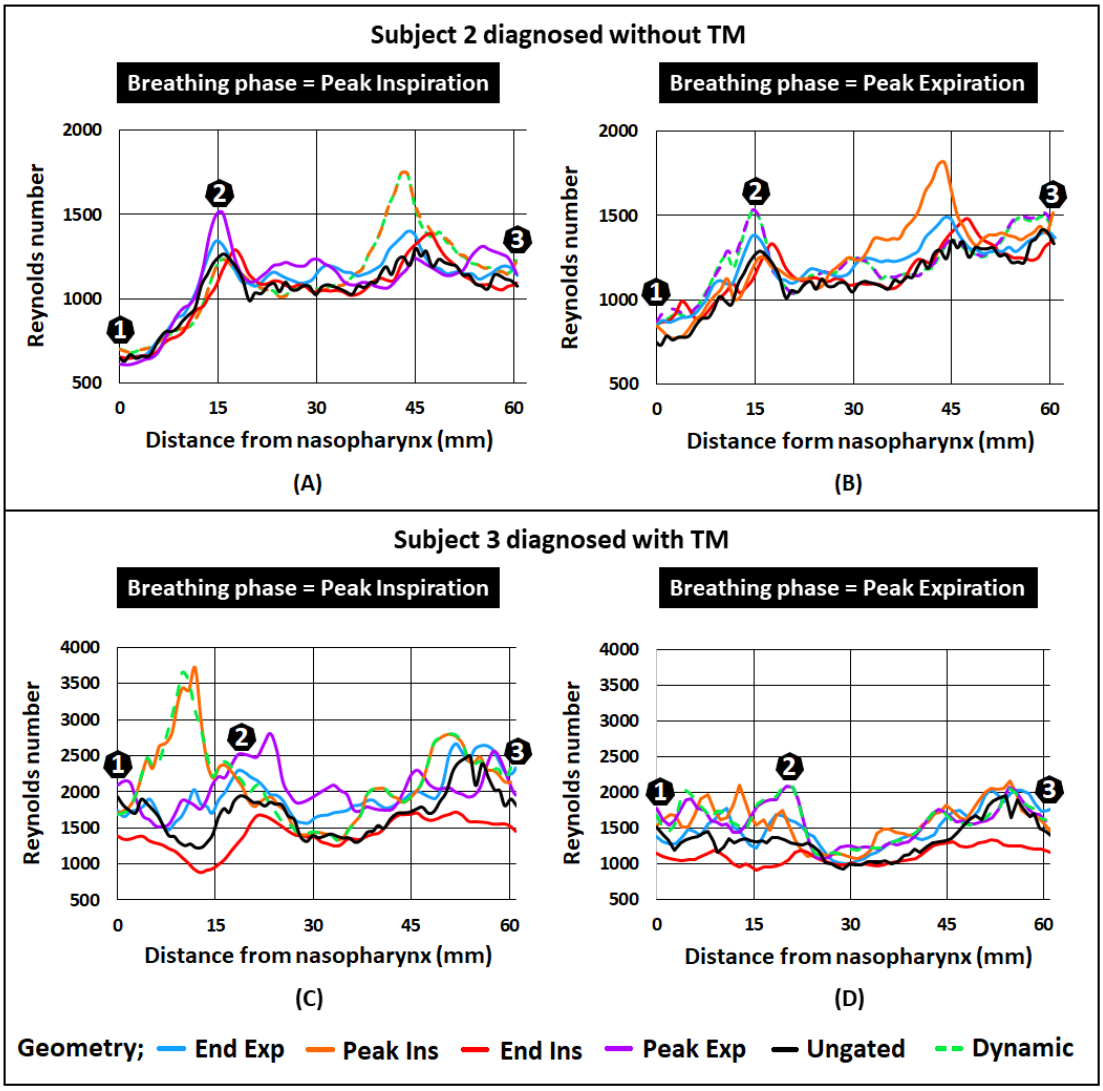

Figure 5.2: Reynolds number along the airway from the nasopharynx to carina for static cases (blue – end expiration, orange - peak inspiration, red – end inspiration, purple – peak expiration, black – ungated) and dynamic case (green). (A) and (B) demonstrate the Reynolds number along the airway in a subject without TM (Subject 2) at peak inspiration and peak expiration, respectively. (C) and (D) demonstrate the same data for the subject with TM (Subject 3). Numbers 1, 2, and 3 indicate the locations of the nasopharynx, glottis, and carina, respectively. Reprinted with permission [53].

The above plot shows the mean cross-sectional Reynolds number along the airway of a healthy subject (Subject 2) and a subject with TM (Subject 3) at peak inspiration and peak expiration. Figure 5.2A shows that the difference in the Reynolds numbers derived using different airway geometries was small at peak inspiration, except at 45 mm from the nasopharynx in subject 2. In contrast, the Reynolds number fluctuates throughout the airway in subject 3 at peak inspiration. The Reynolds number changed from approximately 1000 (end inspiration) to 3500 (dynamic) at about 12 mm from the nasopharynx when using different geometries. Similar behavior can be observed for each subject at peak expiration. The other two subjects (Subject 1 and 4) also showed similar variations in the Reynolds number along the airway compared to subjects 2 and 3, respectively.

5.3.3 The Effect of Airway Geometry on Respiratory Airflow Measurements

The daily tracheal resistive work of breathing (TR-WOB), cumulative airway resistance in the trachea over one breath, and the tracheal pressure loss at peak expiration were calculated for six CFD simulations in each subject to quantify the differences due to various airway geometries. All static airway CFD results were compared with the dynamic airway results of each subject. Figure 5.3 shows the daily TR-WOB of the four subjects using static/dynamic airways and the percentage differences in WOB of the static airways compared to the dynamic airway. The daily TR-WOB obtained using end expiration airway was 102% higher compared to that value obtained using the dynamic airway in subject 1 without TM. The daily TR-WOB obtained using end inspiration airway was 82% lower compared to that value obtained using the dynamic airway in subject 3 with TM. There was at least one static airway geometry that provides a TR-WOB at least 50% lower or higher than the dynamic airway in the other two subjects (Subjects 2 and 4). Figure

5.3B also shows that no single static airway, including the ungated airway can be used to reflect the dynamic airway of each subject.

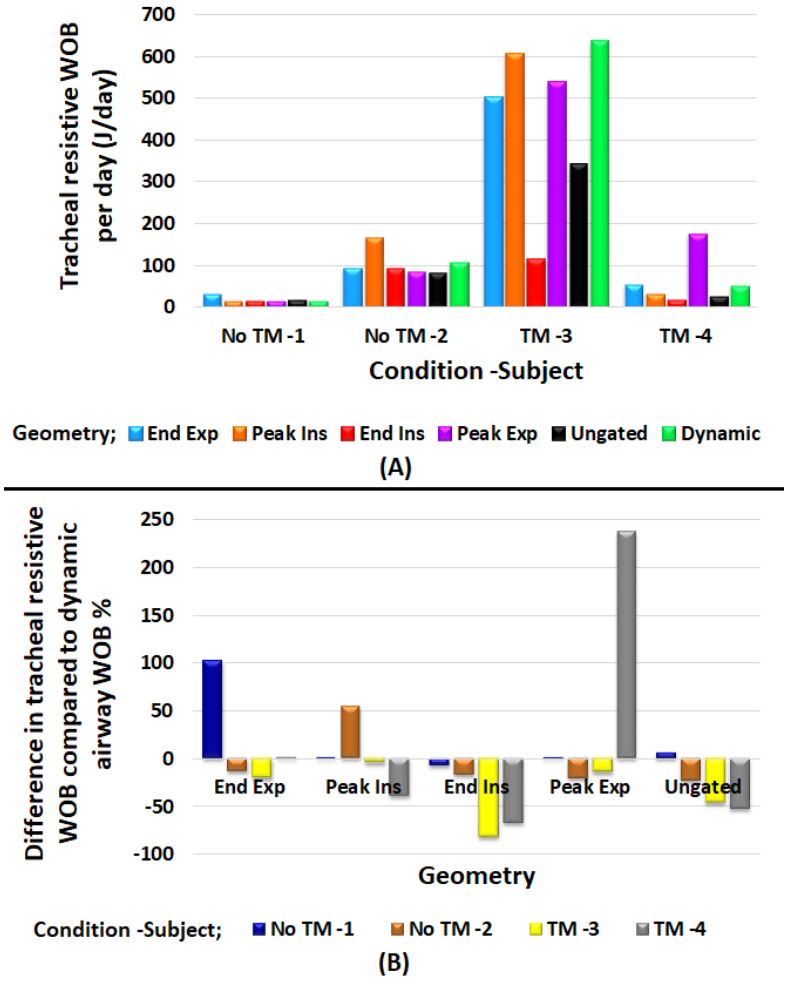

Figure 5.3: Tracheal resistive work of breathing of the four subjects calculated per day using static airways (blue – end expiration, orange - peak inspiration, red – end inspiration, purple – peak expiration, and black - ungated) and the dynamic airway (green) (A). The percentage differences in the tracheal resistive work of breathing of the static airways compared to the dynamic airway (blue - Subject 1, brown – Subject 2, yellow – Subject 3, and gray – Subject 4) (B). Reprinted with permission [53].

Similar variations can be observed for integrated airway resistance per breath compared to TR-WOB in all subjects. The integrated tracheal airway resistance derived using end expiration airway was 105% higher than that value of the dynamic airway in subject 1 without TM. In subject 4 with TM, the tracheal pressure drop was more than 38% lower in all static airways compared to the dynamic airway. Table 5.2 shows the full results of all respiratory airflow measurements [53].

Table 5.2: Respiratory airflow measurements in static airways compared to dynamic airway

Tracheal Resistive WOB						
J/Day (% Difference to Dynamic Geometry Case)						
Geometry	End Expiration	Peak Inspiration	End Inspiration	Peak Expiration	Ungated	Dynamic
Subject 1 (No TM)	30.79 (102%)	15.36 (1%)	14.22 (-7%)	15.55 (2%)	16.24 (6%)	15.27
Subject 2 (No TM)	93.43 (-13%)	165.85 (54%)	89.38 (-17%)	85.59 (-20%)	82.80 (-23%)	107.35
Subject 3 (TM)	499.75 (-21%)	605.35 (-5%)	112.76 (-82%)	537.07 (-15%)	341 (-46%)	635.45
Subject 4 (TM)	52.81 (2%)	31.66 (-39%)	17.07 (-67%)	174.82 (237%)	24.94(-52%)	51.90
Tracheal Airway Resistance Integrated w.r.t. Time Across One Breathing Cycle						
$Pa.s^2/ml$ (% Difference to Dynamic Geometry Case)						

Geometry	End Expiration	Peak Inspiration	End Inspiration	Peak Expiration	Ungated	Dynamic
Subject 1 (No TM)	0.41 (105%)	0.19 (-5%)	0.17 (-15%)	0.14 (-30%)	0.17 (-15%)	0.2
Subject 2 (No TM)	0.28 (-33%)	0.50 (19%)	0.27 (-36%)	0.28 (-33%)	0.21 (-50%)	0.42
Subject 3 (TM)	2.39 (-27%)	2.71 (-17%)	0.39 (-88%)	2.52 (-23%)	1.39 (-57%)	3.26
Subject 4 (TM)	0.17 (-48%)	0.08 (-76%)	0.04 (-88%)	0.99 (200%)	0.06 (-82%)	0.33
Pressure Loss Across Trachea at Peak Expiration Airflow						
cmH_2O (% Difference to Dynamic Geometry Case)						
Geometry	End Expiration	Peak Inspiration	End Inspiration	Peak Expiration	Ungated	Dynamic
Subject 1 (No TM)	-0.15 (88%)	-0.09 (13%)	-0.07 (-13%)	-0.07 (-13%)	-0.09 (13%)	-0.08
Subject 2 (No TM)	-0.31 (-3%)	-0.62 (94%)	-0.32 (0%)	-0.28 (-13%)	-0.26 (-19%)	-0.32
Subject 3 (TM)	-1.29 (-15%)	-1.30 (-15%)	-0.23 (-85%)	-1.28 (-16%)	-0.74 (-51%)	-1.52

Subject 4 (TM)	-0.14 (-71%)	-0.07 (-85%)	-0.05 (-90%)	-0.30 (-38%)	-0.06 (-88%)	-0.48

5.3.4 Airway Velocity Distribution

The following Figure 5.4 illustrates the airway velocity distribution of the 5 static airways and the dynamic airway of Subject 4 with TM at peak inspiration airflow. The airflow velocity in the dynamic airway was lower than the end expiration and peak expiration airways and higher than the end inspiration and the ungated airway. The end expiration and peak expiration static airways show a strong jet at the glottis, carina and the middle of the trachea. However, a much weaker jet can be seen in the end inspiration and ungated airways. The peak inspiration airway demonstrates a similar velocity distribution compared to the dynamic case except for the glottis area.

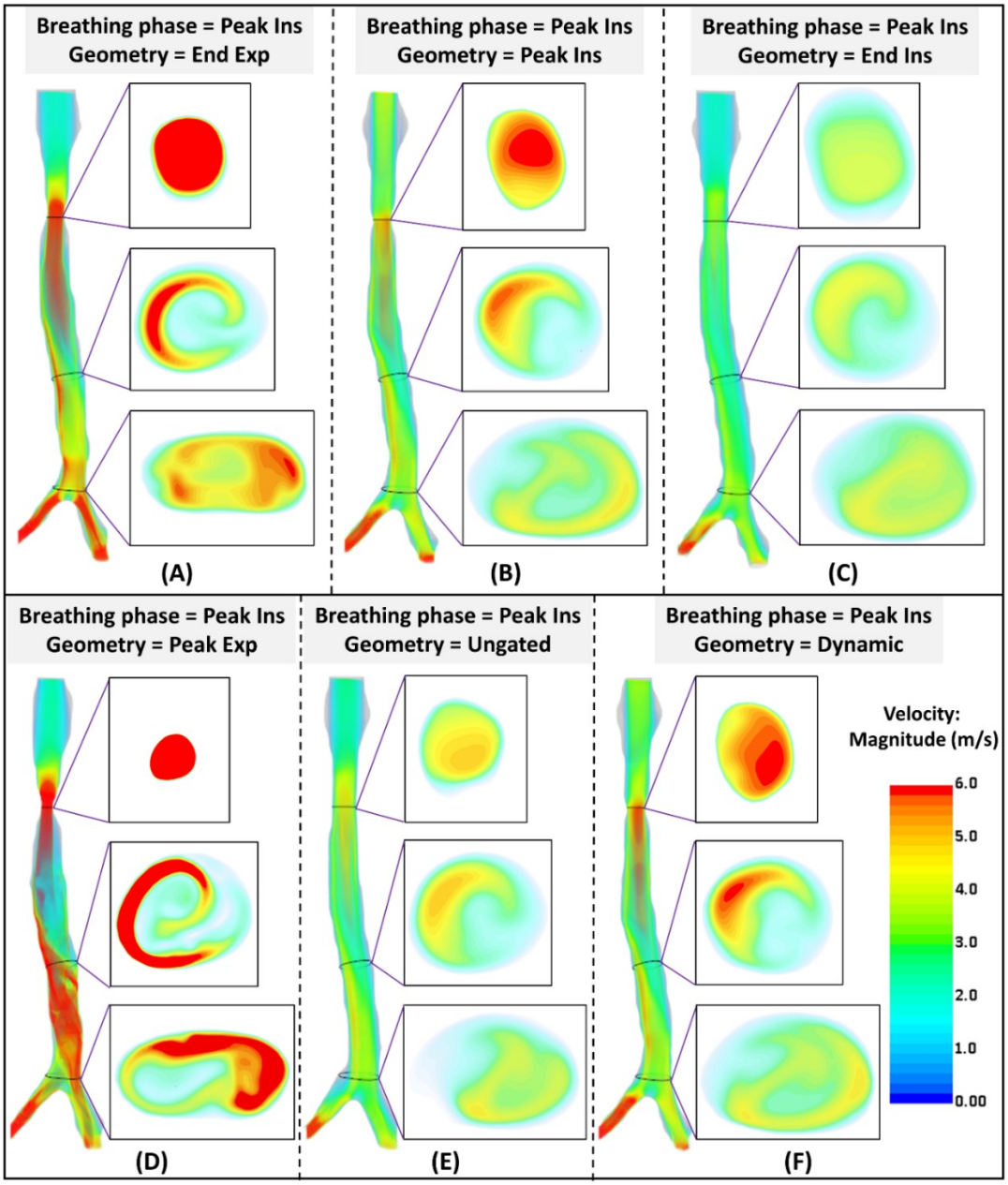

Figure 5.4: Velocity profiles of subject 4 with TM obtained using static airways (end expiration (A), peak inspiration (B), end inspiration (C), peak expiration (D), and ungated (E)) and the dynamic airway (F) at peak inspiration airflow. The three cross-sectional planes of each airway illustrate the velocity distribution of the glottis, middle of the trachea, and carina. Reprinted with permission [53].

5.4 Discussion and Conclusions

The cross-sectional areas of the airway geometries obtained at different phases of breathing in healthy and subjects with TM indicate that the variation in the cross-sectional area is not uniform among static airways (Figure 5.1). The Reynolds numbers derived along the airway using each static airway also demonstrate how flow characteristics can change depending on the airway geometry used for the CFD simulation. The airflow in Subject 3 diagnosed with TM was transitional as Reynolds numbers passed 2300 in some regions along the airway (Figure 5.2). These findings reflect how the phase of breathing of the imaging can affect CFD modeling.

The differences between airflow measurements in the dynamic and static simulations demonstrate the importance of using dynamic airway surfaces to perform CFD simulations (Figure 5.3). The airflow measurements calculated using the CFD simulation with the ungated image, which represents the average airway position over many breaths during the time of MRI were not closer to values obtained from the CFD simulation with the dynamic airway. Each static airway CFD simulation has its own flow characteristics, and future studies may need to report more details on image acquisition, such as in which phase of breathing the images are captured.

Dynamic airway CFD simulations take an extra 25% core-hours to run compared to static airway CFD simulations. However, these patient-specific CFD simulations with airway motion and dynamic flow conditions are capable of providing meaningful information that can help clinicians to improve patient care and well-being. Future studies need to consider using dynamic airway modeling instead of static airway modeling. Cine CT or dynamic MRI are a few examples that can provide dynamic airway images.

6 Neonatal Tracheal Resistive Work of Breathing

This chapter discusses the tracheal resistive work of breathing in newborns diagnosed with and without TM. All of the results have been previously published in the journal Annals of the American Thoracic Society [54].

6.1 Introduction

Neonates diagnosed with TM may require oxygen support due to dynamic collapse during breathing. Currently, there is no technique to quantify the increased breathing effort (WOB). Previous studies have calculated total WOB (elastic and resistive WOB) based on the Campbell diagram by using pleural pressure. In these studies, esophageal pressure was measured as a surrogate for pleural pressure [111–113].

The primary diagnostic method of TM is bronchoscopy. However, this technique is not capable of quantifying the degree of severity in TM. In recent studies of newborns, MRI has been used to evaluate TM, which overlaps well with bronchoscopy findings [13,14]. These evaluations are based on the airway dynamics and cannot calculate the effect on WOB. To determine the resistive WOB in the trachea due to airflow, CFD simulations were conducted with airway motion derived via MRI.

This study hypothesized that the resistive WOB component of the trachea (glottis to carina) (TR-WOB) in neonates diagnosed with TM is higher than the neonates diagnosed without TM due to airway motion. Two CFD simulations were performed with patient-specific boundary conditions (airflow rates and airway anatomy) for each subject to calculate the TR-WOB. The first CFD simulation uses a dynamic airway derived via UTE MRI. The airway geometry in the second CFD simulation is static and that geometry represents approximately the largest size detected

during the breathing cycle. In terms of WOB, the second CFD simulation estimates the lowest possible WOB of each subject, since holding the airway open at its largest size should reduce resistance to airflow. The difference between the WOB calculated from the static and dynamic cases represents the elevated TR-WOB due to each subject's airway motion, which was evaluated and compared with the diagnosis of TM.

6.2 Methods

This research study included 14 NICU subjects after Institutional Review Board approval and parental consent. All subjects were non-intubated and were using non-invasive respiratory support (including free-breathing) at the time of MRI. The diagnosis of TM was evaluated based on bronchoscopy and three of the fourteen subjects did not undergo bronchoscopy since they were considered as respiratory controls with no airway or lung defects.

UTE MRI scans were performed for each subject as described in Section 2.3. Four MR images were reconstructed based on breathing which represents different phases of breathing (Chapter 2.4). Each airway image was used to segment airway surfaces and these virtually created airways were registered to obtain airway motion as described in Chapter 4.1. Each airway surface was extended from main bronchi to pharynx. The airflow rates of the main bronchi were derived by using the lung tidal volumes and the median respiratory waveform (Chapter 4.2). The airway motion and the airflow rates were used as boundary conditions (inputs) to perform the first CFD simulation of each subject. The second CFD simulation was static (without airway motion) and used the same airflow rates applied in the first CFD simulation. All CFD simulations were performed using the STAR-CCM+ 11.06.011-R8 version. In most subjects, the end inspiration airway was the largest in volume and the cross-sectional areas were more prominent in most

locations along the airway compared to other airways obtained at different time points. The narrow regions in the end inspiration airway were replaced by using other segmented airways with larger cross-sectional areas. Figure 6.1 shows how the static airway was made using end inspiration and peak inspiration airways in an example subject.

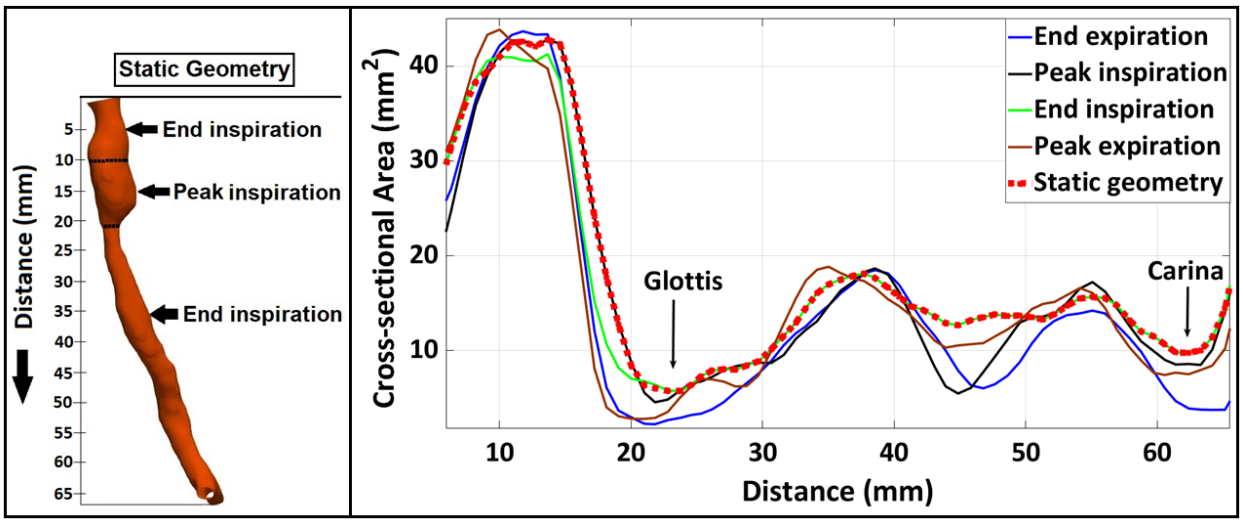

Figure 6.1: The cross-sectional area along the airway of the static geometry and the airway surfaces at different time points during the breathing cycle. Reprinted with permission of the American Thoracic Society. Copyright © 2021 American Thoracic Society. All rights reserved [54].

The daily TR-WOB from glottis to carina of the two simulations was calculated as described in Section 3.5.1. An unpaired t-test (two-tailed, unequal variance) was applied to calculate the p-values in subjects diagnosed with and without TM in both static and dynamic cases. A paired t-test (two-tailed, unequal variance) was applied to calculate p-values between static and dynamic airways. A p-value less than 0.05 was assumed statistically significant.

6.3 Results

6.3.1 Subject Demographics

The PMA of the study subjects was 41.0 ± 1.5 weeks at the time of MRI. On average, the weight and height of the neonates were 3.5 ± 0.8 kg and 49 ± 4 cm, respectively. Table 6.1 shows the sex, clinical diagnosis, post-menstrual age, weight, and respiratory support at the time of MRI of all subjects [54].

Table 6.1: Patient information

Study group	Subject	Sex	Clinical diagnosis	PMA at MRI (weeks)	Weight at MRI (kg)	Respiratory support at MRI
No TM	01	M	BEF	40	3.7	Room air
	02	F	Respiratory control	40.9	3.61	Room air
	03	M	Respiratory control	40.3	3.9	Room air
	04	F	Respiratory control	39.4	2.85	Room air
	05	M	BPD	43	3.6	HFNC
	06	M	BPD	38.7	3.07	HFNC
	07	F	TEF/EA	40	3.18	Room air

TM	08	F	TEF/EA	40.1	2.7	Room air
	09	F	BPD	43.1	4.13	Room air
	10	M	BPD	43.1	5.35	Room air
	11	F	TEF/EA	41.3	2.91	HFNC
	12	F	BPD	43	3.35	HFNC
	13	M	BPD	41	1.94	RAM CPAP
	14	M	BPD	39.6	4.2	RAM CPAP

6.3.2 Increase in TR-WOB in a Subject with and without TM

The following Figure 6.2 illustrates the differences in instantaneous TR-WOB per second for a subject without TM (A) and a subject with TM (B) during the breathing cycle obtained via CFD simulations. The difference between the moving (red) and static (blue) airway curves represents the increase in TR-WOB during the breath of each subject. In the subject with TM, increase TR-WOB is higher compared to subject without TM. Furthermore, increase in TR-WOB is higher during expiration than inspiration in the subject with TM. In the subject without TM, the increase in TR-WOB due to airway motion was 36% (daily TR-WOB in moving airway 84.9 J, daily TR-WOB in static airway 62.2 J). In contrast, the increase in TR-WOB of the subject with TM was 848% (daily TR-WOB in moving airway 421.7 J, daily TR-WOB in static airway 44.5 J).

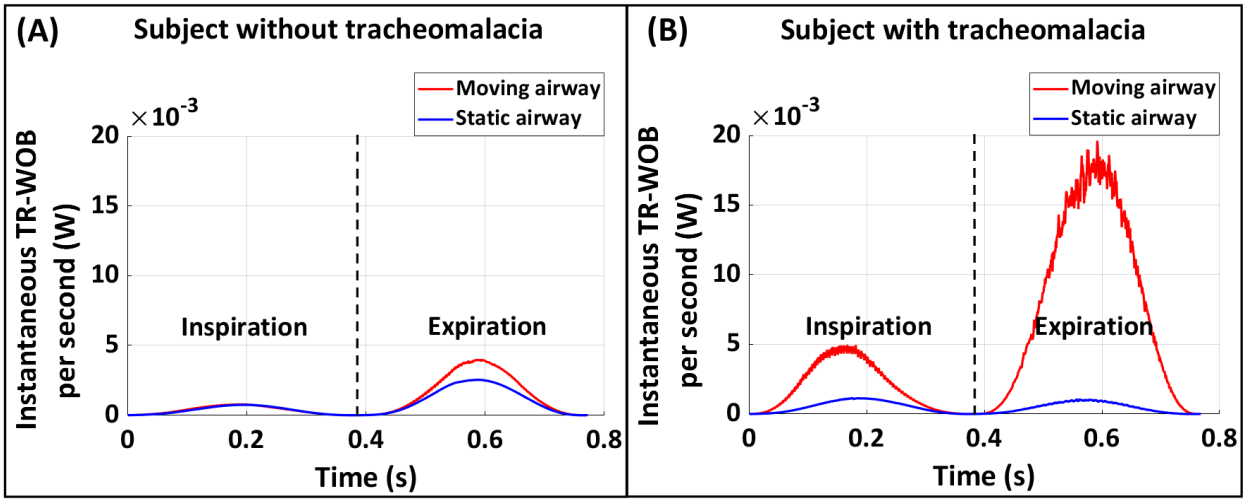

Figure 6.2: The instantaneous TR-WOB per second for a subject without TM (A) and with TM (B). Red and blue lines in both panels show the TR-WOB in the moving and static airways, respectively. The end inspiration time point is denoted by black dashed lines. Reprinted with permission of the American Thoracic Society. Copyright © 2021 American Thoracic Society. All rights reserved [54].

6.3.3 Velocity Distribution at Peak Expiration

In most subjects diagnosed with TM, increase in TR-WOB is greater during expiration compared to inspiration. Figure 6.3 shows the airflow velocity distribution in a subject diagnosed with TM at peak expiration in a dynamic airway (A) and a static airway (B). There is a narrow region in the middle of the trachea (marked ▲) in the dynamic airway. As a result, a strong jet increases TR-WOB in the dynamic case compared to the static case. In contrast, a much weaker jet can be seen in the static airway.

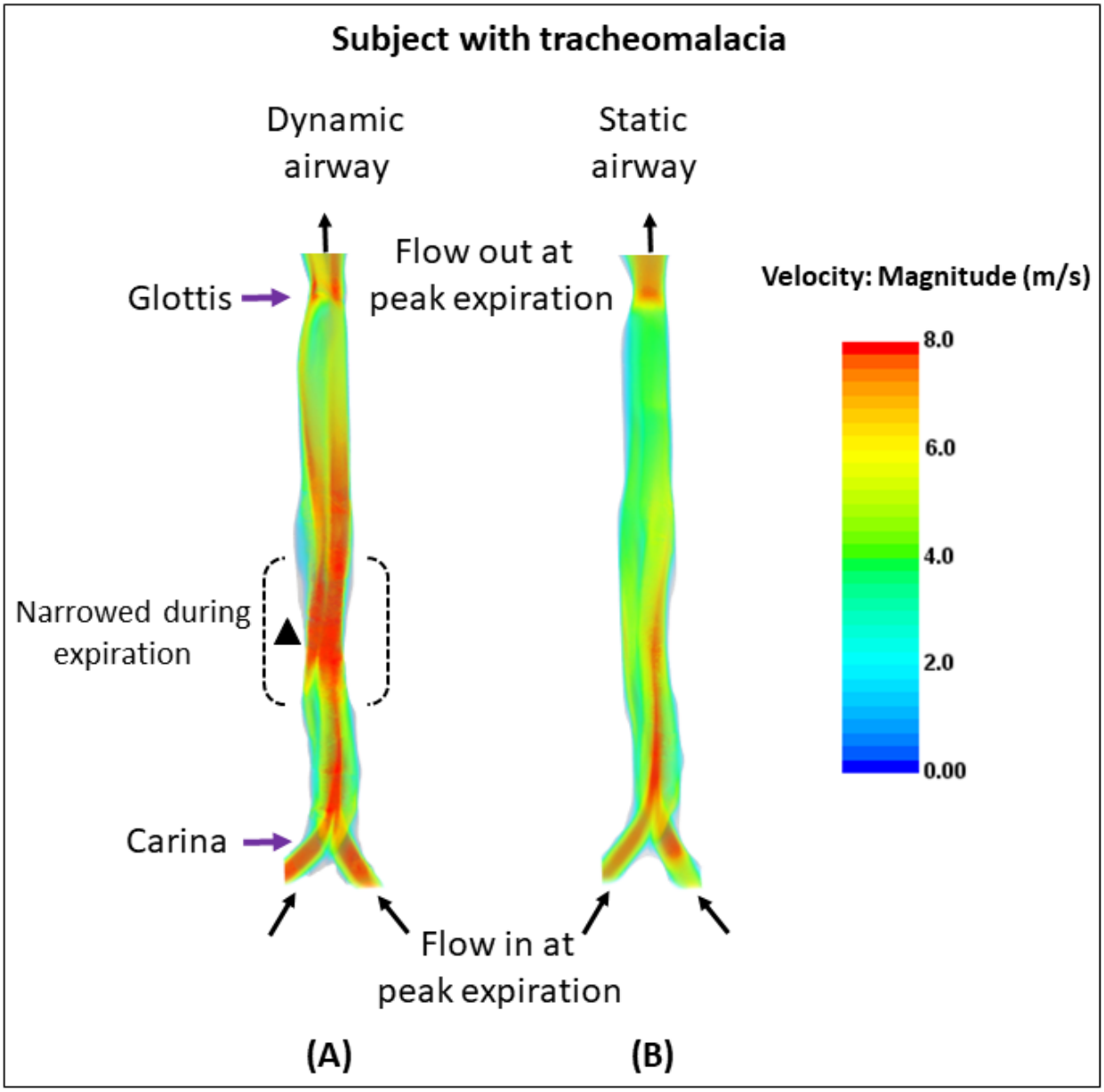

Figure 6.3: Airflow velocity profiles of the dynamic (A) and static (B) airway (coronal plane) in a subject with TM at peak expiration. There is a strong jet at the middle of the trachea in the dynamic airway due to narrowing. Reprinted with permission of the American Thoracic Society. Copyright © 2021 American Thoracic Society. All rights reserved [54].

6.3.4 Analysis of Daily TR-WOB

On average, the daily TR-WOB calculated for subjects without TM was 51.0 ± 32.3 J in the static CFD simulation and 60.4 ± 35.7 J in the dynamic CFD simulation (Figure 6.4A). In contrast, the average daily TR-WOB of the subjects with TM was 89.9 ± 71.9 J in the static case and 437.2 ± 454.1 J in the dynamic case. Figure 6.4B shows the increase in TR-WOB of all subjects based on airway condition. The average increase in TR-WOB of the subject without TM was 24% ± 14% (range 10-38%) and 337% ± 295% (range 50-848%) of the subjects with TM ($p < 0.02$).

Figure 6.4C shows the increase in TR-WOB due to airway motion based on the respiratory support at the time of MRI. There were six subjects in each study group using room air or HFNC and two subjects with TM were using CPAP via RAM cannula during the MRI scan. On average, the increase in TR-WOB of the subjects without TM was 24% ± 14% and 428% ± 288% of the subjects with TM on room air/HFNC. However, the average increase in TR-WOB of the two subjects with TM using RAM CPAP was 67% ± 23%. This percentage decrease in TR-WOB of the two subjects with TM suggests that RAM CPAP may have dropped the energy expenditure.

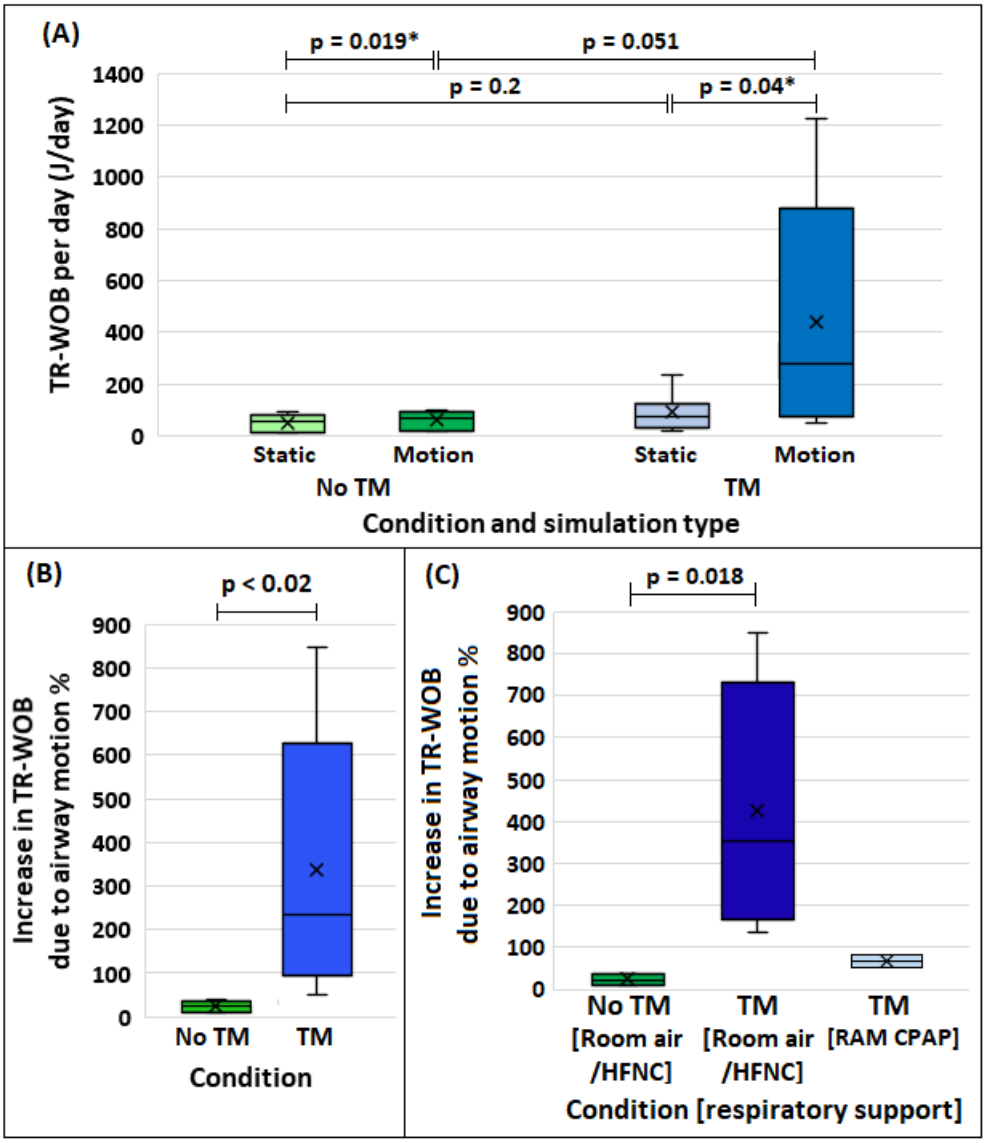

Figure 6.4: The TR-WOB per day in the static and dynamic airways of the subjects diagnosed with and without TM (A). The increase in TR-WOB due to airway motion as a percentage compared to static airway based on airway condition (B) and on the type of respiratory support at the time of MRI (C). The plot elements: average (cross); median (black line); interquartile range (colored box); data within 1.5 times the interquartile range below 25% or above 75% (whiskers) * Paired t-test was used to calculate p-values. Reprinted with permission of the American Thoracic Society. Copyright © 2021 American Thoracic Society. All rights reserved [54].

6.4 Discussion and Conclusions

This is the first study that illustrates the increase in WOB component of the trachea in neonates due to TM. This study demonstrates a new technique to quantify the breathing effort in the airway regionally, using UTE MRI and CFD. The main takeaway message of this study is that the TR-WOB of the subjects with TM was higher than the subjects without TM due to airway motion. Another finding was that RAM CPAP may be able to reduce the energy expenditure of these newborns who require oxygen to support breathing. More CFD simulations may need to perform with a larger number of subjects since this finding is based on two subjects. However, previous studies have reported CPAP increases expiratory flow rates and lung volumes in newborns with TM by improving lung mechanics [114,115].

Figure 6.4 suggests that airway motion increases TR-WOB in the subjects with TM. However, TR-WOB calculated using the static airway was also greater in the subjects with TM than subjects without TM. The results are not statistically significant, but it suggests that tracheas are not completely open during inspiration with subjects with airway disease.

Previous studies have calculated the total (resistive and elastic) WOB of the respiratory system [116–119]. The following Table 6.2 is a summary of subject demographics and respiratory system resistive WOB values of the previous studies [54]. Three studies have calculated WOB values for neonatal subjects with different respiratory diseases and one study has calculated WOB values for healthy neonatal subjects. The total resistive WOB of the respiratory system values reported in the literature is greater than that for healthy neonates.

Table 6.2: Previous studies subject information and WOB values

Study	Average gestational age (weeks)	Average age at study (days)	Average weight at study (kg)	Clinical diagnosis	Respiratory system resistive WOB (J/day)	Additional remarks
Levy et al.	29.7 ± 2.1	33.6 ± 1.4	1.757 ± 0.248	Healthy	89.28	Premature infants nearing discharge from the NICU
Pandit et al.	28 ± 1.7	14 ± 13	- Median (range) 1.151 (0.664 – 1.461)	Apnea or mild respiratory distress	188.64*	Nasal continuous positive airway pressure (NCPAP) at 0 cmH_2O
Bhutani et al.	34.4 ± 1.3	< 2	2.129 ± 0.598	Respiratory distress syndrome	616.32	-
Courtney et al.	27.9 ± 2.0	4.6 ± 4.3	1.092 ± 0.222	Mild respiratory distress	442.08	NCPAP at 0 cmH_2O

*Calculations are based on the median weight.

Figure 6.5 shows the comparison between our findings of the TR-WOB and total resistive WOB of the respiratory system in previous studies. On average, the daily TR-WOB of the subjects without TM was 60.4 ± 35.7 J and 437.2 ± 454.1 J of the subjects with TM. Our findings of the TR-WOB in the subjects without TM is a fraction of the total resistive WOB of the respiratory system results reported by Levy et al. [116] based on healthy neonates. Similarly, TR-WOB values reported for subjects with TM is also significantly higher than other studies with different diseases such as respiratory distress syndrome or apnea.

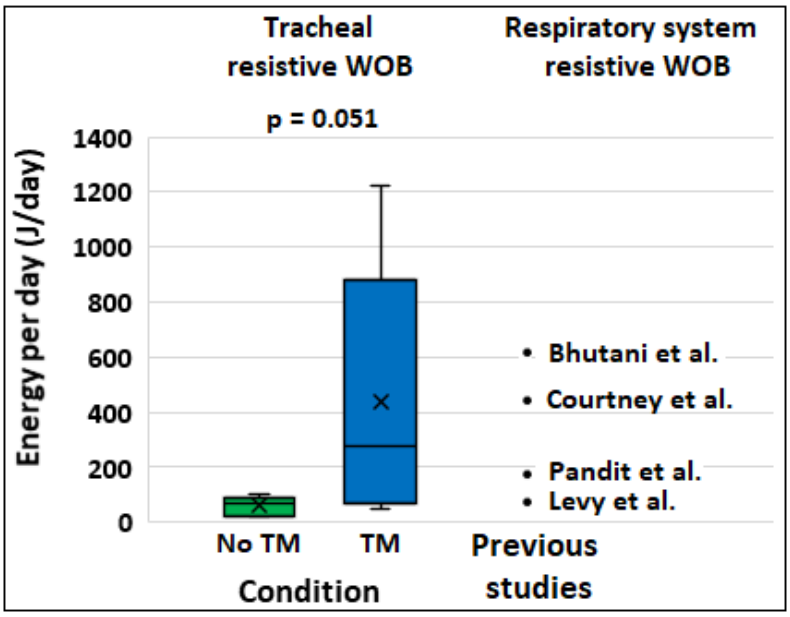

Figure 6.5: The daily energy expenditure values of neonates reported in the present study and in previous studies. Our results show the resistive WOB component in the trachea and previous study results show the resistive WOB of the entire respiratory system. The plot elements: average (cross); median (black line); interquartile range (colored box); data within 1.5 times the interquartile range below 25% or above 75% (whiskers). Reprinted with permission of the American Thoracic Society. Copyright © 2021 American Thoracic Society. All rights reserved [54].

On average, the increase in TR-WOB compared to static airway was 427.7% in six subjects with TM using room air or HFNC (Figure 6.6C). This suggests that neonates with TM expend five times more energy due to airway motion for breathing than its airway held static. The increase in WOB of the subjects with TM may be greater than the values reported here as the airway model only included the central airway. Newborns with airway issues spend more energy for breathing and it limits their growth which requires more energy during the early stage of life. The findings of this study suggest that TM may impact the growth and development of newborns.

7 Auto-PEEP due to Glottis Closure

As seen in previous chapters, airflow through the opening between the vocal folds at the glottis impacts airflow in the trachea. This chapter reveals the role of the glottis on airflow in newborns with TM. All results have been submitted to the journal *Chest*.

7.1 Introduction

The glottis is the narrowest location in the airway in most cases. Previous studies have modeled glottis motion to study particle deposition and to quantify energy expenditure in the airway [120,121]. A study demonstrated that the glottis narrowed in adult subjects with chronic obstructive lung disease (COPD) to self-generate positive end expiratory pressure (auto-PEEP) [122]. It is assumed that glottis narrowing prevents airway collapse by increasing pressure inside the airways[123]. Another study based on neonates showed that intrapleural pressure was elevated due to glottis closure [124]. However, auto-PEEP has not been demonstrated in newborns with TM.

This study hypothesized that newborns with TM narrow their glottises to generate auto-PEEP, particularly during expiration. The glottis motion was studied using the four MR images, which represent different phases during breathing. CFD simulations were performed with airway motion to quantify the pressure difference across the glottis and throughout the central airway during the breathing cycle.

7.2 Methods

This study included 21 neonatal subjects after receiving the Institutional Review Board approval and parental consent. All subjects were not intubated and were using room air or non-invasive respiratory support at the time of MRI. Clinical bronchoscopy was performed to diagnose TM in 14 of the 21 subjects and the rest of the subjects did not undergo bronchoscopy. Three of the seven subjects were considered respiratory controls since they did not exhibit any airway or lung defects. The diagnosis of TM in four of the seven subjects was evaluated based on the maximum tracheal cross-sectional area change during breathing [13].

UTE MRI was performed for each subject and was reconstructed to obtain 4 MR images which represent different phases during breathing. More details on UTE imaging and image reconstruction can be found in Chapters 2.3 and 2.4. For each subject, CFD simulation was performed with patient-specific airway motion and airflow rates derived via MRI (Chapter 4). STAR-CCM+ 14.04.011-R8 version was used to run each simulation. Briefly, CFD mesh included 2 million cells with 9 prism layers on the wall and the interior was built with polyhedral cells. The temporal resolution of the CFD simulation was 0.8 ms. More details on CFD simulations can be found in Chapter 3.

The total pressure loss from the nasopharynx to carina was calculated from the CFD simulation. A centerline was created for each airway to calculate the cross-sectional areas along the airway [74,102,125]. The cross-sectional area of the glottis was obtained during the breathing cycle. A two-tailed t-test (unpaired and unequal variance) was implemented to compare the results of the 21 subjects.

7.3 Results

7.3.1 Study Subjects

Table 7.1 shows the clinical diagnosis, PMA, weight, and respiratory support at MRI. In 18 out of 21 subjects were clinically diagnosed with BPD, TEF/EA, and bronchoesophageal fistula (BEF) [54]. On average, the weight and length of the subjects were 3.4 ± 0.7 kg and 48.2 ± 3.9 cm, respectively.

Table 7.1: Subject information

Airway condition/ (N)	Clinical Diagnosis	PMA at MRI (wk)	Weight at MRI (kg)	Respiratory Support at MRI	Cohort N
No TM (10)	BPD	41 ± 2	3.55 ± 0.40	Room air	1
				HFNC	5
	BEF	40	3.7	Room air	1
	Respiratory control	40 ± 1	3.45 ± 0.54	Room air	3
TM (11)	BPD	41 ± 3	3.43 ± 1.21	Room air	2
				HFNC	1
				RAM CPAP	4
	TEF/ EA	40 ± 1	2.87 ± 0.23	Room air	2
				HFNC	1
				RAM CPAP	1

7.3.2 Glottis Movement during the Breath

Figure 7.1 shows the glottis lumen cross-sectional plane derived from the segmented airway in a subject without TM. The graph on the right shows the change in the glottis cross-sectional area during the breathing cycle in a subject with and without TM. Glottis cross-sectional area increases during inspiration and decreases during expiration. The main difference between the subject with TM and without TM was that the glottis cross-sectional area at peak expiration was smaller compared to its end expiration time point in the subject with TM. Five out of 11 subjects with TM demonstrated similar behavior as shown in the plot. The rest of the subjects with TM demonstrated a similar pattern compared to subjects without TM with smaller glottis area during the breathing cycle.

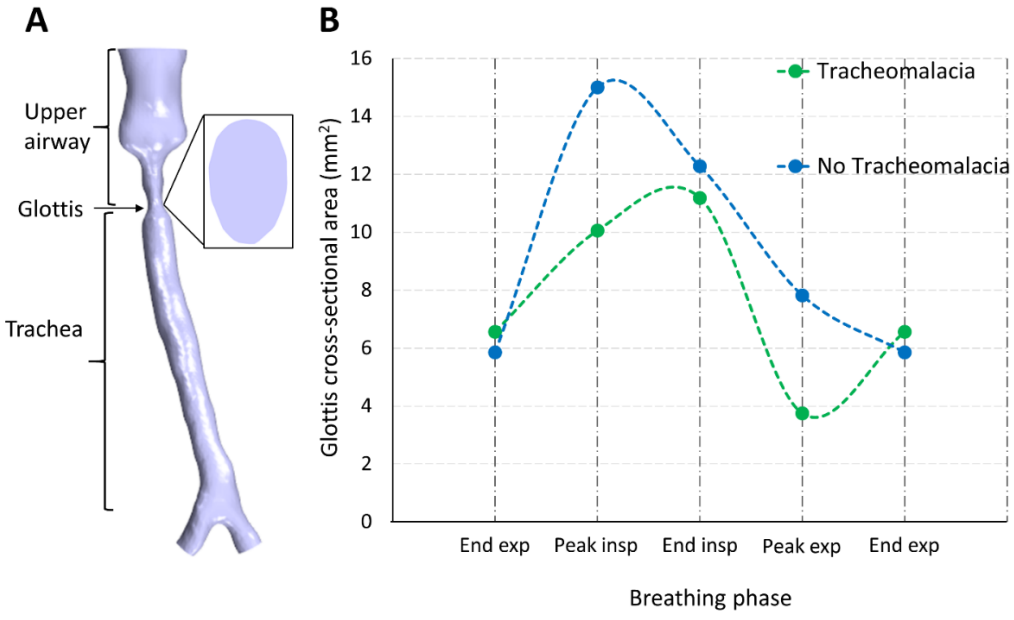

Figure 7.1: Glottis cross-sectional area in a subject without TM derived from the segmented airway (A). Glottis cross-sectional area during the breathing cycle in a subject without TM (blue) and with TM (green) (B).

The average glottis cross-sectional area at peak expiration was 10.3 ± 4.4 mm^2 in the subjects without TM and 4.0 ± 1.1 mm^2 in the subjects with TM (Figure 7.2). When the glottis area was normalized by the length, weight, or body surface area of each subject, similar results were observed.

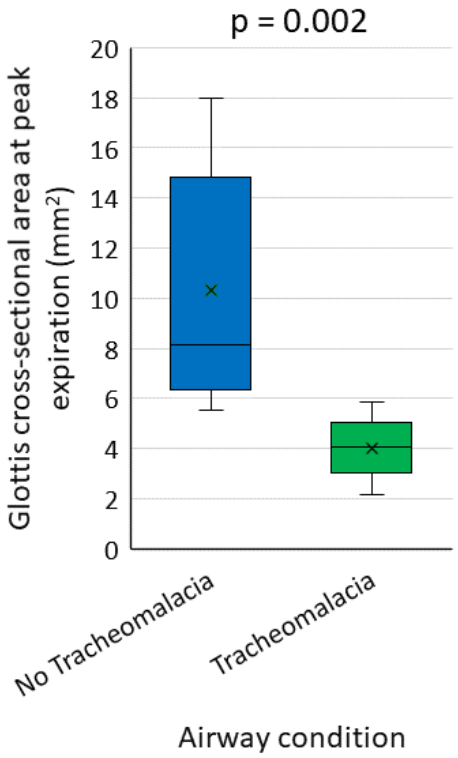

Figure 7.2: Glottis cross-sectional area at peak expiration of the 21 subjects. Green and blue colored boxes represent the glottis cross-sectional area of the subject with TM and without TM, respectively. Plot elements; mean = cross; median = solid line; interquartile range (IQR) = box; data within 1.5 times the IQR below 25% or above 75% = whiskers.

7.3.3 Total Pressure Loss along the Airway

After conducting patient-specific CFD simulations, total pressure loss along the airway was calculated for each subject. Figure 7.3 demonstrates the total pressure loss along the airway at peak expiration of an example subject with TM and without TM. The total pressure loss through the glottis for the subject with TM was 2.27 cmH_2O and 0.21 cmH_2O for the subject without TM. The glottis cross-sectional area of the two example subjects was 7.8 mm^2 (subject without TM) and 2.2 mm^2 (subject with TM).

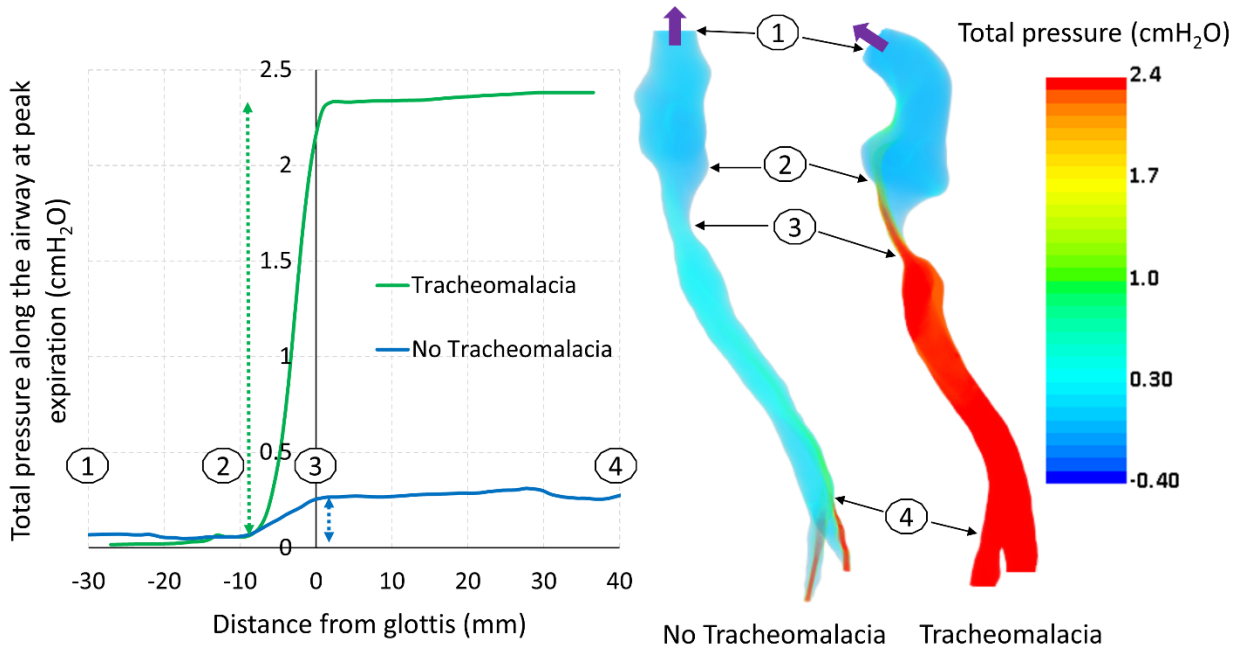

Figure 7.3: The total pressure loss along the airway at peak expiration in a subject with TM (green) and without TM (blue). The position of the nasopharynx, larynx, glottis, and carina are numbered 1, 2, 3, and 4, respectively. The total pressure loss through the glottis in the subject with TM and without TM is represented by green and blue dashed arrows, respectively.

In order to compare the effect of the glottis at peak expiration, the total pressure loss across the glottis was measured for all subjects and compared with the airway condition Figure 7.4A. On average, the total pressure loss through the glottis at peak expiration in the subjects with TM and without TM was 2.88 ± 2.29 cmH_2O and 0.26 ± 0.16 cmH_2O, respectively ($p = 0.005$). Figure 7.4B demonstrates the total pressure loss from the larynx to carina at peak expiration. On average, total pressure loss at peak expiration from the larynx to carina of the subjects with TM and without TM was 3.60 ± 2.56 cmH_2O and 0.41 ± 0.19 cmH_2O, respectively ($p = 0.003$). Figure 7.4C shows the pressure loss through the glottis compared to the total pressure loss from the larynx to carina. On average, $79\% \pm 20\%$ of the total pressure loss occurred in the glottis in the subject with TM and $60\% \pm 19\%$, in the subjects without TM compared to the total pressure loss from the larynx to carina ($p = 0.042$). Similar results were observed after normalizing all pressure values by the length, weight, or body surface area of each subject.

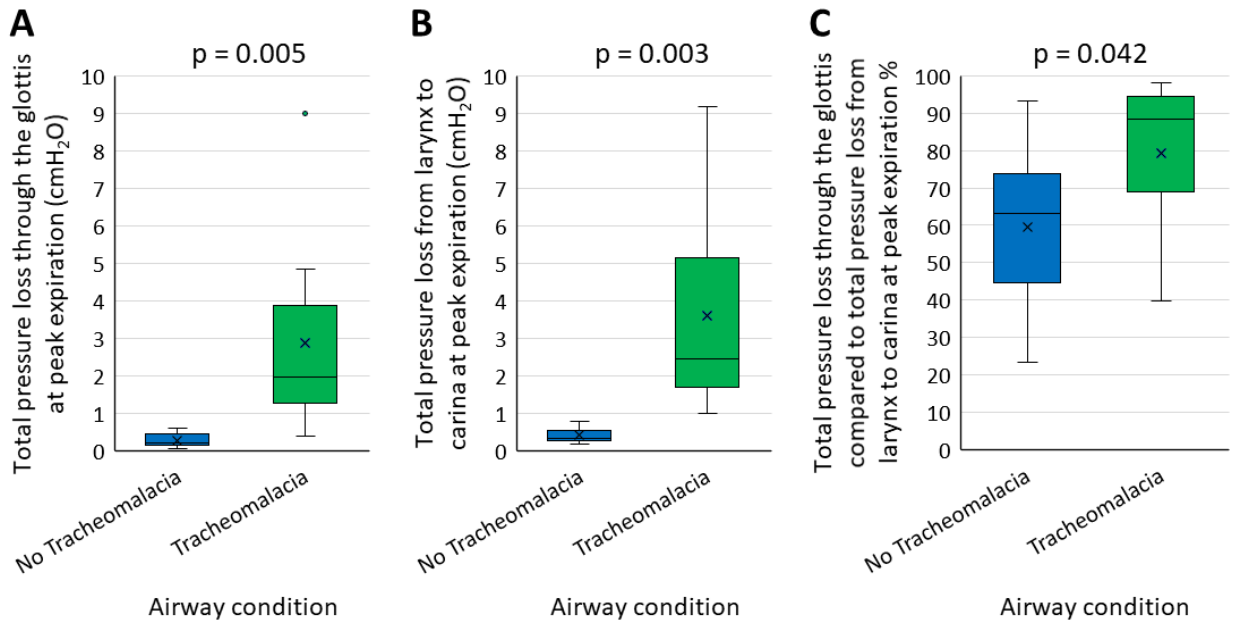

Figure 7.4: The total pressure loss across the glottis (A), total pressure loss from the larynx to carina (B), and the total pressure loss across the glottis as a percentage compared to total pressure loss from the larynx to carina. Plot elements; median = solid line; mean = cross; interquartile range (IQR) = box; data within 1.5 times the IQR below 25% or above 75% = whiskers; outlier = circle.

As seen in Figure 7.1B, the glottis cross-sectional area of the subject with TM was smaller than the subject without TM at other time points during the breathing cycle (peak inspiration). The average glottis cross-sectional area during the breathing cycle for the subjects with TM was 5.5 ± 1.9 mm^2 and 11.3 ± 3.1 mm^2 of the subjects without TM ($p < 0.001$, Figure 7.5A). Figure 7.5B shows the total pressure loss from the larynx to carina at peak inspiration. On average, the total pressure loss for the subjects with TM was 2.65 ± 2.35 cmH_2O and 0.29 ± 0.18 cmH_2O for the subjects without TM ($p = 0.01$).

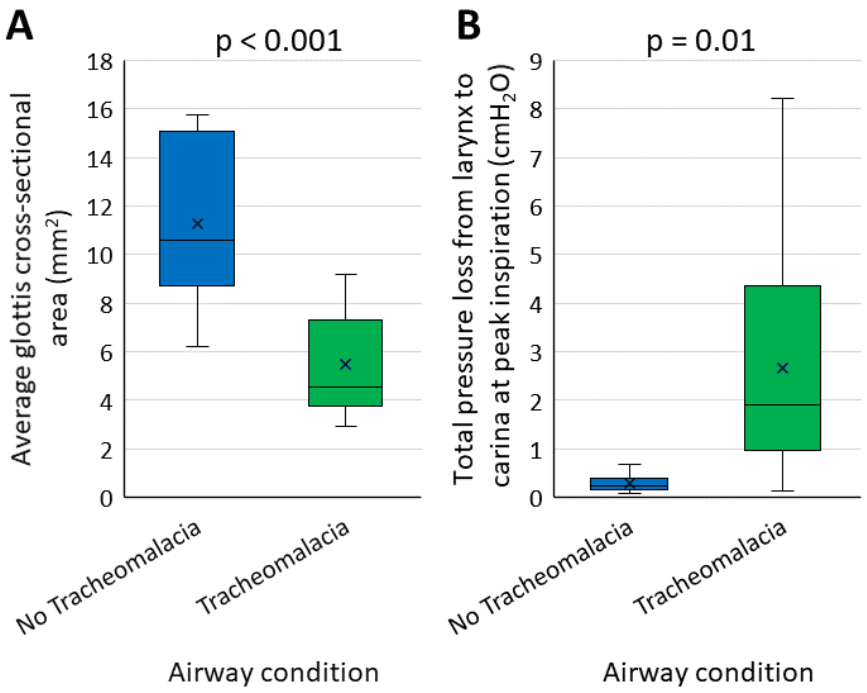

Figure 7.5 Average glottis cross-sectional area during the breathing cycle (A), total pressure loss from the larynx to carina at peak inspiration time point (B). Plot elements; median = solid line; mean = cross; interquartile range (IQR) = box; data within 1.5 times the IQR below 25% or above 75% = whiskers.

7.4 Discussion and Conclusions

This is the first study that shows neonates with TM use auto-PEEP. The narrowing of the glottis during expiration raised pressure in the airway of the subjects with TM, there by acting as auto-PEEP. Previous studies have reported glottis narrowing in children and adults. During the first 16 hours after birth, newborns diagnosed with respiratory distress syndrome narrowed their glottises during expiration [124]. Furthermore, a study showed the increased subglottic pressure and laryngeal resistance due to glottis closure in children diagnosed with Down syndrome [126]. Baz et al. [122] showed that adults with COPD narrowed their glottises than healthy controls.

Previous studies have used invasive techniques to assess glottis motion and to measure pressure in the airway. A fibreoptic nasenodoscope was used to record the movement of the glottis during the breathing cycle and a balloon was inserted to measure the pressure [122,124,127]. These invasive procedures can change the dynamics of the airway and affect airflow. However, the imaging method applied in this study is non-ionizing and non-invasive. CFD simulations used to derive the pressure along the airway can calculate pressure regionally and reveal more information on the airflow that cannot be obtained from other techniques.

The total pressure loss through the glottis in subjects with TM was 10 times higher than in subjects without TM due to the narrowing of the glottis (Figure 7.4A). This increased pressure across the glottis elevated the total pressure loss in the trachea and as a result, neonates with TM require more energy for breathing [54]. This study assumed that the neonates with TM attempt to avoid tracheal collapse by increasing pressure in the trachea during expiration.

Figure 7.5A indicates that neonates with TM have a smaller glottis area throughout the breathing cycle, including inspiration. A previous study has reported that the glottis was narrowed

during inspiration in a study involving adults with airway obstruction [128]. Subjects with disease narrowed their glottises during expiration compared to controls during normal breathing. Although, when they performed the forced spirometry test (i.e. breathing with a higher rate, 1 Hz to 3 Hz), patients with forced expiratory volume in 1 second (FEV_1) less than 80% narrowed their glottises during inspiration while subjects with normal FEV_1 opened glottis more during breathing.

There are a few clinical implications of auto-PEEP and glottis narrowing. Auto-PEEP avoids collapsing small airways during breathing and improves gas exchange [123,126,129–131]. In infants with TM, PEEP acts as a pneumatic stent for the collapsible region of the trachea and raises lung volumes [114,132]. However, glottis narrowing increases upper airway resistance and limits the aerosol drug delivery to lower airways [5,120].

8 Limitations and Future Directions

UTE MRI is widely used in research settings and MR image quality has improved rapidly in recent years. These improvements allow MR images to reconstruct at different phases of breathing. However, there are a few limitations associated with this study. UTE MR images were acquired in more than 150 newborns at the NICU over the last several years. Most of the subjects were intubated at the time of MRI. Since the endotracheal tube can affect the airway motion, neonates intubated at the time of MRI were excluded. Some of the subjects were not included due to limited image coverage and the MR image quality. Another limitation of the study was the temporal resolution of MRI, which was approximately one-quarter of the breathing cycle. The image acquisition window was half of the temporal resolution of MRI and airway motion faster than this resolution was not captured and modeled in this study.

Currently, respiratory CFD is not available in clinical settings. However, CFD simulations are performed in cardiovascular medicine to diagnose coronary artery disease with the approval of U.S. Food and Drug Administration [133,134]. CFD simulations are computationally expensive and take a relatively long time to complete. These patient-specific CFD simulations take approximately 1000 core-hours.

In addition to these drawbacks, new methods can be applied in the future to improve performance in specific fields.

1. Airway coverage

In the majority of cases, the airway geometry used in the CFD simulation extended from the main bronchi to the nasopharynx. More information on airflow can be obtained if the airway model can include starting from the nostrils to a few branches below the main bronchi. Dynamic CT can be used as an alternative for MRI.

2. Image reconstruction

Each data point in the FID waveform weighted equally to reconstruct MR images (hard gating). However, different weighting values may be applied to improve image quality and to reduce blurring (soft gating).

3. Airway motion

In this study, airway surface registration was performed rather than image registration, which requires airway segmentation in all four time points to obtain airway motion. However, airway segmentation is time-consuming and in the future, image registration can be applied to obtain airway motion during the breathing cycle.

The techniques used in this study can be applied to older infants and adults with airway diseases such as sleep apnea, laryngomalacia, retrognathia, and bilateral vocal cord paralysis. In addition, these patient-specific CFD simulations can be used for surgical planning and to assess the airway regionally.

Bibliography

[1] R.J. Pierce, C.J. Worsnop, Upper airway function and dysfunction in respiration, Clin. Exp. Pharmacol. Physiol. 26 (1999) 1–10.

[2] E. Hernández-Cortez, Airway in the Newborn Patient, J. Anesth. Crit. Care Open Access. 5 (2016).

[3] Z. Zhang, Regulation of glottal closure and airflow in a three-dimensional phonation model: Implications for vocal intensity control, J. Acoust. Soc. Am. 137 (2015) 898–910.

[4] M. Brouns, S. Verbanck, C. Lacor, Influence of glottic aperture on the tracheal flow, J. Biomech. 40 (2007) 165–172.

[5] A.H. Campbell, H. Imberger, B. McC. Jones, Increased upper airway resistance in patients with airway narrowing, Br. J. Dis. Chest. 70 (1976) 58–65.

[6] E.B. Hysinger, H.B. Panitch, Paediatric Tracheomalacia, Paediatr. Respir. Rev. 17 (2016) 9–15.

[7] V.. M. McNamara, D.C.. C.G. Crabbe, Tracheomalacia, Paediatr. Respir. Rev. 5 (2004) 147–154.

[8] G.C. Smaldone, Excessive dynamic airway collapse: Fact, fiction, or flow limitation, Ann. Am. Thorac. Soc. 14 (2017) 301–302.

[9] R. Boogaard, S.H. Huijsmans, M.W.H. Pijnenburg, H.A.W.M. Tiddens, J.C. De Jongste, P.J.F.M. Merkus, Tracheomalacia and bronchomalacia in children: Incidence and patient characteristics, Chest. 128 (2005) 3391–3397.

[10] E.B. Hysinger, N.L. Friedman, M.A. Padula, R.T. Shinohara, H. Zhang, H.B. Panitch, S.M. Kawut, Tracheobronchomalacia is associated with increased morbidity in bronchopulmonary dysplasia, Ann. Am. Thorac. Soc. 14 (2017) 1428–1435.

[11] M. McCubbin, E.E. Frey, J.S. Wagener, R. Tribby, W.L. Smith, Large airway collapse in bronchopulmonary dysplasia, J. Pediatr. 114 (1989) 304–307.

[12] I.B. Masters, P. V. Zimmerman, N. Pandeya, H.L. Petsky, S.B. Wilson, A.B. Chang, Quantified tracheobronchomalacia disorders and their clinical profiles in children, Chest. 133 (2008) 461–467.

[13] E.B. Hysinger, A.J. Bates, N.S. Higano, D. Benscoter, R.J. Fleck, C.K. Hart, G. Burg, A. De Alarcon, P.S. Kingma, J.C. Woods, Ultrashort echo-time MRI for the assessment of tracheomalacia in neonates, Chest. 157 (2020) 595–602.

[14] A.J. Bates, N.S. Higano, E.B. Hysinger, R.J. Fleck, A.D. Hahn, S.B. Fain, P.S. Kingma, J.C. Woods, Quantitative assessment of regional dynamic airway collapse in neonates via retrospectively respiratory-gated 1H ultrashort echo time MRI, J. Magn. Reson. Imaging. 49 (2019) 659–667.

[15] K.Y. Wu, E.A. Jensen, A.M. White, Y. Wang, D.M. Biko, K. Nilan, M. V. Fraga, L. Mercer-Rosa, H. Zhang, H. Kirpalani, Characterization of Disease Phenotype in Very Preterm Infants with Severe ronchopulmonary Dysplasia, Am. J. Respir. Crit. Care Med. 201 (2020) 1398–1406.

[16] D. Masui, S. Fukahori, N. Hashizume, S. Ishii, M. Yagi, High-flow nasal cannula therapy for severe tracheomalacia associated with esophageal atresia, Pediatr. Int. 61 (2019) 1060–1061.

[17] K. Vézina, S. Laberge, T.T.D. Nguyen, Home high-flow nasal cannula as a treatment for severe tracheomalacia: A pediatric case report, Pediatr. Pulmonol. 52 (2017) E43–E45.

[18] Q. Mok, Airway problems in neonates-A review of the current investigation and management strategies, Front. Pediatr. 5 (2017) 60.

[19] E. Hysinger, N. Friedman, E. Jensen, H. Zhang, J. Piccione, Bronchoscopy in neonates with severe bronchopulmonary dysplasia in the NICU, J. Perinatol. 39 (2019) 263–268.

[20] L. Spitz, Oesophageal atresia, Orphanet J. Rare Dis. 2 (2007).

[21] S. Lee, Basic Knowledge of Tracheoesophageal Fistula and Esophageal Atresia, Adv. Neonatal Care. 18 (2018) 14–21.

[22] R. Sfeir, L. Michaud, J. Salleron, F. Gottrand, Epidemiology of esophageal atresia, Dis. Esophagus. 26 (2013) 354–355.

[23] P.G. Zaveri, A.M. Vogel, A.J. Vachharajani, Late preterm baby with recurrent respiratory distress, Neoreviews. 15 (2014) e199–e201.

[24] J.C. Woods, J.C. Schittny, Lung Structure at Preterm and Term Birth, Fetal Neonatal Lung Dev. (2015) 124–138.

[25] C.J. Bradshaw, H. Thakkar, L. Knutzen, R. Marsh, M. Pacilli, L. Impey, K. Lakhoo, Accuracy of prenatal detection of tracheoesophageal fistula and oesophageal atresia, J. Pediatr. Surg. 51 (2016) 1268–1272.

[26] N.S. Higano, A.J. Bates, J.A. Tkach, R.J. Fleck, F.Y. Lim, J.C. Woods, P.S. Kingma, Pre- and post-operative visualization of neonatal esophageal atresia/tracheoesophageal fistula via magnetic resonance imaging, J. Pediatr. Surg. Case Reports. 29 (2018) 5–8.

[27] J.A.N. Robert J. Mason, V.Courtney Broaddus, Thomas R Martin, Talmadge E King, Dean Schraufnagel, John F. Murray, Murray and Nadel's Textbook of Respiratory Medicine E-Book: 2-Volume Set, 2010.

[28] A.H. Jobe, E. Bancalari, Bronchopulmonary dysplasia, in: Am. J. Respir. Crit. Care Med., American Lung Association, 2001: pp. 1723–1729.

[29] K.R. Stenmark, S.H. Abman, Lung vascular development: Implications for the pathogenesis of bronchopulmonary dysplasia, Annu. Rev. Physiol. 67 (2005) 623–661.

[30] B.J. Stoll, N.I. Hansen, E.F. Bell, S. Shankaran, A.R. Laptook, M.C. Walsh, E.C. Hale, N.S. Newman, K. Schibler, W.A. Carlo, K.A. Kennedy, B.B. Poindexter, N.N. Finer, R.A. Ehrenkranz, S. Duara, P.J. Sánchez, T.M. O'Shea, R.N. Goldberg, K.P. Van Meurs, R.G. Faix, D.L. Phelps, I.D. Frantz, K.L. Watterberg, S. Saha, A. Das, R.D. Higgins, Neonatal outcomes of extremely preterm infants from the NICHD Neonatal Research Network, Pediatrics. 126 (2010) 443–456.

[31] N.S. Higano, D.R. Spielberg, R.J. Fleck, A.H. Schapiro, L.L. Walkup, A.D. Hahn, J.A. Tkach, P.S. Kingma, S.L. Merhar, S.B. Fain, J.C. Woods, Neonatal pulmonary magnetic resonance imaging of bronchopulmonary dysplasia predicts short-term clinical outcomes, Am. J. Respir. Crit. Care Med. 198 (2018) 1302–1311.

[32] P.J. Critser, N.S. Higano, J.A. Tkach, E.S. Olson, D.R. Spielberg, P.S. Kingma, R.J. Fleck, S.M. Lang, R.A. Moore, M.D. Taylor, J.C. Woods, Cardiac magnetic resonance imaging evaluation of neonatal bronchopulmonary dysplasia-associated pulmonary hypertension, Am. J. Respir. Crit. Care Med. 201 (2020) 73–82.

[33] L.L. Walkup, J.A. Tkach, N.S. Higano, R.P. Thomen, S.B. Fain, S.L. Merhar, R.J. Fleck,

R.S. Amin, J.C. Woods, Quantitative magnetic resonance imaging of bronchopulmonary dysplasia in the neonatal intensive care unit environment, Am. J. Respir. Crit. Care Med. 192 (2015) 1215–1222.

[34] J.L. Slaughter, P.B. Reagan, T.B. Newman, M.A. Klebanoff, Comparative effectiveness of nonsteroidal anti-inflammatory drug treatment vs no treatment for patent ductus arteriosus in preterm infants, JAMA Pediatr. 171 (2017) e164354.

[35] R. Ramanathan, Pharmacology review: Bronchopulmonary dysplasia and diuretics, Neoreviews. 9 (2008) e260–e267.

[36] J.C. Euteneuer, E. Kerns, C. Leiting, R.J. McCulloh, E.S. Peeples, Inhaled bronchodilator exposure in the management of bronchopulmonary dysplasia in hospitalized infants, J. Perinatol. 41 (2021) 53–61.

[37] W. Gerlach, O. Stern, Der experimentelle Nachweis des magnetischen Moments des Silberatoms, Zeitschrift Für Phys. 8 (1922) 110–111.

[38] W. Gerlach, O. Stern, Das magnetische Moment des Silberatoms, Zeitschrift Für Phys. 9 (1922) 353–355.

[39] W. Gerlach, O. Stern, Der experimentelle Nachweis der Richtungsquantelung im Magnetfeld, Zeitschrift Für Phys. 9 (1922) 349–352.

[40] Y. Ohashi, K. Sakai, H. Hase, N. Joki, Dry weight targeting: The art and science of conventional hemodialysis, Semin. Dial. 31 (2018) 551–556.

[41] M.M. Harjai, Fluid and electrolyte concepts in new borns [2], Med. J. Armed Forces India. 58 (2002) 182–183.

[42] H. Hatabu, D.C. Alsop, J. Listerud, M. Bonnet, W.B. Gefter, T2* and proton density measurement of normal human lung parenchyma using submillisecond echo time gradient echo magnetic resonance imaging, Eur. J. Radiol. 29 (1999) 245–252.

[43] C.J. Bergin, J.M. Pauly, A. Macovski, Lung parenchyma: Projection reconstruction MR imaging, Radiology. 179 (1991) 777–781.

[44] J. Yu, Y. Xue, H.K. Song, Comparison of lung T2* during free-breathing at 1.5 T and 3.0 T with ultrashort echo time imaging, Magn. Reson. Med. 66 (2011) 248–254.

[45] J.D. Mathews, A. V. Forsythe, Z. Brady, M.W. Butler, S.K. Goergen, G.B. Byrnes, G.G. Giles, A.B. Wallace, P.R. Anderson, T.A. Guiver, P. McGale, T.M. Cain, J.G. Dowty, A.C. Bickerstaffe, S.C. Darby, Cancer risk in 680 000 people exposed to computed tomography scans in childhood or adolescence: Data linkage study of 11 million Australians, BMJ. 346 (2013).

[46] B. Huang, M.W.M. Law, P.L. Khong, Whole-body PET/CT scanning: Estimation of radiation dose and cancer risk, Radiology. 251 (2009) 166–174.

[47] D.L. Miglioretti, E. Johnson, A. Williams, R.T. Greenlee, S. Weinmann, L.I. Solberg, H.S. Feigelson, D. Roblin, M.J. Flynn, N. Vanneman, R. Smith-Bindman, The use of computed tomography in pediatrics and the associated radiation exposure and estimated cancer risk, JAMA Pediatr. 167 (2013) 700–707.

[48] M.S. Pearce, J.A. Salotti, M.P. Little, K. McHugh, C. Lee, K.P. Kim, N.L. Howe, C.M. Ronckers, P. Rajaraman, A.W. Craft, L. Parker, A.B. De González, Radiation exposure from CT scans in childhood and subsequent risk of leukaemia and brain tumours: A retrospective cohort study, Lancet. 380 (2012) 499–505.

[49] A.D. Hahn, N.S. Higano, L.L. Walkup, R.P. Thomen, X. Cao, S.L. Merhar, J.A. Tkach, J.C. Woods, S.B. Fain, Pulmonary MRI of neonates in the intensive care unit using 3D ultrashort echo time and a small footprint MRI system, J. Magn. Reson. Imaging. 45 (2017) 463–471.

[50] K.M. Johnson, S.B. Fain, M.L. Schiebler, S. Nagle, Optimized 3D ultrashort echo time pulmonary MRI, Magn. Reson. Med. 70 (2013) 1241–1250.

[51] G. Dournes, D. Grodzki, J. Macey, P.O. Girodet, M. Fayon, J.F. Chateil, M. Montaudon, P. Berger, F. Laurent, Erratum: Quiet Submillimeter MR Imaging of the Lung Is Feasible with a PETRA Sequence at 1.5 T, Radiology. 279 (2016) 328.

[52] M. Lederlin, Y. Crémillieux, Three-dimensional assessment of lung tissue density using a clinical ultrashort echo time at 3 tesla: A feasibility study in healthy subjects, J. Magn. Reson. Imaging. 40 (2014) 839–847.

[53] C.C. Gunatilaka, A. Schuh, N.S. Higano, J.C. Woods, A.J. Bates, The effect of airway motion and breathing phase during imaging on CFD simulations of respiratory airflow, Comput. Biol. Med. 127 (2020) 104099.

[54] C.C. Gunatilaka, N.S. Higano, E.B. Hysinger, D.B. Gandhi, R.J. Fleck, A.D. Hahn, S.B. Fain, J.C. Woods, A.J. Bates, Increased work of breathing due to tracheomalacia in neonates, Ann. Am. Thorac. Soc. 17 (2020) 1247–1256.

[55] N.S. Higano, A.D. Hahn, J.A. Tkach, X. Cao, L.L. Walkup, R.P. Thomen, S.L. Merhar, P.S. Kingma, S.B. Fain, J.C. Woods, Retrospective respiratory self-gating and removal of bulk motion in pulmonary UTE MRI of neonates and adults, Magn. Reson. Med. 77 (2017) 1284–1295.

[56] M. Tibiletti, A. Bianchi, Å. Kjørstad, S. Wundrak, D. Stiller, V. Rasche, Respiratory self-gated 3D UTE for lung imaging in small animal MRI, Magn. Reson. Med. 78 (2017) 739–745.

[57] M. Tibiletti, J. Paul, A. Bianchi, S. Wundrak, W. Rottbauer, D. Stiller, V. Rasche, Multistage three-dimensional UTE lung imaging by image-based self-gating, Magn. Reson. Med. 75 (2016) 1324–1332.

[58] P. Hu, S. Hong, M.H. Moghari, B. Goddu, L. Goepfert, K. V. Kissinger, T.H. Hauser, W.J. Manning, R. Nezafat, Motion correction using coil arrays (MOCCA) for free-breathing cardiac cine MRI, Magn. Reson. Med. 66 (2011) 467–475.

[59] A.C. Larson, R.D. White, G. Laub, E.R. McVeigh, D. Li, O.P. Simonetti, Self-Gated Cardiac Cine MRI, Magn. Reson. Med. 51 (2004) 93–102.

[60] G. V. Lee GR, Chen Y, A correlation based approach to respiratory self navigation for multi channel non-Cartesian MRI, Proc Intl Soc Magn Reson Med. (2015) 585.

[61] D.B. Gandhi, A. Rice, C.C. Gunatilaka, N.S. Higano, R.J. Fleck, A. de Alarcon, C.K. Hart, I.C. Kuo, R.S. Amin, J.C. Woods, E.B. Hysinger, A.J. Bates, Quantitative evaluation of subglottic stenosis using ultrashort echo time MRI in a rabbit model, Laryngoscope. (2021) lary.29363.

[62] A.J. Bates, N.S. Higano, J.C. Woods, Non-Bronchoscopic Assessment of the Airways, in: Humana, Cham, 2021: pp. 155–169.

[63] J.G. Pipe, P. Menon, Sampling density compensation in MRI: Rationale and an iterative numerical solution, Magn. Reson. Med. 41 (1999) 179–186.

[64] J.I. Jackson, C.H. Meyer, D.G. Nishimura, A. Macovski, Selection of a convolution function for Fourier inversion using gridding (computerised tomography application), IEEE Trans. Med. Imaging. 10 (1991) 473–478.

[65] A.J. Bates, Fundamentals of Fluid Dynamics, in: 2021: pp. 117–156.

[66] C.M. Rhie, W.L. Chow, Numerical study of the turbulent flow past an airfoil with trailing edge separation, AIAA J. 21 (1983) 1525–1532.

[67] Siemens Product Lifecycle Management Software Inc, User Guide, (2019).

[68] A.J. Bates, Mechanics of Airflow in Human Inhalation, Imperial College London, 2014.

[69] Q. Xiao, Computational modelling of airflow and transport in the upper respiratory tract, Imperial College London, 2019.

[70] O. Ben-Nasr, A. Hadjadj, A. Chaudhuri, M.S. Shadloo, Assessment of subgrid-scale modeling for large-eddy simulation of a spatially-evolving compressible turbulent boundary layer, Comput. Fluids. 151 (2017) 144–158.

[71] F. Nicoud, F. Ducros, Subgrid-scale stress modelling based on the square of the velocity gradient tensor, Flow, Turbul. Combust. 62 (1999) 183–200.

[72] H. Calmet, A.M. Gambaruto, A.J. Bates, M. Vázquez, G. Houzeaux, D.J. Doorly, Large-scale CFD simulations of the transitional and turbulent regime for the large human airways during rapid inhalation, Comput. Biol. Med. 69 (2016) 166–180.

[73] A.J. Bates, D.J. Doorly, R. Cetto, H. Calmet, A.M. Gambaruto, N.S. Tolley, G. Houzeaux, R.C. Schroter, Dynamics of airflow in a short inhalation, J. R. Soc. Interface. 12 (2015) 20140880.

[74] A.J. Bates, A. Comerford, R. Cetto, D.J. Doorly, R.C. Schroter, N.S. Tolley, Computational fluid dynamics benchmark dataset of airflow in tracheas, Data Br. 10 (2017) 101–107.

[75] K. Bass, S. Boc, M. Hindle, K. Dodson, W. Longest, High-Efficiency Nose-to-Lung Aerosol Delivery in an Infant: Development of a Validated Computational Fluid Dynamics Method, J. Aerosol Med. Pulm. Drug Deliv. 32 (2019) 132–148.

[76] Star CCM+ User Guide | Mathematical Model | Fluid Dynamics, (2006).

[77] P.A. Yushkevich, J. Piven, H.C. Hazlett, R.G. Smith, S. Ho, J.C. Gee, G. Gerig, User-guided 3D active contour segmentation of anatomical structures: Significantly improved efficiency and reliability, Neuroimage. 31 (2006) 1116–1128.

[78] Q. Xiao, R. Cetto, D.J. Doorly, A.J. Bates, J.N. Rose, C. Mcintyre, A. Comerford, G. Madani, N.S. Tolley, R. Schroter, Assessing changes in airflow and energy loss in a progressive tracheal compression before and after surgical correction, Ann. Biomed. Eng. 48 (2020) 822–833.

[79] C.L. Lin, M.H. Tawhai, G. McLennan, E.A. Hoffman, Characteristics of the turbulent laryngeal jet and its effect on airflow in the human intra-thoracic airways, Respir. Physiol. Neurobiol. 157 (2007) 295–309.

[80] P. Cignoni, M. Callieri, M. Corsini, M. Dellepiane, F. Ganovelli, G. Ranzuglia, MeshLab: An open-source mesh processing tool, 6th Eurographics Ital. Chapter Conf. 2008 - Proc. (2008) 129–136.

[81] G. Taubin, Curve and surface smoothing without shrinkage, IEEE Int. Conf. Comput. Vis. (1995) 852–857.

[82] W. Shi, X. Zhuang, L. Pizarro, W. Bai, H. Wang, K.P. Tung, P. Edwards, D. Rueckert, Registration using sparse free-form deformations, in: Lect. Notes Comput. Sci. (Including Subser. Lect. Notes Artif. Intell. Lect. Notes Bioinformatics), Springer Verlag, 2012: pp. 659–666.

[83] J.A. Schnabel, D. Rueckert, M. Quist, J.M. Blackall, A.D. Castellano-Smith, T. Hartkens, G.P. Penney, W.A. Hall, H. Liu, C.L. Truwit, F.A. Gerritsen, D.L.G. Hill, D.J. Hawkes, A generic framework for non-rigid registration based on non-uniform multi-level free-form deformations, in: Lect. Notes Comput. Sci. (Including Subser. Lect. Notes Artif. Intell. Lect. Notes Bioinformatics), Springer Verlag, 2001: pp. 573–581.

[84] D. Rueckert, Nonrigid registration using free-form deformations: Application to breast mr images, IEEE Trans. Med. Imaging. 18 (1999) 712–721.

[85] E.R.E. Denton, L.I. Sonoda, D. Rueckert, S.C. Rankin, C. Hayes, M.O. Leach, D.L.G. Hill, D.J. Hawkes, Comparison and evaluation of rigid, affine, and nonrigid registration of breast MR images, J. Comput. Assist. Tomogr. 23 (1999) 800–805.

[86] A.J. Bates, A. Schuh, K. McConnell, B.M. Williams, J.M. Lanier, M.M. Willmering, J.C. Woods, R.J. Fleck, C.L. Dumoulin, R.S. Amin, A novel method to generate dynamic boundary conditions for airway CFD by mapping upper airway movement with non-rigid registration of dynamic and static MRI, Int. J. Numer. Method. Biomed. Eng. 34 (2018) e3144.

[87] A. Schuh, M. Murgasova, A. Makropoulos, C. Ledig, S.J. Counsell, J. V Hajnal, P. Aljabar, D. Rueckert, Construction of a 4D brain atlas and growth model using diffeomorphic registration, in: Lect. Notes Comput. Sci. Vol 8682. Springer, Cham., 2015: pp. 27–37.

[88] A. Schuh, A. Makropoulos, E.C. Robinson, L. Cordero-Grande, E. Hughes, J. Hutter, A.N. Price, M. Murgasova, R.P.A.G. Teixeira, N. Tusor, J.K. Steinweg, S. Victor, M.A. Rutherford, J. V. Hajnal, A. David Edwards, D. Rueckert, Unbiased construction of a temporally consistent morphological atlas of neonatal brain development, bioRxiv. (2018) 251512.

[89] Y. Chen, G. Medioni, Object modeling by registration of multiple range images, in: Proc. - IEEE Int. Conf. Robot. Autom., Publ by IEEE, 1991: pp. 2724–2729.

[90] P.J. Besl, N.D. McKay, Method for registration of 3-D shapes, in: P.S. Schenker (Ed.), Sens. Fusion IV Control Paradig. Data Struct., SPIE, 1992: pp. 586–606.

[91] Z. Zhang, Iterative point matching for registration of free-form curves and surfaces, Int. J. Comput. Vis. 13 (1994) 119–152.

[92] Engineering ToolBox, Density of Moist Humid Air, [Online] Available at: Https://www.engineeringtoolbox.com/density-Air-d_680.html. (2004).

[93] An introduction to air density and density altitude calculations, [Online] Available at: https://wahiduddin.net/calc/density_altitude.htm#b15. (2019).

[94] A. Picard, R.S. Davis, M. Gläser, K. Fujii, Revised formula for the density of moist air (CIPM-2007), IOP Publ. Metrol. Metrol. 45 (2008) 149–155.

[95] J.W.W. De Backer, W.G.G. Vos, A. Devolder, S.L.L. Verhulst, P. Germonpré, F.L.L. Wuyts, P.M.M. Parizel, W. De Backer, Computational fluid dynamics can detect changes in airway resistance in asthmatics after acute bronchodilation, J. Biomech. 41 (2008) 106–113.

[96] S.C. Persak, S. Sin, J.M. McDonough, R. Arens, D.M. Wootton, Noninvasive estimation of pharyngeal airway resistance and compliance in children based on volume-gated dynamic MRI and computational fluid dynamics, J. Appl. Physiol. 111 (2011) 1819–1827.

[97] C. Xu, S.H. Sin, J.M. McDonough, J.K. Udupa, A. Guez, R. Arens, D.M. Wootton, Computational fluid dynamics modeling of the upper airway of children with obstructive sleep apnea syndrome in steady flow, J. Biomech. 39 (2006) 2043–2054.

[98] M. Brouns, S.T. Jayaraju, C. Lacor, J. De Mey, M. Noppen, W. Vincken, S. Verbanck, Tracheal stenosis: a flow dynamics study, J. Appl. Physiol. 102 (2007) 1178–1184.

[99] A.J.J. Bates, A. Comerford, R. Cetto, R.C.C. Schroter, N.S.S. Tolley, D.J.J. Doorly, Power loss mechanisms in pathological tracheas, J. Biomech. 49 (2016) 2187–2192.

[100] M.M. Yang, N.S. Higano, C.C. Gunatilaka, E.B. Hysinger, R.S. Amin, J.C. Woods, A.J. Bates, Subglottic stenosis position affects work of breathing, Laryngoscope. (2020) lary.29169.

[101] T. Cheng, D. Carpenter, S. Cohen, D. Witsell, D.O. Frank-Ito, Investigating the effects of laryngotracheal stenosis on upper airway aerodynamics, Laryngoscope. 128 (2018) E141–E149.

[102] A.J. Bates, R. Cetto, D.J. Doorly, R.C. Schroter, N.S. Tolley, A. Comerford, The effects of curvature and constriction on airflow and energy loss in pathological tracheas, Respir. Physiol. Neurobiol. 234 (2016) 69–78.

[103] D.O. Frank-Ito, K. Schulz, G. Vess, D.L. Witsell, Changes in aerodynamics during vocal cord dysfunction, Comput. Biol. Med. 57 (2015) 116–122.

[104] R. Arens, S. Sin, J.M. McDonough, J.M. Palmer, T. Dominguez, H. Meyer, D.M. Wootton, A.I. Pack, Changes in upper airway size during tidal breathing in children with obstructive sleep apnea syndrome, Am. J. Respir. Crit. Care Med. 171 (2005) 1298–1304.

[105] J. Huynh, K.B. Kim, M. McQuilling, Pharyngeal airflow analysis in obstructive sleep apnea patients pre-and post-maxillomandibular advancement surgery, J. Fluids Eng. Trans. ASME. 131 (2009) 0911011–09110110.

[106] G.J. Collier, M. Kim, Y. Chung, J.M. Wild, 3D phase contrast MRI in models of human airways: Validation of computational fluid dynamics simulations of steady inspiratory flow, J. Magn. Reson. Imaging. 48 (2018) 1400–1409.

[107] T. Iwasaki, H. Sato, H. Suga, Y. Takemoto, E. Inada, I. Saitoh, K. Kakuno, R. Kanomi, Y. Yamasaki, Influence of pharyngeal airway respiration pressure on Class II mandibular retrusion in children: A computational fluid dynamics study of inspiration and expiration, Orthod. Craniofacial Res. 20 (2017) 95–101.

[108] M. Mihaescu, S. Murugappan, E. Gutmark, L.F. Donnelly, M. Kalra, Computational modeling of upper airway before and after adenotonsillectomy for obstructive sleep apnea, Laryngoscope. 118 (2008) 360–362.

[109] S. Miyawaki, S. Choi, E.A. Hoffman, C.-L. Lin, A 4DCT imaging-based breathing lung model with relative hysteresis, J. Comput. Phys. 326 (2016) 76–90.

[110] A.J. Bates, A. Schuh, G. Amine-Eddine, K. McConnell, W. Loew, R.J. Fleck, J.C. Woods, C.L. Dumoulin, R.S. Amin, Assessing the relationship between movement and airflow in the upper airway using computational fluid dynamics with motion determined from magnetic resonance imaging, Clin. Biomech. 66 (2019) 88–96.

[111] C. Roussos, P.T. Macklem, The Thorax, in: Dekker, New York, 1985.

[112] J. Mancebo, D. Isabey, H. Lorino, F. Lofaso, F. Lemaire, L. Brochard, Comparative effects of pressure support ventilation and intermittent positive pressure breathing (IPPB) in non-intubated healthy subjects, Eur. Respir. J. 8 (1995) 1901–1909.

[113] O. Hjalmarson, T. Olsson, Work of Breathing, Acta Pædiatrica. 63 (1974) 49–60.

[114] S. Davis, M. Jones, J. Kisling, C. Angelicchio, R.S. Tepper, Effect of continuous positive airway pressure on forced expiratory flows in infants with tracheomalacia, Am. J. Respir. Crit. Care Med. 158 (1998) 148–152.

[115] H.B. Panitch, J.L. Allen, B.E. Alpert, D. V Schidlow, Effects of CPAP on lung mechanics in infants with acquired tracheobronchomalacia, Am J Respir Crit Care Med. 150 (1994) 1341–1346.

[116] J. Levy, R.H. Habib, E. Liptsen, R. Singh, D. Kahn, A.M. Steele, S.E. Courtney, Prone versus supine positioning in the well preterm infant: Effects on work of breathing and breathing patterns, Pediatr. Pulmonol. 41 (2006) 754–758.

[117] V.K. Bhutani, E.M. Sivieri, S.A. Md, T.H. Shaffer Phd, Evaluation of neonatal pulmonary mechanics and energetics: A two factor least mean square analysis, Pediatr. Pulmonol. 4 (1988) 150–158.

[118] S.E. Courtney, Z.H. Aghai, J.G. Saslow, K.H. Pyon, R.H. Habib, Changes in lung volume and work of breathing: A comparison of two variable-flow nasal continuous positive airway pressure devices in very low birth weight infants, Pediatr. Pulmonol. 36 (2003) 248–252.

[119] P.B. Pandit, S.E. Courtney, K.H. Pyon, J.G. Saslow, R.H. Habib, Work of breathing during

constant- and variable-flow nasal continuous positive airway pressure in preterm neonates, Pediatrics. 108 (2001) 682–685.

[120] J. Zhao, Y. Feng, C.A. Fromen, Glottis motion effects on the particle transport and deposition in a subject-specific mouth-to-trachea model: A CFPD study, Comput. Biol. Med. 116 (2020) 103532.

[121] J. Xi, X. April Si, H. Dong, H. Zhong, Effects of glottis motion on airflow and energy expenditure in a human upper airway model, Eur. J. Mech. - B/Fluids. 72 (2018) 23–37.

[122] M. Baz, G.S. Haji, A. Menzies-Gow, R.J. Tanner, N.S. Hopkinson, M.I. Polkey, J.H. Hull, Dynamic laryngeal narrowing during exercise: A mechanism for generating intrinsic peep in COPD?, Thorax. 70 (2015) 251–257.

[123] S. Mishra, Early diagnosis of airway closure from pigtail signature capnogram and its management in intubated small infants undergoing general anaesthesia for surgery, Indian J. Anaesth. 54 (2010) 331–334.

[124] V.C. Harrison, H. de V. Heese, M. Klein, The significance of grunting in hyaline membrane disease, Pediatrics. 41 (1968).

[125] M. Piccinelli, A. Veneziani, D.A. Steinman, A. Remuzzi, L. Antiga, A framework for geometric analysis of vascular structures: Application to cerebral aneurysms, IEEE Trans. Med. Imaging. 28 (2009) 1141–1155.

[126] R.L. Thoman, G.L. Stoker, J.C. Ross, The efficacy of pursed-lips breathing in patients with chronic obstructive pulmonary disease., Am. Rev. Respir. Dis. 93 (1966) 100–106.

[127] P.E. Pepe, J.J. Marini, Occult positive end-expiratory pressure in mechanically ventilated

patients with airflow obstruction: The auto-PEEP effect, Am. Rev. Respir. Dis. 126 (1982) 166–170.

[128] T. Higenbottam, J. Payne, Glottis narrowing in lung disease, Am. Rev. Respir. Dis. 125 (1982) 746–750.

[129] J.P. Praud, V. Diaz, I. Kianicka, D. Dalle, Active expiratory glottic closure during permeability pulmonary edema in nonsedated lambs, Am. J. Respir. Crit. Care Med. 152 (1995) 732–737.

[130] V. Diaz, I. Kianicka, P. Letourneau, J.-P. Praud, Inferior pharyngeal constrictor electromyographic activity during permeability pulmonary edema in lambs, J. Appl. Physiol. 81 (1996) 1598–1604.

[131] R.H. Ingram, D.P. Schilder, Effect of pursed lips expiration on the pulmonary pressure-flow relationship in obstructive lung disease., Am. Rev. Respir. Dis. 96 (1967) 381–388.

[132] H.B. Panitch, J.L. Allen, B.E. Alpert, D. V. Schidlow, R. Motley, T. Bradley, Effects of CPAP on lung mechanics in infants with acquired tracheobronchomalacia, Am. J. Respir. Crit. Care Med. 150 (1994) 1341–1346.

[133] B.S. Ko, D.T.L. Wong, B.L. Nørgaard, D.P. Leong, J.D. Cameron, S. Gaur, M. Marwan, S. Achenbach, S. Kuribayashi, T. Kimura, I.T. Meredith, S.K. Seneviratne, Diagnostic performance of transluminal attenuation gradient and noninvasive fractional flow reserve derived from 320-detector row CT angiography to diagnose hemodynamically significant coronary stenosis: An NXT substudy, Radiology. 279 (2016) 75–83.

[134] C.A. Taylor, T.A. Fonte, J.K. Min, Computational fluid dynamics applied to cardiac

computed tomography for noninvasive quantification of fractional flow reserve: Scientific basis, J. Am. Coll. Cardiol. 61 (2013) 2233–2241.

Copyright Clearance Permissions

Copyright permits have been obtained for all figures used in this thesis that have been published in journal articles [53][54].

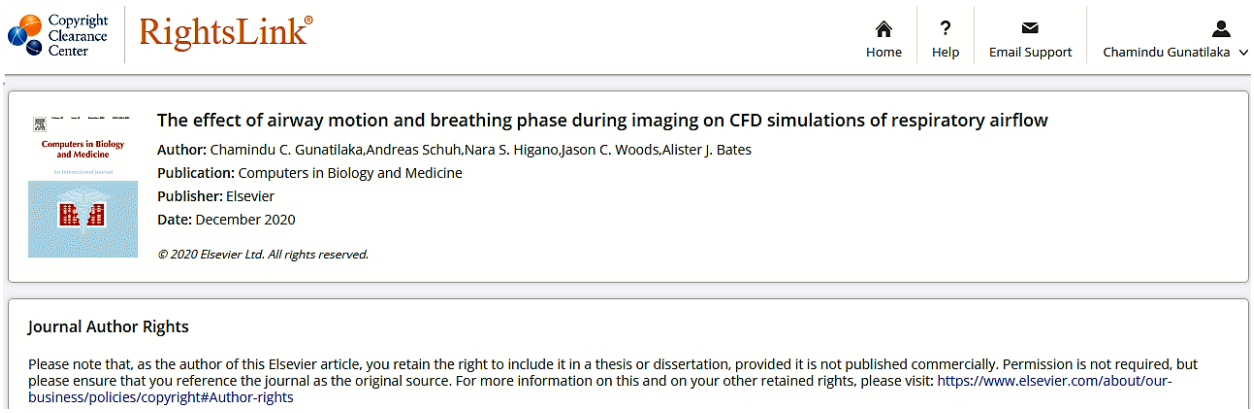

From: Gunatilaka, Chamindu <Chamindu.Gunatilaka@cchmc.org>
Sent: Thursday, February 25, 2021 7:36 PM
To: ATS Permission Requests <permissions@thoracic.org>
Subject: Reuse article in the thesis/dissertation

Hello,

I published a research article in the Annals of ATS journal last year. I would like to use the article in my thesis/dissertation, which I will submit to the University of Cincinnati, OH, as a part of my degree requirement. The following are the details of my request.

Article title: Increased work of breathing due to tracheomalacia in neonates

Authors: Chamindu C. Gunatilaka, Nara S. Higano, Erik B. Hysinger, Deep B. Gandhi, Robert J. Fleck, Andrew D. Hahn, Sean B. Fain, Jason C. Woods, Alister J. Bates

Page Range: 1247-1256

Volume Number: 17

Journal Title: Annals of ATS

Requested figures/ tables: Figure 1, Figure 3, Figure 4, Figure 5, Figure 6, Figure 7, Table 1, Table 2

Thank you.
Chamindu

From: ATS Permission Requests [mailto:permissions@thoracic.org]
Sent: Friday, February 26, 2021 10:15 AM
To: Gunatilaka, Chamindu <Chamindu.Gunatilaka@cchmc.org>
Subject: RE: Reuse article in the thesis/dissertation

Dear Dr. Gunatilaka,

Thank you for your request. Because you are one of the original authors, an active ATS member, and this request is for thesis use, permission for one time use of these unmodified figures is granted at no charge. Please complete the below and use it beneath the material. Thank you.

Reprinted with permission of the American Thoracic Society.

Cite: Author(s)/Year/Title/Journal title/Volume/Pages.
Annals of the American Thoracic Society is an official journal of the American Thoracic Society.

Thank you, and please let me know if you have any questions or concerns.

Best regards,

Megan

Megan Murphy
Production Coordinator
American Thoracic Society
25 Broadway, 4th Floor
New York, NY 10004
212-315-8643
mmurphy@thoracic.org